

TYCO



NASA

CR 70930

TYCO LABORATORIES, INC., BEAR HILL, WALTHAM, MASSACHUSETTS 02154 TELEPHONE 617 899-1650

Development of Cathodic
Electrocatalysts for Use
in Low Temperature H_2/O_2
Fuel Cells with an
Alkaline Electrolyte

Contract No. NASW-1233

Q-2

Second Quarterly Report
Covering Period October 1
Through December 31, 1965

for
National Aeronautics and Space
Administration
Headquarters, Washington, D.C.

GPO PRICE \$ _____
CFSTI PRICE(S) \$ \$ 4.00
Hard copy (HC) 1.00
Microfiche (MF) _____
853 July 65

FACILITY FORM 802

N66 24550

(ACCESSION NUMBER)

(THRU)

(PAGES)

(CODE)

(NASA CR OR TMX OR AD NUMBER)

(CATEGORY)

CONTRACT OBJECTIVES

The research under contract NASW-1233 is directed towards the development of an improved oxygen electrode for use in alkaline H_2/O_2 fuel cells. The work is being carried out for the National Aeronautics and Space Administration with Mr. E. Cohn as technical monitor. Principal Investigators are A. C. Makrides, J. Giner, and R. J. Jasinski.

Tyco Laboratories, Inc.
Bear Hill
Waltham, Massachusetts

DEVELOPMENT OF CATHODIC ELECTRO-
CATALYSTS FOR USE IN LOW TEMPERATURE
 H_2/O_2 FUEL CELLS WITH AN
ALKALINE ELECTROLYTE

Contract No. NASW-1233

Q-2

Second Quarterly Report
Covering Period October 1
Through December 31, 1965

for

National Aeronautics and Space
Administration
Headquarters, Washington, D.C.

CONTENTS

	<u>Page No.</u>
List of Figures	iii
I. Abstract	1
II. Introduction	2
III. Experimental	3
A. Preparation of Samples of Intermetallic Compounds	3
B. Intermetallic Substitutional Compounds of Refractory Elements	3
C. Preparation of Interstitials of Metal of the VIII-Group Metals	4
D. Electrode Assembly	6
E. Electrochemical Test of Compact Samples	8
IV. Results	10
A. $i(E)$ -curves of Pure Elements	10
B. Intermetallic Compounds	12
C. Solid Solutions	19
D. Interstitials/Substitutionals	20
E. Ternary Systems	22
F. Metallurgical Characterization of Intermetallic Compounds	89
V. General Discussion	108
VI. Future Work	109
Distribution List	

LIST OF FIGURES

<u>Figure No.</u>		<u>Page No.</u>
1 a & b	Electrode Assemblies	7
2	i (E)-curve for Graphite	23
3	i (E)-curve for Titanium	24
4	i (E)-curve for Chromium	25
5	i (E)-curve for Iron	26
6	i (E)-curve for Cobalt	27
7a	i (E)-curve for Nickel	28
7b	i (E)-curve for Nickel	29
8	i (E)-curve for Zirconium	30
9	i (E)-curve for Molybdenum	31
10	i (E)-curve for Palladium	32
11	i (E)-curve for Hafnium	33
12	i (E)-curve for Nb ₃ Pt	34
13	i (E)-curve for Mo ₃ Pt	35
14	i (E)-curve for Ni ₃ Al	36
15a	i (E)-curve for Zr ₂ Ni	37
15b	i (E)-curve for Zr ₂ Ni (Rerun)	38
16	i (E)-curve for Ti ₂ Cu	39
17	i (E)-curve for TiCo	40
18	i (E)-curve for NiAl	41
19	i (E)-curve for CoAl	42
20	i (E)-curve for MoPt	43
21	i (E)-curve for TaV ₂ (II)	44
22	i (E) i (E)-curve for HfW ₂	45
23	i (E)-curve for TiCr ₂	46
24	i (E)-curve for ZrW ₂	47
25	i (E)-curve for ZrMo ₂	48
26	i (E)-curve for HfMo ₂	49
27	i (E)-curve for TaCr ₂	50
28	i (E)-curve for TaFe ₂	51
29	i (E)-curve for NbPt ₂	52
30a	i (E)-curve for TaPt ₂	53

LIST OF FIGURES (Cont.)

<u>Figure No.</u>		<u>Page No.</u>
30b	i (E)-curve for TaPt ₂ (Rerun)	54
31a	i (E)-curve for TiPt ₃	55
31b	i (E)-curve for TiPt ₃ (Rerun)	56
32	i (E)-curve for CoPt ₃	57
33	i (E)-curve for ZrPt ₃	58
34	i (E)-curve for TaPd ₃	59
35a	i (E)-curve for TaPt ₃	60
35b	i (E)-curve for TaPt ₃ (Rerun)	61
36a	i (E)-curve for TiNi ₃	62
36b	i (E)-curve for TiNi ₃ (Rerun)	63
37	i (E)-curve for V Pt ₃	64
38a	i (E)-curve for ZrAu ₃	65
38b	i (E)-curve for ZrAu ₃ (Rerun)	66
39	i (E)-curve for MoNi ₄	67
40	i (E)-curve for TaNi (μ)	68
41	i (E)-curve for TaV ₂ (I)	69
42a	i (E)-curve for 66.6% Co - 33.3% Ni	70
42b	i (E)-curve for 66.6% Co - 33.3% Ni (Rerun)	71
43	i (E)-curve for 30% Pd - 70% Ag	72
44	i (E)-curve for 50% Pd - 50% Ag	73
45	i (E)-curve for 70% Pd - 30% Ag	74
46	i (E)-curve for 80% Pd - 20% Ag	75
47	i (E)-curve for 90% Pd - 10% Ag	76
48	i (E)-curve for Cr ₂ B	77
49	i (E)-curve for Ni ₂ B	78
50	i (E)-curve for B ₄ C	79
51	i (E)-curve for VC	80
52	i (E)-curve for Fe ₂ C	81
53	i (E)-curve for ZrC	82
54	i (E)-curve for NbC	83
55	i (E)-curve for Mo ₂ C	84
56	i (E)-curve for HfC	85
57	i (E)-curve for TaC	86

LIST OF FIGURES (Cont.)

<u>Figure No.</u>		<u>Page No.</u>
58	i (E)-curve for Ni_2P	87
59	i (E)-curve for Co_2NiAl_3	88
60	AB_2 Stoichiometry: TaPt_2	90
61	AB_3 Stoichiometry: TiPt_3	91
62	AB_3 Stoichiometry: TaPt_3	92
63	AB_3 Stoichiometry: NbNi_3	93
64	AB_3 Stoichiometry: TiNi_3	94
65	Interstitials: Ni_3B	95
66	A_3B Stoichiometry: Mo_3Pt	96
67	A_2B Stoichiometry: Ti_2Cu	97
68	AB Stoichiometry: TiCo	98
69	AB Stoichiometry: NiAl	99
70	AB Stoichiometry: CoAl	100
71	AB Stoichiometry: MoPt	101
72	AB_3 Stoichiometry: CoPt_3	102
73	AB_n , $n > 3$ Stoichiometry: MoNi_4	103
74	Solid Solutions: TaV	104
75	Solid Solution: Co_2Ni	105
76	Interstitials: Ni_2B	106
77	Ternary Compounds; AB Stoichiometry: $(\text{Co}_{.67}\text{Ni}_{.33})\text{Al}$	107

I. ABSTRACT

Fifty-eight materials including ten elements have been tested in this quarter for corrosion resistance and activity as oxygen electrodes in 2 N KOH at 75°C. The technique used was to measure the current-potential curve with rotated compact electrodes completely immersed in KOH solutions saturated either with nitrogen or oxygen.

The materials tested were selected according to two criteria introduced in the first quarterly report. In one approach (continuum approach), the major factor considered was the structure of the material such as an intermetallic compound, while in the other approach (atomistic approach), combinations of elements with established properties for corrosion and activity were selected.

Of the tested elements, Pd shows very good O₂ activity, only slightly inferior to Pt (around 75 mv more polarization in the non-steady state *i* (E)-curve). Graphite shows relatively good intrinsic activity (with O₂ current at *E* = 800 mv); and iron with O₂-reduction at *E* = 600 mv is surprisingly more active than nickel.

The experiments with the intermetallic compounds show that under conditions of O₂-reduction, the fundamental factor determining the activity is the atomic factor. Thus, compounds of Pt and Au show an *i* (E)-curve for O₂-reduction which is similar (but with "diluted" activity) to those of pure Pt and Au. In some cases such as TaPt₂, the activity of the intermetallic compound is very close to the activity of pure Pt.

The solid solution "Co₂Ni" shows a very interesting behavior which confirms the catalytic activity of Co³⁺ containing oxide and the poor activity of the bivalent oxide.

Of the interstitials tested, carbides show some activity, especially an iron carbide (Hagg carbide Fe₂C) prepared by surface carburization (with CO) of an iron rod at several temperatures not exceeding 300°C; activity for O₂-reduction which, although lower than that of Pt, Pd, Ag and Au, is considerably better than the activity of Fe.

Metallographic characterization of eighteen samples of the prepared intermetallic compounds shows that in those cases where a simple phase was expected, a predominant phase with very little or no second phase was obtained.

II. INTRODUCTION

In order to improve the over-all efficiency of hydrogen-oxygen fuel cells, improvements in the performance of the oxygen electrode are needed, since the high polarization of this electrode is the main source of inefficiency.

The approach followed in this work in order to obtain better O_2 -electrodes is to investigate the catalytic properties for O_2 -reduction and the corrosion resistance to the alkali electrolyte of a large number of compounds selected according to structural or atomic considerations. The criteria for catalyst selection according to structural factors have been discussed in detail in the first quarterly report. Selections are made from intermetallic compounds of the T - T - type (i. e. of two transition metals) with the objective of testing the possibility that the continuum properties (electronic properties) of the crystal may have decisive influence on its catalytic activity even if the elements (or one of them) are not catalytically active. Similarly, compounds of the T - B - type (i. e. one transition metal and an element on the right side of the periodic table) with special emphasis on interstitial/substitutional compounds such as borides, carbides, nitrides, oxides, and silicides are being tested.

Since, under the conditions of electrolyte and potential, the surface of the catalyst will usually be a mixed oxide, oxides are of especial interest, and attention will be given to them in a later phase of this work.

To select a catalyst according to atomistic considerations, elements with favorable catalytic activity and/or corrosion resistance, as established empirically in published research or during the course of the present work, will be combined in order to give a composite material of better over-all performance.

III. EXPERIMENTAL

In order to test a large number of materials in the least ambiguous manner possible, we have chosen to test in the first phase of the program, compact samples immersed and rotated in 2 N KOH solution saturated with oxygen.

The test procedure was described in the first quarterly report; in the following only the essentials of the method and the variations introduced since the last report will be described.

A. Preparation of Samples of Intermetallic Compounds

The intermetallic compounds of the T - T type and the solid solutions tested were prepared by melting in an arc furnace under an argon atmosphere mixtures of carefully weighed correct proportions of the elementary components. In order to eliminate oxygen in the furnace, Ti powder, which acts as an oxygen getter, was melted prior to the melting of the sample.

The resulting samples are buttons of approximately 1 cm diameter. Compounds which are known (from the phase diagram) to form congruently were tested without any subsequent heat treatment, while materials which are formed through a peritectic reaction were annealed in a vacuum furnace at a temperature selected from the phase diagram in such a way that no melting occurs, while, at the same time, fast homogenization at the practical time periods used is achieved. The cases where annealing was used are reported in the text with the temperature and time used.

A large portion of the compounds compared were analyzed metallographically and the results are given under "Characterization" (section IV F).

B. Intermetallic/Substitutional Compounds of Refractory Elements

The following compounds have been ordered and received from Cerac, Inc. as hot-pressed truncated cones of 95% density. This geometry has been selected as a convenience in the electrode mounting, as described below.

1. Borides

CrB	NbB	TaB ₂	W ₂ B
CrB ₂	NbB ₂		VB ₂
Cr ₅ B ₃	SiB ₆	TiB ₂	
MoB	SiB ₄	WB	ZrB ₂
MoB ₂	TaB	W ₂ B ₅	

2. Carbides

B ₄ C	Mo ₂ C	TiC	(94 WC - 6 Co)
Cr ₃ C ₂	NbC	VC	(80 WC - 20 Co)
HfC	TaC	ZrC	

3. Nitrides

Cr ₂ N	NbN	TiN	ZrN
HfN	TaN	VN	

4. Silicides

CrSi ₂	MoSi ₂		VS ₂
Cr ₃ Si	NbSi ₂	TiSi ₂	
CoSi ₂	TaSi ₂	Ti ₅ Si ₃	ZrSi ₂
MnSi ₂	Ta ₅ Si ₃	WSi ₂	(Si-B ₆ Si)

C. Preparation of Interstitials of Metal of the VIII-Group Metals

Work has been started on preparing carbides, nitrides, and carbonitrides of Fe, Co and Ni. These interstitials are compounds with interesting catalytical properties, especially with respect to the Fischer-Tropsch processes ^(1, 2). In general, in preparing these compounds, care-

1. J. F. Schultz, L. J. H. Hofer, E. M. Cohn, K. C. Stein, and R. B. Anderson, Bureau of Mines Bulletin No. 578.
2. J. F. Schultz, L. J. H. Hofer, K. C. Stein, and R. B. Anderson, Bureau of Mines Bulletin No. 612.

ful control of the temperature and gas composition has to be exerted in order to remain in the range of thermodynamic stability. In order to prepare the compounds, three furnace tubes equipped to work under CO and NH₃ atmospheres have been constructed. The operation of these furnaces will be described in subsequent reports when data of the prepared materials are discussed. The preparation of a sample of Fe₂C (Hagg carbide) is briefly described below. Four iron carbides have been described in the literature ⁽¹⁻³⁾, i.e. "FeC", the "hexagonal iron carbide" of controversial formulation (Fe₂C or Fe₃C) (both discovered in used Fischer-Tropsch catalysts), Hagg carbide (Fe₂C), and cementite (Fe₃C). The three last carbides can be obtained separately under action of CO on finely divided iron by regulating the temperature. In that way, at temperatures under 170°C hexagonal close packed carbide is obtained; between T = 170°C and 300°C, Hagg carbides are obtained; and at temperatures higher than 300°C, cementite is obtained. If hydrogen is used previous to the carburization (CO treatment) - or still better, simultaneously with the carburization - contaminations by oxygen are eliminated.

In the first attempts to prepare Fe₂C, carbon monoxide was passed over a pure iron sponge (99.999%) at temperatures of 150° - 270°C. In the first run, pure iron was used without pretreatment. Carbon monoxide was passed over the sample for 27 hours according to the following temperature schedule recommended in the literature:

150°C, 4 hrs; 200°C, 15 hrs; 250°C, 4 hrs; and 275°C, 4 hrs.

X-ray analysis indicated mostly iron and magnetite.

In the second run, two pure iron samples, consisting of a compact 99.999% iron cylinder mounted in an electrode assembly to be described later, and pure iron sponge (99.999%) were carburized according to the following schedule:

Reduction: H₂ - 325°C, 15 hrs; carburization: CO, 170°C, 8 hrs;
200°C, 15 hrs; 250°C, 4 hrs; and 300°C, 4 hrs.

-
3. K. J. Jack, Proc. Roy. Soc. (London) A195, 34 (1948); *ibid* A195, 41 (1948), and *ibid* A195, 56 (1948).

After this treatment X-ray analysis of the powder showed strong evidence of carbide, but still with too large proportions of unreacted iron and magnetite. The preliminary results of the electrochemical test for O_2 -reduction activity will be described later. Further preparations with new furnaces and mixtures of hydrogen and carbon monoxide are underway.

D. Electrode Assembly

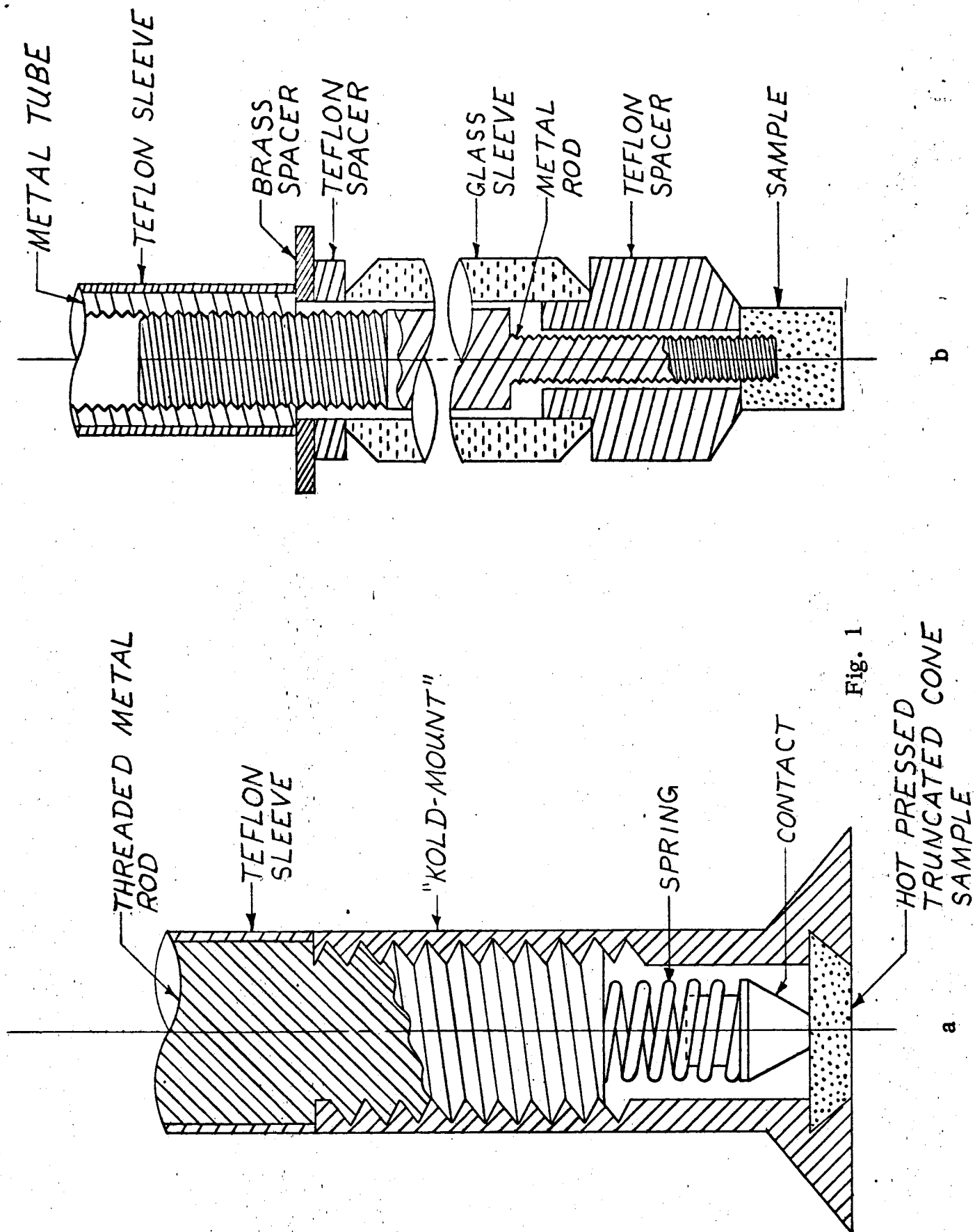
In the previous quarterly report, a description was given of how the button obtained from the argon arc furnace is cut with two parallel faces and mounted in "Koldmount" to give a "rotating disc" with a face exposed to the electrolyte, while the other face is used to make contact against a spring placed between this face and an iron rod axis externally insulated with Teflon. The whole assembly is rotated at 600 rpm.

In order to mount the interstitials and substitutionals of the refractory metals obtained from Cerac, the samples in the form of truncated cones were mounted in "Koldmount" so as to expose the short face to the electrolyte. Electrical contact with the screw was made to the base of the cone. Care was taken to avoid detaching the electrode material from the surrounding "Koldmount" when applying force to the spring (see Fig. 1a).

The ductile materials were run using a demountable electrode assembly described by Stern and Makrides⁽⁴⁾ and shown in Fig. 1b. In this assembly, the tapped and threaded steel rod is inserted through a Teflon washer and screwed to the sample. A heavy-walled glass tube ground at the lower end is made to exert pressure on the Teflon gasket when a nut at the top end of the steel rod is tightened against the glass tube. By grinding the glass tube and machining the low part of the Teflon washer to a sharp edge, a liquid-tight seal at the glass-Teflon and Teflon-sample junctions can be achieved. As usual, this electrode assembly was rotated by a Sargent synchronous motor at 600 rpm. The advantage of such an arrangement is that it eliminates the uncertainty of the effect of "Koldmount" on the measured activity curves (a minor disadvantage is that the limiting current cannot be described in a simple manner, e.g. by the Levich expression for a rotating disc). From the comparison of the measurement with elements of known relative activity for O_2 -reduction such as Pt, Ag,

4. M. Stern and A. C. Makrides, J. Electrochem. Soc. 107, 782 (1960).

4 X ACTUAL SIZE



Au, and Ni with Koldmount and from experiments (to be described later) made with Koldmount and with the Teflon washer arrangement on the same material (Ni), it can be concluded that this material is satisfactory for our semiquantitative screening; for more complete studies, the Teflon arrangement is preferred when possible. The tests described in the present report were made using the "Koldmount" assembly (Fig. 1a) if nothing else is stated.

E. Electrochemical Test of Compact Samples

The test of electrochemical activity for O_2 -reduction and the corrosion resistance to the electrolyte as a function of potential using the rotating disc arrangement, was described in the first quarterly report. The corrosion resistance was measured by obtaining the $i(E)$ -curve under N_2 , while the activity for O_2 -reduction was estimated from the $i(E)$ -curve taking in oxygen saturated electrode. The $i(E)$ -curves were obtained by sweeping the potential linearly with time at a rate of 50 mv/min. During the reporting period the testing procedure has been slightly changed in order to improve the meaning of the measurements. In all the tests the $i(E)$ -curves (with N_2 or O_2) were started at potentials higher than $E = 0.9$ v and lower than $E = 1.22$ v (depending on the potential at which corrosion or a transpassive region start) and the potential was decreased to $E = 0$, at which potential the sweep was reversed again and allowed to proceed until the starting potential was reached. After the nitrogen run, a short $i(t)_E$ -curve (15 min run) at 900 - 1000 mv was taken in order to ascertain if the corrosion current showed any decrease with time. Prior to the O_2 -experiment, the electrode was usually repolished in order to start with the same surface state as during the N_2 -curve. The capacity measurements using the fast triangular sweep, described in Appendix B of the first quarterly report, was made during the $i(E)$ -curve at three potentials as long as no sizable Faradaic current existed at those potentials.

The potential of the hydrogen-evolving electrode was measured frequently, before and after tests, against a reversible hydrogen electrode in the same solution (under N_2 or O_2). In all cases, the reference electrode was 20 - 22 mv more negative than the reversible hydrogen electrode. The potential used in the graphs is referred to the hydrogen evolving electrode (or dynamic hydrogen electrode (DHE)), i. e. has not been corrected for the 20 mv.

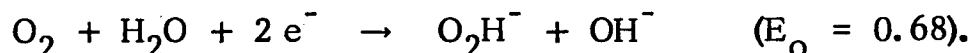
During this period, two cells have been put in use sharing the same electronic and electrical instrumentation. One cell is made ready for a run (i.e. mount the electrode, heat and saturate the solution with N_2 or with O_2) while measurements on the other cell are underway.

During the measurements, it was found that some of the $i(E)$ -curves given in the first quarterly report may have been falsified by leakage of electrolyte between sample and "Koldmount". Where doubt existed, the curves have been rerun and the results are given in the present report.

IV. RESULTS

A. i (E)-curves of Pure Elements

Graphite (Fig. 2): Graphite obtained with a compact graphite electrode mounted in "Koldmount" as shown in Fig. 1a shows sizable capacity for the O_2 -reduction starting at $E = 0.8$ volts. This confirms the intrinsic activity of carbon to reduce oxygen reversibly according to the Berl reaction:



The potential is kept more positive than the E_0 by the diffusion away from the electrode of the formed O_2H^- . The formation of O_2H^- during the O_2 -reduction is confirmed by the unusually low limiting current density and the indication of a second current step at potentials below $E = 200$ mv. The fact that graphite shows activity (even if the capacity is somehow high $C = 410 \mu f/cm^2$) under the experimental conditions selected is a reassurance for the use of this screening technique, since activity of porous non-activated carbon electrodes has long been known.

Titanium (Fig. 3): The corrosion rate of titanium is moderate and independent of potential. Activity for O_2 -reduction is negligible at potentials higher than $E = 300$ mv, but O_2 -reduction at diffusion limited current can be obtained below this potential.

Chromium (Fig. 4): The corrosion rate of chromium becomes very high above a potential of 950 millivolts; below this value, the corrosion is small. Activity for O_2 -reduction is small at potentials less than 200 millivolts, and is negligible at higher potentials.

Iron (Fig. 5): Under the conditions selected, iron shows a small corrosion peak at $E = 75$ mv with passivation at potentials higher than $E = 200$ mv. The activity for O_2 -reduction, although lower than that of Pt, Pd, Ag, Au and graphite, is remarkably high, even higher than Ni which is used as O_2 -catalyst at higher temperatures. It will be worthwhile to investigate this point further to define exactly the stability of the electrode as a function of KOH concentration, potential, and tem-

perature, and the specific catalytic activity of iron oxide such as magnetite, etc., in order to determine if, under any circumstances, Fe is a convenient catalyst, either by itself or in combination with other material. A partial answer to this question will be given when discussing the behavior of Fe_2C .

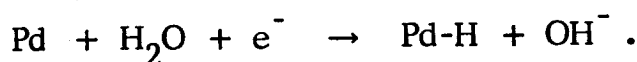
Cobalt (Fig. 6): Cobalt displayed extreme corrosion over the entire potential range, even after passivation. In the $i(E)$ -curve obtained with increasing potentials, two peaks at $E \sim 200$ mv and at $E \sim 1000$ mv are observed which probably correspond to the oxidation of Co to CoO and to the oxidation of CoO to Co_2O_3 , respectively. The interpretation of the corrosion peak observed at $E \sim 600$ mv in the $i(E)$ -curve obtained with negative potentials is difficult with the available information.

Nickel (Fig. 7a): As expected, the sample underwent no observable corrosion. Activity for O_2 -reduction is low, especially in the $i(E)$ -curve obtained with decreasing potentials, i.e. with oxidized electrode. When reversing the potential after reaching $E = 0$ mv, a strong hysteresis with increased activity is observed which can be interpreted as due to the partial reduction of the oxide at potentials lower than $E = 230$ mv (i.e. the standard potential of the reaction $\text{Ni} + 2\text{OH}^- \rightleftharpoons \text{NiO} + \text{H}_2\text{O} + 2e^-$) and to the slow formation at potentials higher than $E = 230$ mv in the $i(E)$ -curve with increasing potentials. The curve of Fig. 7b shows similar behavior when the electrode assembly was the same as that of Fig. 1b, (while for Fig. 7a the arrangement shown in Fig. 1a was used). The somewhat higher activity found in this case can be attributed at the moment to a different extent of surface oxidation or to a secondary poisoning effect by the "Koldmount". (Note also the change of the ma/cm^2 - scale due to change of geometric surface.) Since the NiO formed electrochemically under the present circumstances is an insulator, measurements with samples pre-oxidized with conductive NiO obtained by Si-doping, will be made. This will allow us to compare the activity of this electrode with the other data under exactly the same conditions.

Zirconium (Fig. 8): The corrosion is low and the activity for O_2 -reduction negligible.

Molybdenum (Fig. 9): The corrosion of this material is high at potentials higher than $E = 400$ mv, and no passivation at potentials below $E = 1000$ mv is observed.

Palladium (Fig. 10): The N_2 corrosion curve shows a cathodic current below 250 millivolts in the decreasing potential sweep. This current is due to absorption of hydrogen in palladium:



When the sweep is reversed at 0 millivolts, the current becomes less cathodic as the palladium absorption rate decreases. Finally, at about 200 millivolts, the current becomes anodic as the above equation reverses itself. There is no apparent corrosion taking place.

There is good activity for O_2 -reduction below 950 millivolts, although lower than Pt (Fig. 4, first quarterly report).

The large hysteresis observed in the activation controlled region indicates inhibition of the O_2 -reduction by "surface oxides". This hysteresis is of the same direction as that observed with Pt, but larger. Comparing the $i(E)$ -curves of Pt and Pd obtained with decreasing potentials, a difference of approximately 75 mv in favor of Pt for current start (under similar current scales) is observed.

The differences on the limiting currents obtained with Pd with increasing or decreasing potentials can be attributed to hydrogen oxidation.

Hafnium (Fig. 11): As with zirconium, no corrosion or activity for O_2 -reduction is observed.

B. Intermetallic Compounds

1. A_3B Stoichiometry

Nb_3Pt (β W type, A 15 structure, congruent) (Fig. 12):

This material corrodes strongly at any potential higher than the reversible

hydrogen potential, and although it passivates at potentials higher than $E = 600$ mv, the passive current is too high. No appreciable current decay with time was found during 15 min at $E = 900$ mv.

Mo₃Pt (β W type, A 15 structure, forms through a peritectic reaction and was heat treated at 1600°C for 40 hrs in vacuum) (Fig. 13): Metallographic analysis showed that the tested material is not a true compound, but a mixture of β -phase (i. e. phase with β W structure, and ϵ phases (MoPt). This was explained subsequently by the fact that the β W phase does not correspond to the Mo₃Pt stoichiometry. The high corrosion observed can be attributed to a combination of the corrosion of MoPt (ϵ phase) and the corrosion of the β -structure. Since the MoPt phase (see Fig. 20) corrodes much less than this mixture, it can be reasonably concluded that the pure β -phase will corrode still more than the mixture. Based on this conclusion, no attempt to prepare the β -phase has been made.

Ni₃Al (AuCu₃ type, L1₂ structure; strictly a peritectic, but virtually congruent; therefore no heat-treatment required) (Fig. 14): The qualitative behavior for corrosion resistance and O₂-activity is similar to that of pure nickel. The low capacities measured indicate that there is no leaching of aluminum from the sample.

2. A₂B Stoichiometry

Zr₂Ni (CuSi₂ type; C 16 structure, congruent) (Fig. 15): The results reported in the first quarterly report (Fig. 15a of the present report) were suspected of being falsified by an electrolyte leak between sample and "Koldmount"; repetition of the run (Fig. 15b) shows only negligible corrosion and practically no activity for O₂-reduction.

Ti₂Cu (MoSi₂ type, C 11b structure, peritectic; heat-treated in vacuum at 800°C for 160 hrs) (Fig. 16): The compound displayed a moderate but significant corrosion current in the potential range studied and some O₂-reduction current below $E = 450$ mv.

3. AB Stoichiometry

TiCo ("CsCl type", B2 structure, peritectic, heat-treated at 800°C for 160 hrs) (Fig. 17): This material shows a moderate but significant corrosion current across the entire potential range. The O_2 -reduction current is difficult to infer because of the corrosion current. It seems, however, to be significant only at potentials lower than $E = 100$ mv. Over-all, the material is not useful as an O_2 -reduction catalyst.

NiAl (CsCl type, B2 structure, congruent) (Fig. 18): This material is interesting because, in spite of the large content of aluminum, its corrosion rate is negligible from $E = 0$ to $E = 1200$ mv. Activity for O_2 -reduction is practically non-existent at potentials above 300 mv.

CoAl (CsCl type, B2 structure, congruent) (Fig. 19): The behavior of CoAl in respect to corrosion is very similar to the behavior of Co. The differences in behavior between CoAl and NiAl are similar to the differences between the pure Ni and Co.

MoPt (hexagonal close-packed structure, congruent) (Fig. 20): Considerable activity for O_2 -reduction, but excessive corrosion (although not as high as the corrosion of the mixture of the β W structure and MoPt (Fig. 13). The double layer capacity increases during the test due to roughening caused by corrosion. The difference between nitrogen and oxygen i (E)-curves at potentials higher than 800 mv cannot be explained with the available information.

4. AB₂ Stoichiometry

TaV₂ (II) (MgCu₂ type, C 15 structure (Laves phases) (Fig. 21): Tantalum and vanadium form a solid solution which, when the TaV₂ stoichiometry is selected, can be designated TaV₂ (I). This solid solution can be ordered by heat treating at 1100°C for 24 hrs to form the TaV₂ (II) of C 15 structure. Samples of both materials (TaV₂ (I) and TaV₂ (II)) have been obtained and tested; both corrode vigorously under N₂ and are not useful for O_2 -reduction catalysts. The differences between the corrosion of TaV₂ (II) and TaV₂ (I) will be discussed when discussing the TaV₂ (I), classified under "Solid Solutions".

HfW₂ (MgCu₂-type, C15 structure (Laves phase); peritectic heat-treated in vacuum at 1800°C for 26 hrs) (Fig. 22): This material starts corroding at potentials more negative than the reversible hydrogen electrode and the corrosion proceeds violently in the whole potential scale studied (from E = 0 mv to E = 1200 mv).

TiCr₂ (MgCu₂-type, C15 structure, (Laves phases); although this material is formed strictly by an ordering reaction, it can be virtually considered as congruent and therefore requires no heat-treatment) (Fig. 23): This sample shows a large corrosion current at potentials higher than 1000 mv. At potentials lower than 1000 mv, there is reasonably good stability, but the activity for O₂-reduction is negligible.

ZrW₂ (MgCu₂-type, C15 structure (Laves phase); peritectic, heat-treated at 1400°C for 30 hours in vacuum) (Fig. 24): Sample underwent high corrosion over the entire potential range studied.

ZrMo₂ (MgCu₂-type, C15 structure (Laves phase); peritectic, heat-treated at 1400°C for 30 hours in vacuum) (Fig. 25): Sample underwent high corrosion over the entire potential range studied.

HfMo₂ (MgCu₂-type, C15 structure (Laves phase); peritectic, heat-treated at 1800°C for 26 hours in vacuum) (Fig. 26): The sample showed an extremely large corrosion rate at potentials above 400 mv; while below this value, the corrosion current dropped very rapidly to zero. Since the material corrodes very sharply in the potential of region under study, it can be discarded.

TaCr₂ (This intermetallic is of the MgCu₂-type, C15 structure at low temperatures and of the MgZn₂ type, C14 structure and congruent at high temperature; since no heat-treatment followed, the sample was of the high temperature structure) (Fig. 27): Corrosion is very low below E = 0.9 volt, but catastrophic at higher potentials. Activity for O₂-reduction is negligible.

TaFe₂ (MgZn-type, C14 structure, congruent) (Fig. 28):

Corrosion is appreciable at potentials in the range of interest; activity for O₂-reduction is negligible above E = 300 mv.

NbPt₂ (Orthorhombic close-packed structure, congruent)

(Fig. 29): NbPt₂ shows little or no corrosion current over the entire 1200 mv range. The O₂-reduction activity is fairly large below 850 mv; the real surface is relatively high, C133 $\mu\text{f}/\text{cm}^2$, but not much higher than that measured for Pt, C = 115 $\mu\text{f}/\text{cm}^2$ under similar conditions (see first quarterly report, Fig. 4). In the Nb-Pt series of compounds, as the amount of platinum increases, the corrosion decreases and the O₂-reduction current increases.

TaPt₂ (TaPt₂-type, orthorhombic structure, congruent)

(Figs. 30a and b): Due to some interesting differences on corrosion between TaPt₂ and TaPt₃ reported in the first quarterly report, measurements with these compounds have been repeated. Fig. 30b shows exactly the same behavior as described before (Fig. 30a) in spite of the some higher capacity (112 $\mu\text{f}/\text{cm}^2$ as compared to 24 $\mu\text{f}/\text{cm}^2$). In general, the activity of this compound is very similar to that of pure platinum.

5. AB₃ - Stoichiometry

TiPt₃ (AuCu₃-type, L1₂ structure, congruent) (Figs. 31a

and b): Results reported in the first quarterly report (see Fig. 31a of the present report) were suspected of being caused by an electrolyte leak of the electrode assembly; new measurements with a carefully mounted electrode show (Fig. 31b) no appreciable corrosion and O₂-activity similar to but slightly lower than platinum. The lower current in the activation control region in the i (E)-curve, obtained with increasing potentials as compared with the i (E)-curve obtained with decreasing potentials, can be attributed to a time effect due to impurity poisoning.

CoPt₃ (AuCu₃-type, Ll₂ structure, formed by an ordering reaction, heat-treated at 700°C for 66 hours in vacuum) (Fig. 32): There is very little corrosion over the potential range tested. The compound exhibits good O₂-reduction activity from 900 to 0 millivolts. The hysteresis observed in the activation control region may have the same origin as suggested for TiPt₃, but it can also be caused by corrosion and/or by lack of Co³⁺ oxide in the i(E)-curve obtained with increasing potential (see later comments on Figs. 42a and b).

ZrPt₃ (TiNi₃, DO₂₄ structure, congruent) (Fig. 33): Excessive corrosion may be due to accidental leaks. These measurements will be repeated.

TaPd₃ (3 lsh stacking structure type, congruent). (Fig. 34): This sample shows moderate corrosion in the range of interest, and high activity for oxygen reduction. This activity is, in part, due to the very high roughening caused by corrosion, as indicated by the double layer capacity of $C = 663 \mu\text{f}/\text{cm}^2$.

TaPt₃ (TiCu₃-type, DO_a structure, congruent) (Figs. 35a and b): Qualitatively, the results obtained in this new run (Fig. 35b) are the same as previously reported (Fig. 35a), although the magnitude of the current in the region of diffusion control is larger in Fig. 35a than in Fig. 35b. Comparison of Fig. 30b and Fig. 35b seems to confirm that the corrosion is higher with TaPt₃ than with TaPt₂ as reported in the first quarterly report.

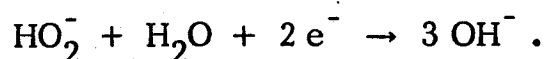
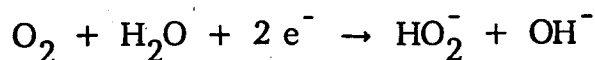
TiNi₃ (DO₂₄ - structure, congruent) (Figs. 36a and b): This compound was run again due to the suspicious nature of the peaks obtained with first sample (Fig. 36a) which did not correspond even approximately to thermodynamic potentials of any possible electrode reaction. It was felt that there may have been a crack through which the KOH solution was making contact with the connecting metal rod. A new sample was made, and the results (Fig. 36b) show that there is little corrosion in KOH solution. O₂-reduction activity is limited to potentials below 400 mv and is relatively small.

VPt₃ (3 lsh stacking structure, congruent) Fig. 37):

Corrosion is moderate, but considerable, especially in the potential region of the O₂-electrode. The activity for the O₂-reduction is relatively good in the i(E)-curve, taken with decreasing potentials. The large hysteresis in the region of activation control seems to be due to corrosion, which is due to passivation during the pre-heat-treatment at high potentials in the i(E)-curve obtained with decreasing potentials.

ZrAu₃ (2 lsh stacking structure, congruent) (Fig. 38):

After repetition of the previous run, the results (Fig. 38b) are similar to those published in the previous quarterly report (Fig. 38a), but with better defined limiting current. Similarly, as found with pure gold, indications of two steps are found in the region of diffusion control of Fig. 38b, which can be attributed to the reduction of O₂ in two distinct steps:



The undefined limiting current in Fig. 38a can be due to the same cause. Corrosion is low; the activity, although high, is lower than that of pure gold.

6. AB₄ Stoichiometry

MoNi₄ (Face centered tetragonal superstructure, peritectoid; heat-treated at 700°C for 66 hours in vacuum) (Fig. 39): Corrosion is moderate, but sizable, especially in the potential range of the O₂-electrode; activity is only high at potentials below E = 300 mv.

7. Variable Stoichiometry

Ta-Ni (μ-structure) (Fig. 40): This material has a corrosion rate and O₂-reduction activity very similar to NiAl (Fig. 18). All indications of activity for O₂-reduction appear below 300 millivolts.

TaV₂ (I) (bcc solid solution) Fig. 41): The corrosion behavior for this sample is qualitatively the same as that of the ordered species (Fig. 21). Quantitatively, it seems if the corrosion is higher for the solid solution at low potentials and for the ordered structure at higher potentials.

C. Solid Solutions

Co₂Ni (fcc solid solution) (Figs. 42a and b): This solid solution has been selected because it can form a spinel oxide layer, NiCo₂O₄, at the potential of the O₂-electrode ($0.8 \text{ v} < E < 1.2 \text{ v}$). Figure 42a shows that the corrosion rate of Co₂Ni is small in the potential range of interest. In addition, upon decreasing the potential from 1.2 volt to 0 volts in O₂-saturated solutions, appreciable activity for O₂-reduction, starting at $E^2 = 0.9 \text{ volt}$, is observed. This activity decreases at potentials lower than 0.7 volts, probably due to reduction of the Co³⁺ in the spinel. After reversing the potential sweep at 0 mv, the current increases to diffusion limited values at potentials lower than $E = 400 \text{ mv}$ due to substantial oxide reduction at the low potentials; however, no activity maximum is found in the region of 600 mv to 800 mv, probably because Co³⁺ is not formed except at higher potentials. A repeat of this experiment (Fig. 42b) shows an even more pronounced qualitative difference between the zone of activity due to Co³⁺ ($E = 900 \text{ mv}$ to $E = 600 \text{ mv}$) and the zone due to a lower oxide ($E < 400 \text{ mv}$). These experiments show the decisive effect of the composition of the surface oxide on activity. (In parallel to experiments with oxide powders, we plan to investigate the effect of pre-oxidation of compact samples of solid solutions of nickel and cobalt.

Pd-Ag Solid Solutions (fcc): Palladium-silver alloys have been the object of investigation by several groups because of their excellent properties as H₂-permeable membranes. Since both constituents show good oxygen activity, it was decided to study these alloys now as O₂-reduction catalysts. For this purpose, spheres of five different alloys mounted in an electrode configuration like that of Fig. 1b have been used. No clear difference in behavior can be concluded from the curves of Figs. 43 to 47 (described with more detail in the following). Further study with a more refined selection of experimental conditions (such as avoiding H₂-absorption, better control of oxide formation, etc.) is planned.

30% Pd-70% Ag (Fig. 43): This material shows no corrosion and a fairly good O_2 -reduction activity below 850 millivolts. Since the sample is 70 percent silver, the cathodic current due to hydrogen absorption in the palladium is extremely small.

50% Pd-50% Ag (Fig. 44): There is no appreciable corrosion; however, below 150 millivolts, there is a cathodic current due to hydrogen absorption as previously discussed for pure Pd. The O_2 -reduction activity is very good starting at 900 millivolts applied potential.

70% Pd-30% Ag (Fig. 45): There is a large cathodic current below 200 millivolts, as expected for a sample which is largely palladium, and very little, if any, corrosion. The O_2 -reduction activity is moderate below 850 millivolts, but the current seems to be smaller than expected; therefore, this material will be rerun at a later date to verify the results.

80% Pd-20% Ag (Fig. 46): On decreasing the potential in N_2 -saturated solutions, there is no apparent corrosion; below 300 millivolts, there is the usual cathodic current; finally, on increasing the potential, there is a pronounced anodic current due to the desorption of the hydrogen and not to corrosion. The O_2 -reduction activity is fairly large, though less than that of 50% Pd-50% Ag.

90% Pd-10% Ag (Fig. 47): This material shows an expected large cathodic current below 120 millivolts with a large O_2 -reduction activity below 800 millivolts. The corrosion is negligible.

D. Interstitials/Substitutionals

Cr_2B (CuAl-type, C16 structure, congruent) (Fig. 48): Corrosion high above $E = 0.8$ volt; no sizable activity for O_2 -reduction.

Ni_2B (CuAl-type, C16 structure, congruent) (Fig. 49): Corrosion resistance is good on "anodized" surfaces (i.e. starting run at high potential, 1 to 1.2 volts); it is appreciable in the $i(E)$ -curve taken with increasing potentials, probably due to reduction of a protective oxide; and in general it is worse than for pure nickel. Activity for O_2 -reduction is similar to that of pure nickel.

B₄C (Rhombohedral type structure, based probably on a group of three carbon atoms surrounded by clusters of twelve boron atoms) (Fig. 50): Corrosion resistance is good; activity for O₂-reduction is low.

VC (Complex cubic structure) (Fig. 51): This compound shows corrosion at potentials higher than E = 850 mv; below this potential there is activity for O₂-reduction.

Fe₂C (Haag carbide, obtained by carburization of iron surface; electrode mounted using assembly of Fig. 1b) (Fig. 52): This sample shows surprisingly high activity for O₂-reduction (although lower than that of Pt, Pd, Ag, and Au). Comparison with the results obtained with pure iron (Fig. 5) shows a displacement of the oxygen i(E)-curve to more positive values by approximately 100 mv; at the same time the corrosion is smaller in "Fe₂C" than in pure iron. Since the double layer capacity of the "Fe₂C" sample is 28 μf/cm² for iron, the increased activity cannot be explained in terms of roughening. A more detailed study is necessary to ascertain the intrinsic activity of the carbide and of the possible oxides.

ZrC (NaCl type, B1 structure) (Fig. 53): This material shows no appreciable corrosion. Below 400 mv there is activity for oxygen reduction without much hysteresis.

NbC (NaCl type, B1 structure) (Fig. 54): This material corrodes at potential higher than 600 mv. No activity for O₂-reduction was determined.

Mo₂C (W₂C type, hexagonal close-packed structure) (Fig. 55): There is high corrosion at potentials higher than 200 mv.

HfC (NaCl type, B1 structure) (Fig. 56): This material shows an interesting corrosion passivation behavior at potentials between 500 and 750 mv. There is clear activity for O₂-reduction at potentials below 500 mv.

TaC (NaCl type, B1 structure) (Fig. 57): The corrosion rate is very high at potentials higher than E = 700 mv, without passivation.

Ni₂P (Fe₂P type, C22 structure) (Fig. 58): Reasonably good corrosion resistance although worse than pure nickel. There is no activity for O₂-reduction above 400 mv.

E. Ternary Systems

Co_{0.66}Ni_{0.33}Al (CsCl-type, B2 structure, congruent) (Fig. 59):

This material was selected in order to investigate if it is possible to combine the performance of the Co₂Ni solid solution and the stability for corrosion of the NiAl intermetallic. Unfortunately, the corrosion is large in the whole potential range.

Current
current Dens.

+1.0 ma
+2.6 ma/cm²

0.0

-1.0 ma
-2.6 ma/cm²

GRAPHITE

2N KOH, 75°C

Scan 50 mv/min

CE:Pt RE:DHE

____ Oxygen

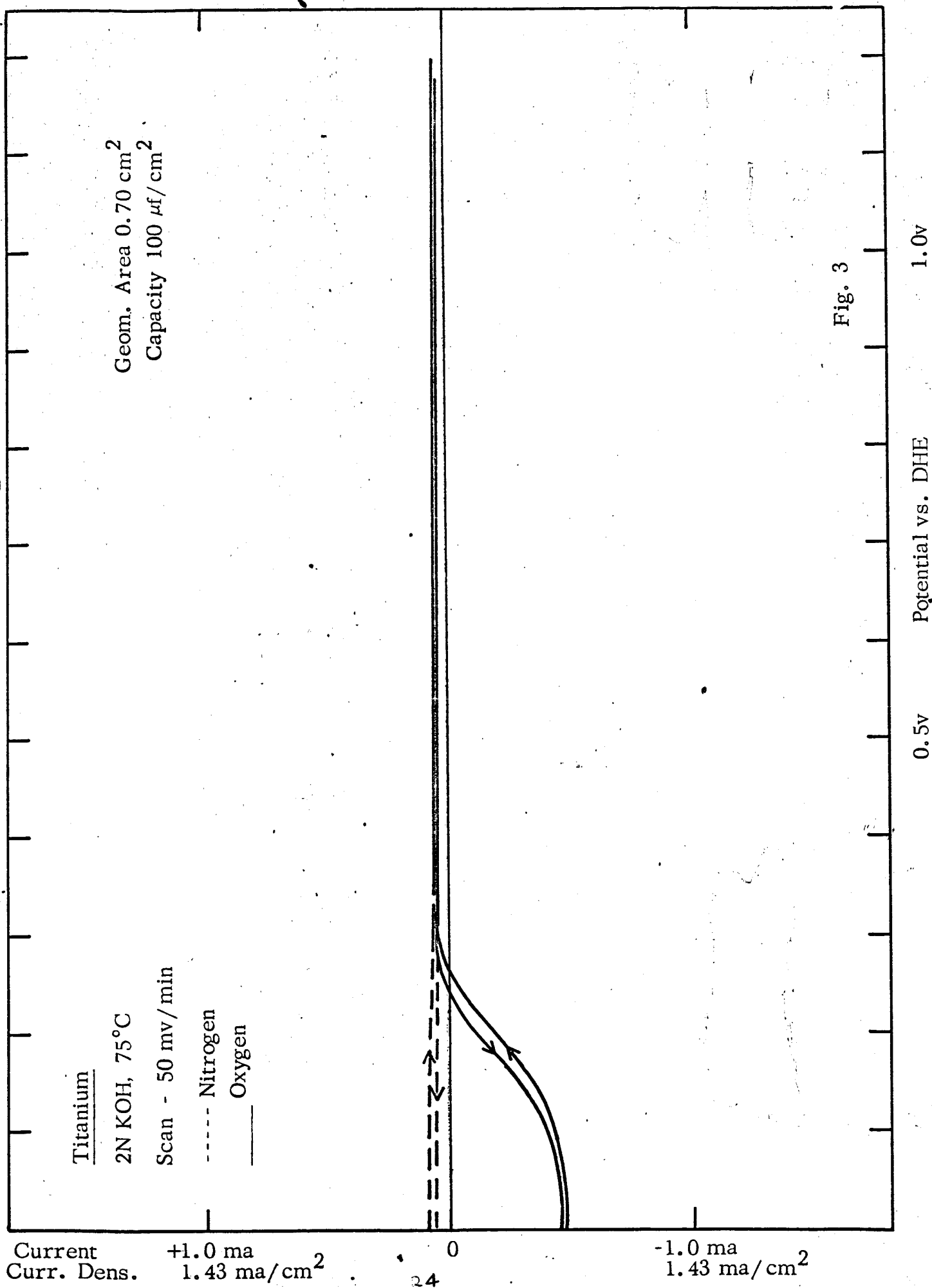
Geometric Area: .37 cm²
Average Capacity 410 μf/cm²

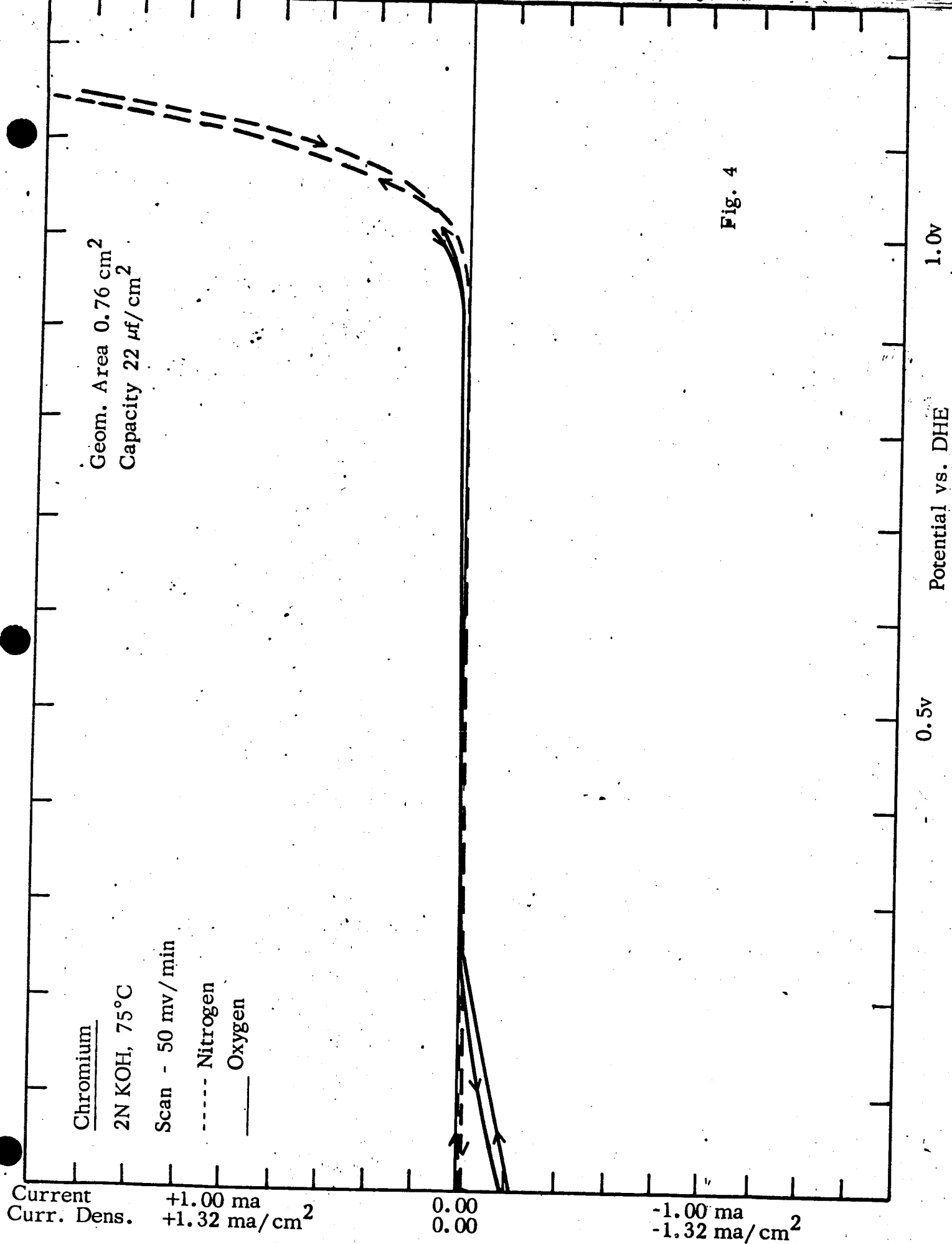
Fig. 2

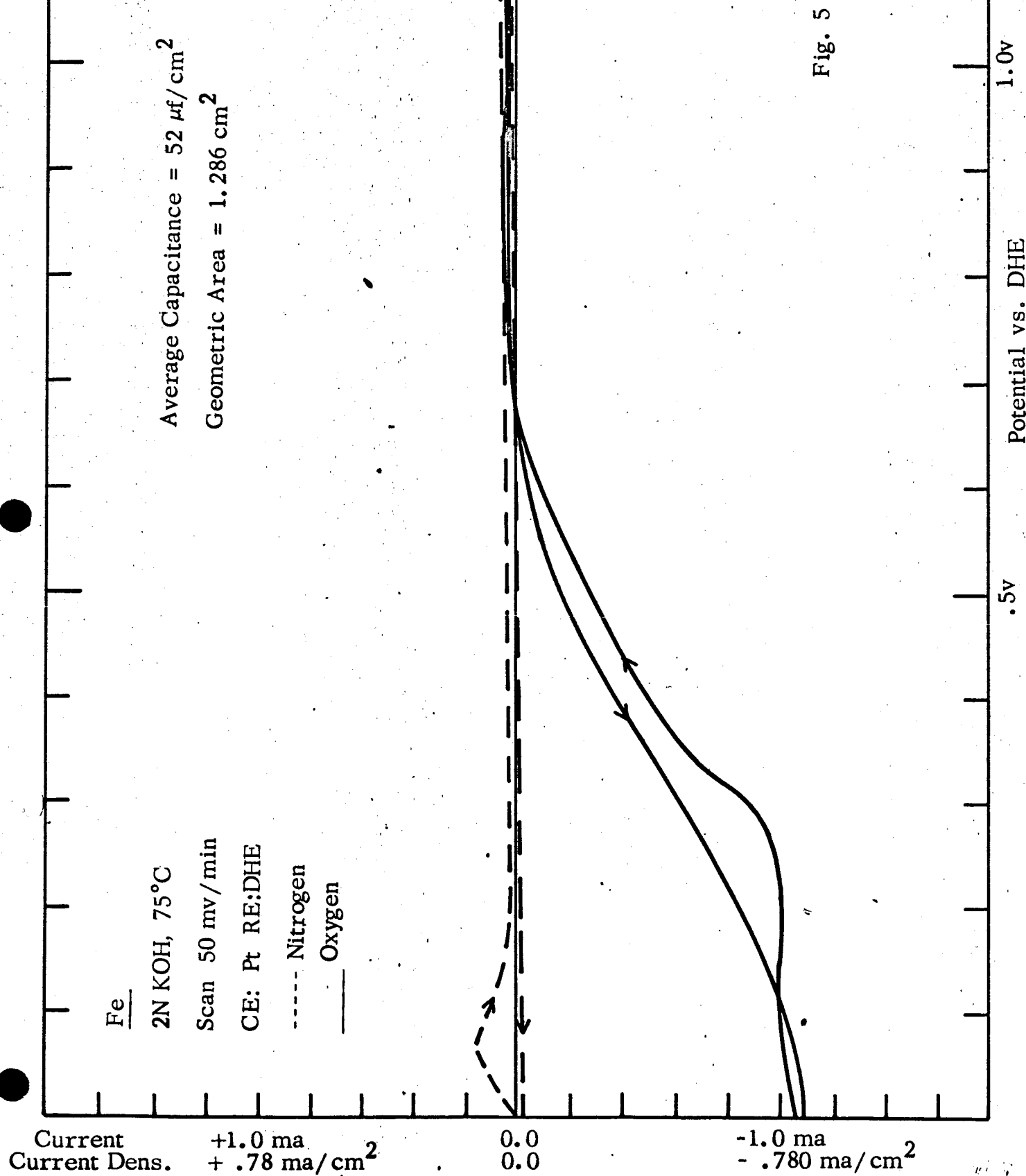
1.0v

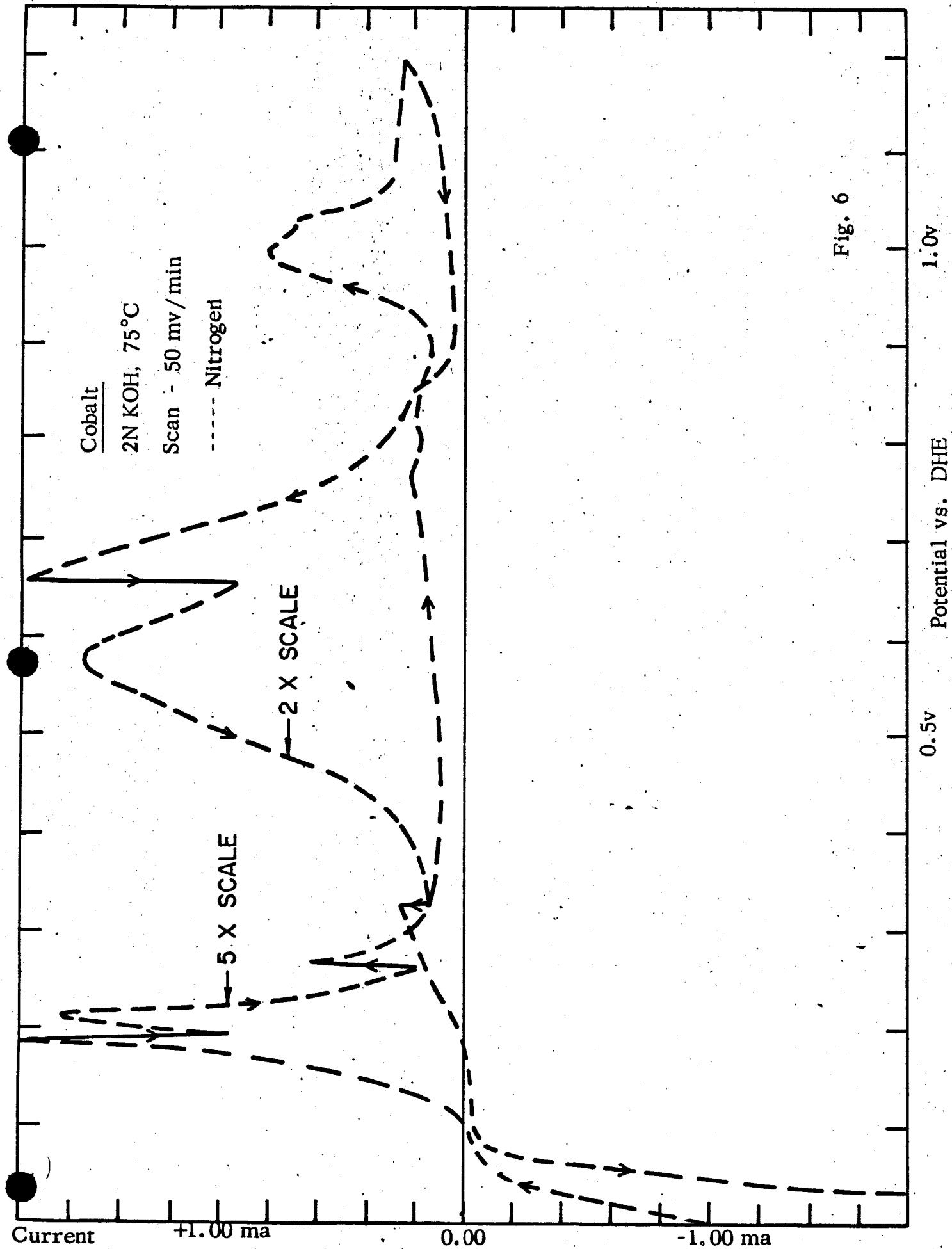
Potential vs. DHE

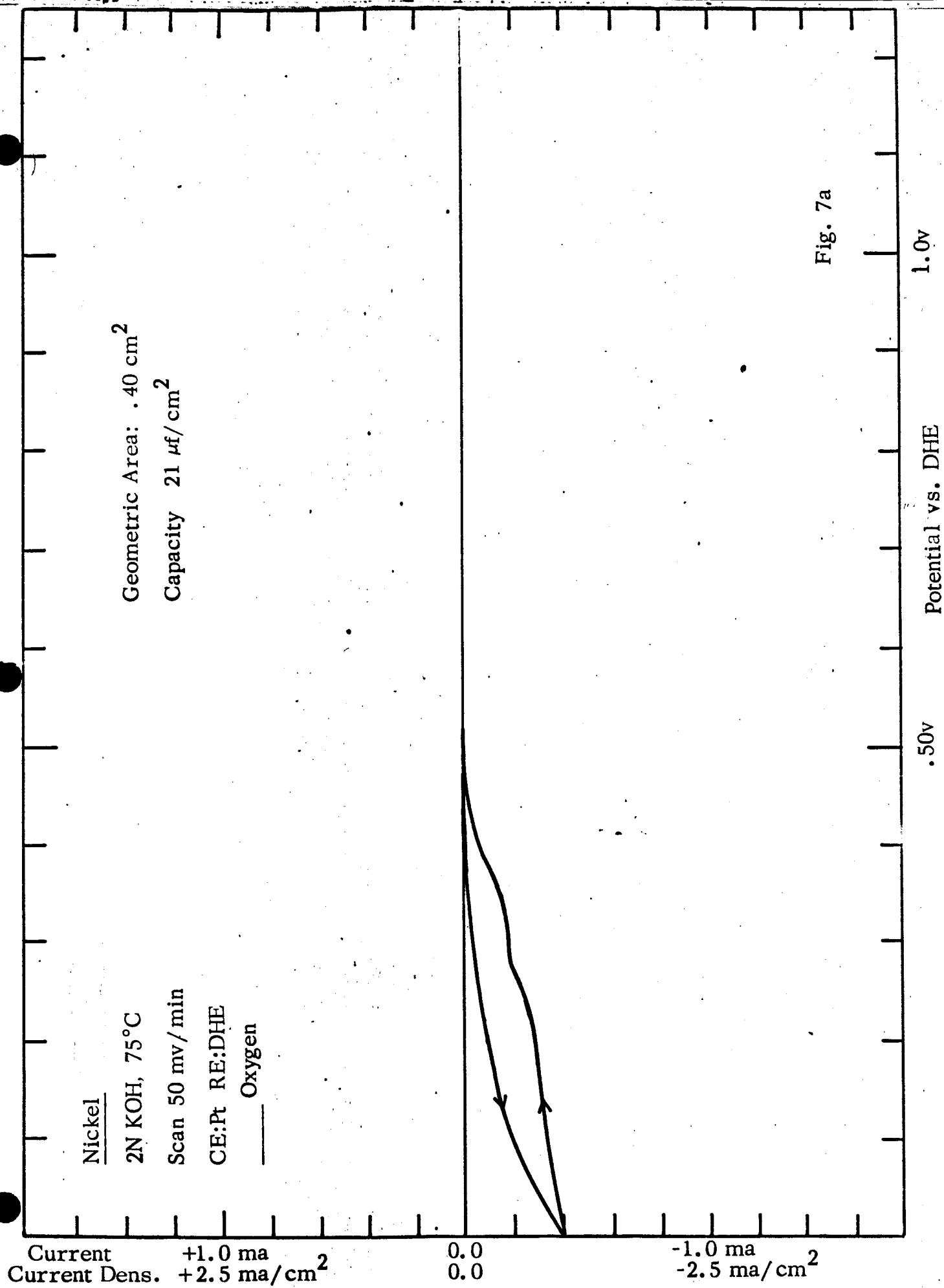
.5v

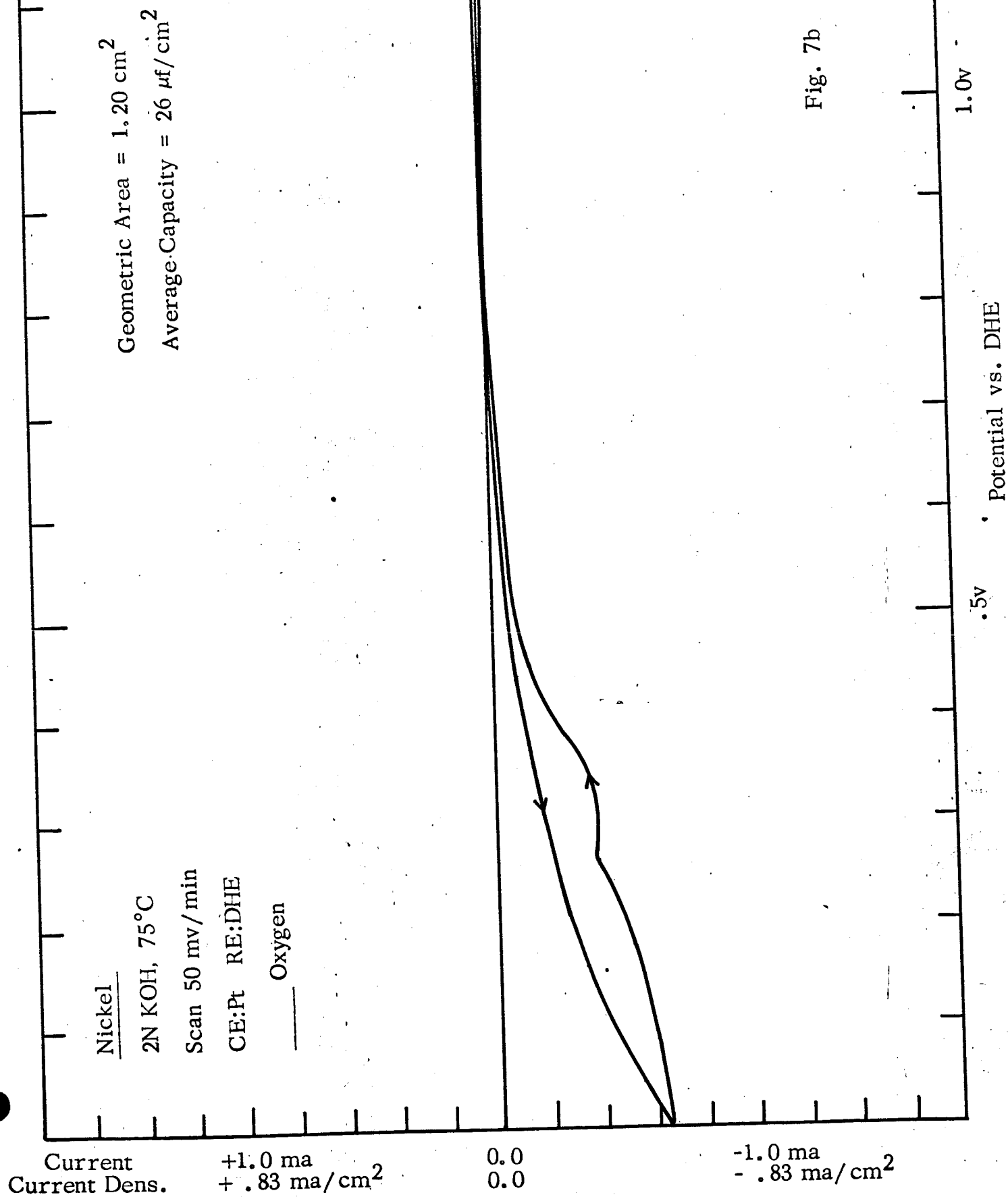


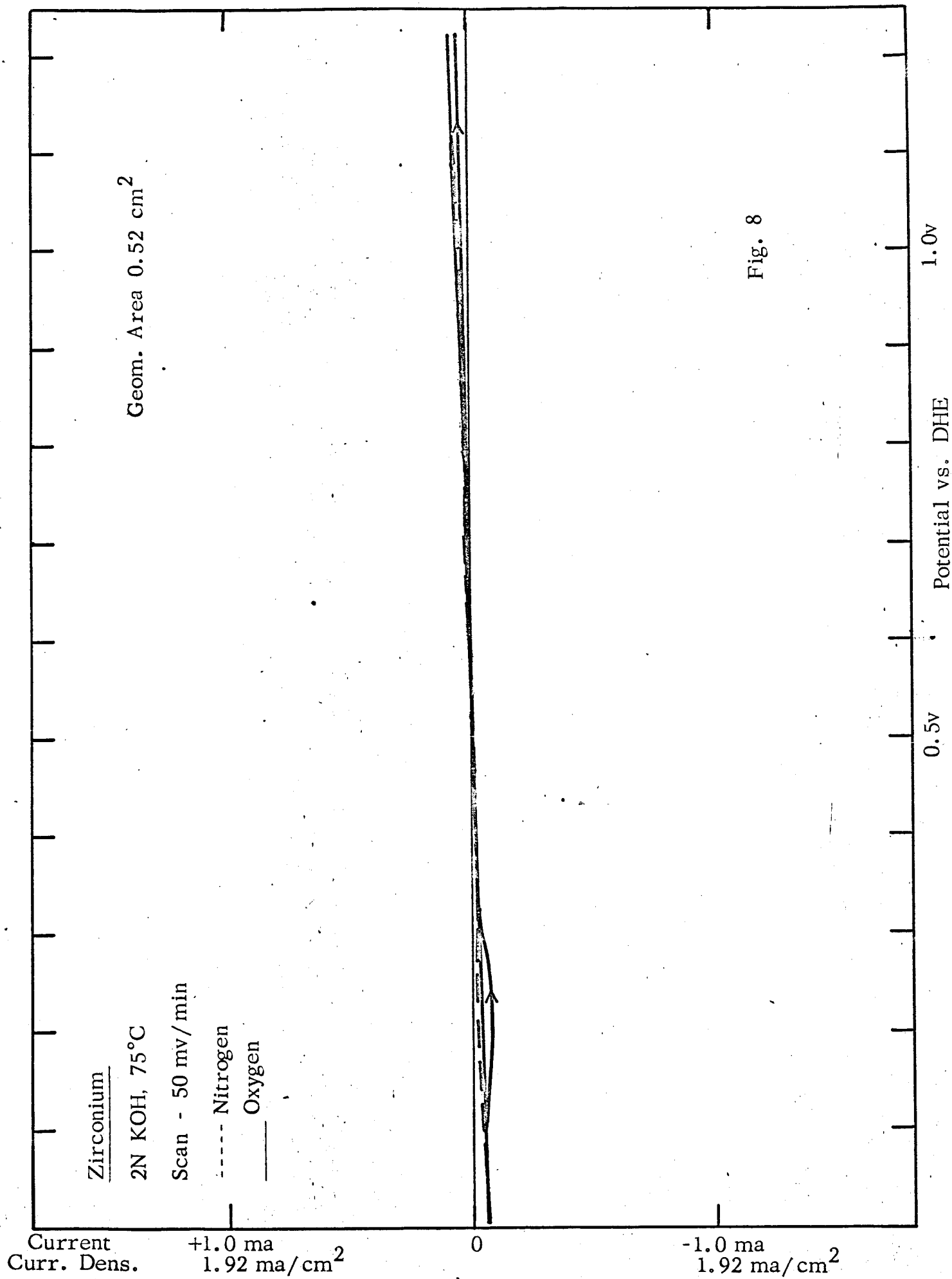












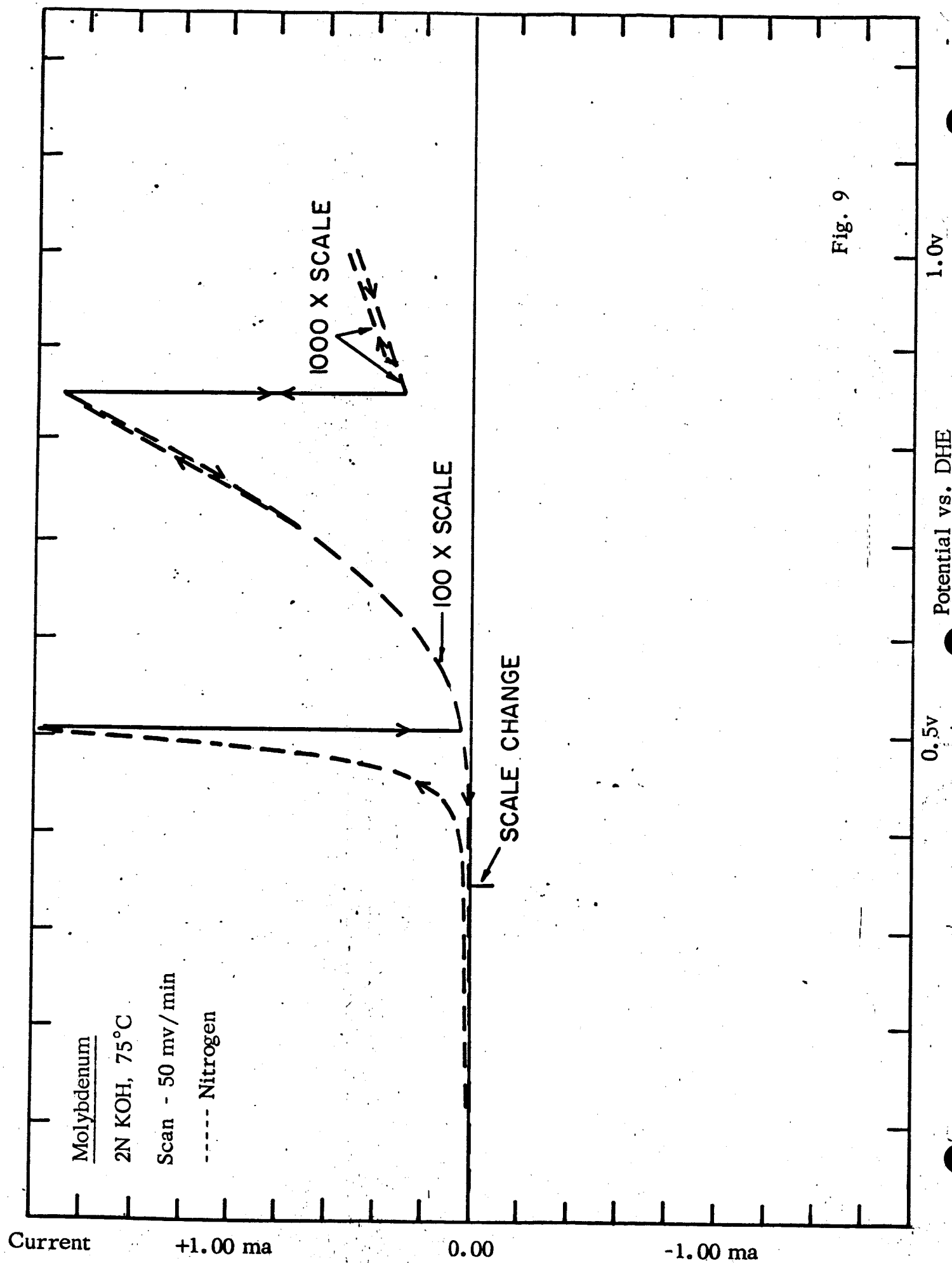
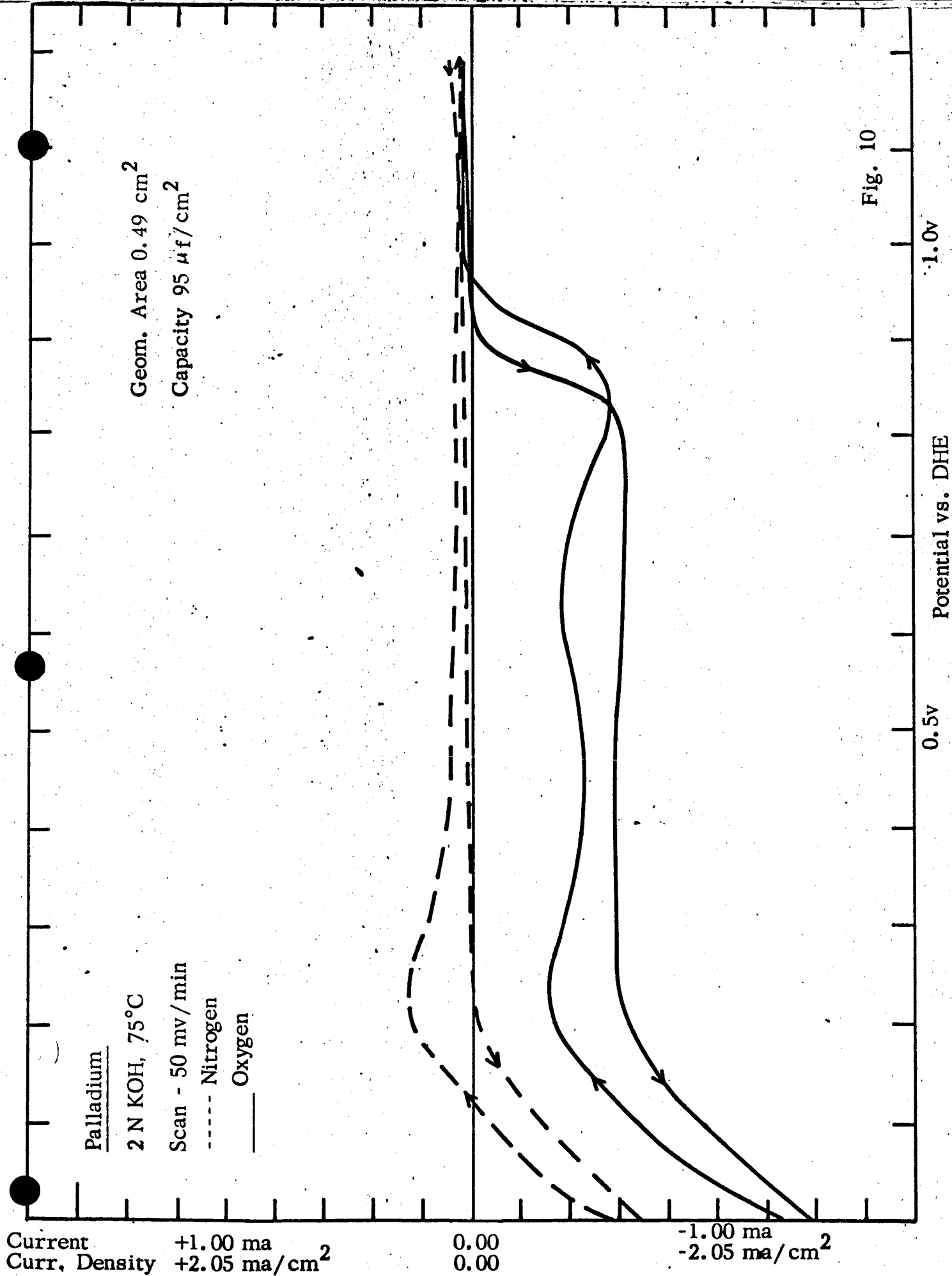
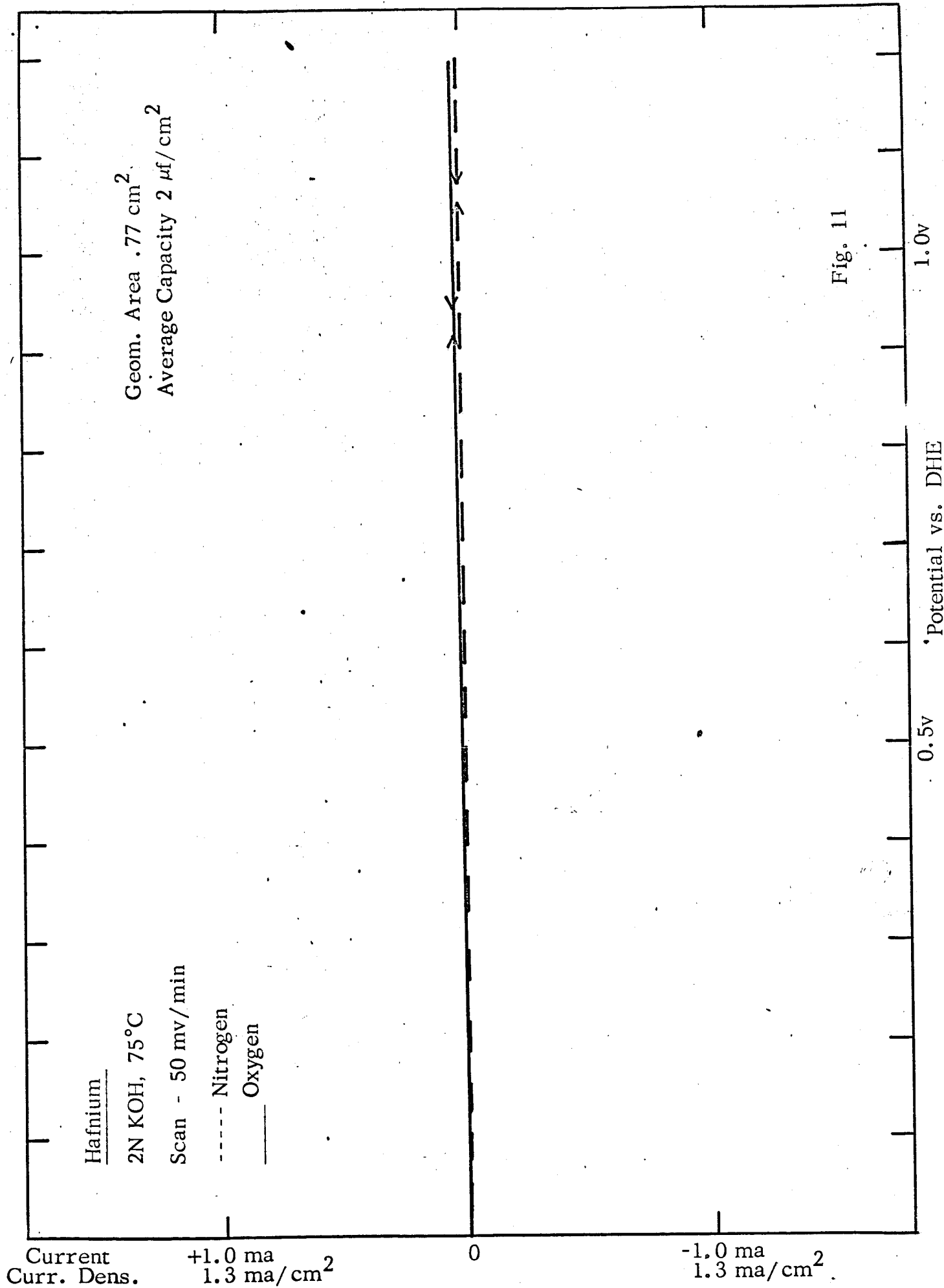


Fig. 9





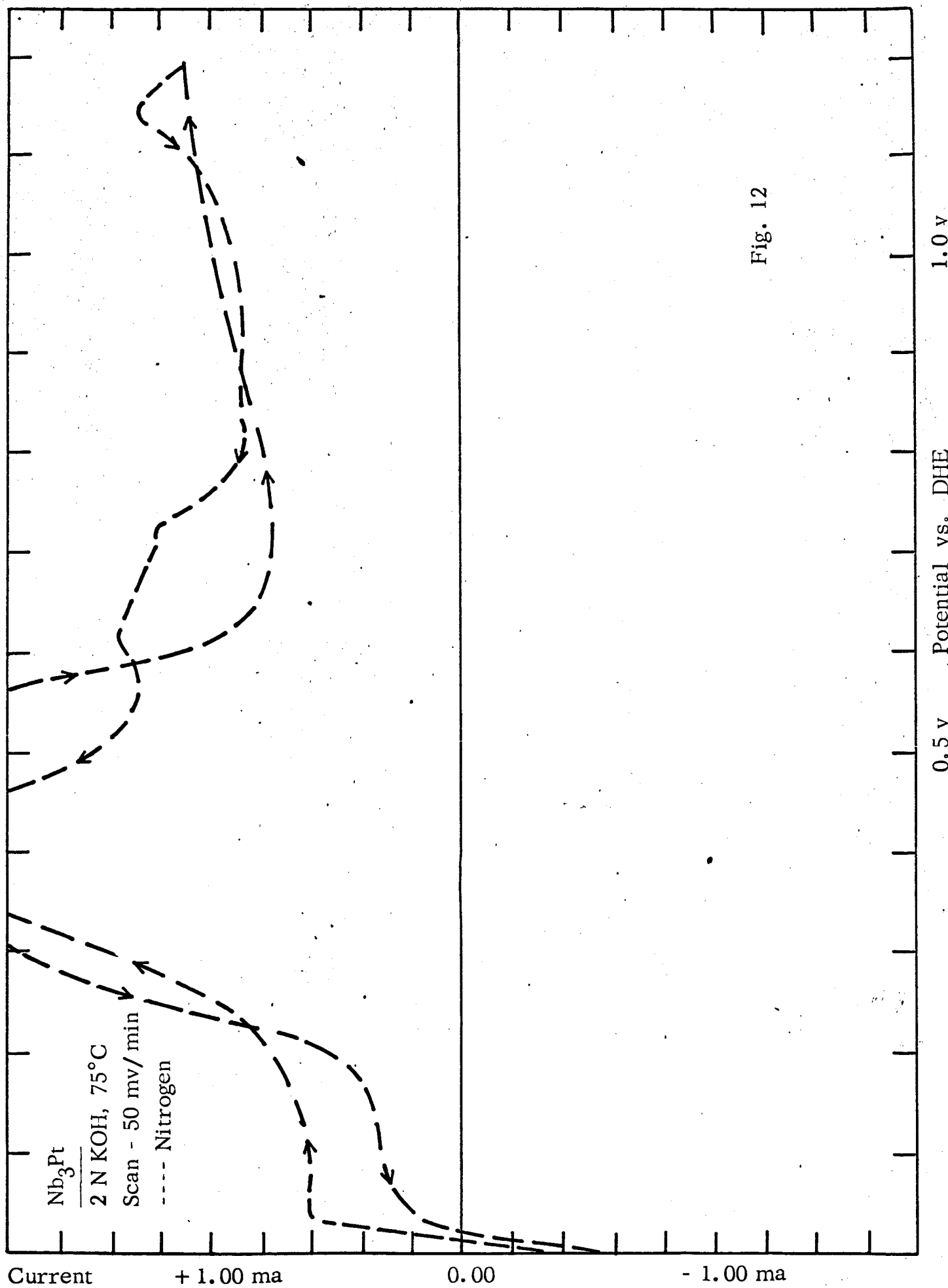


Fig. 12

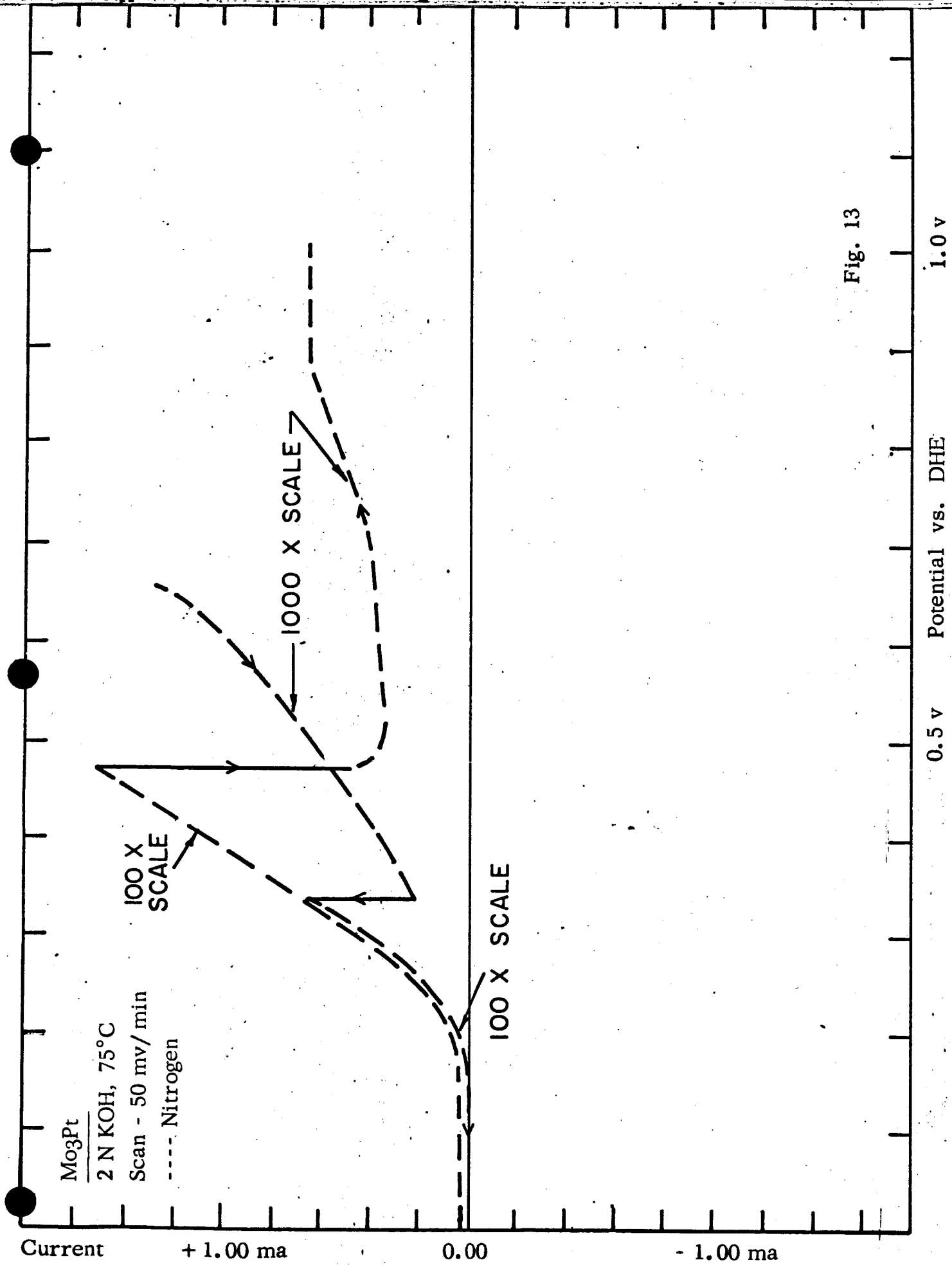
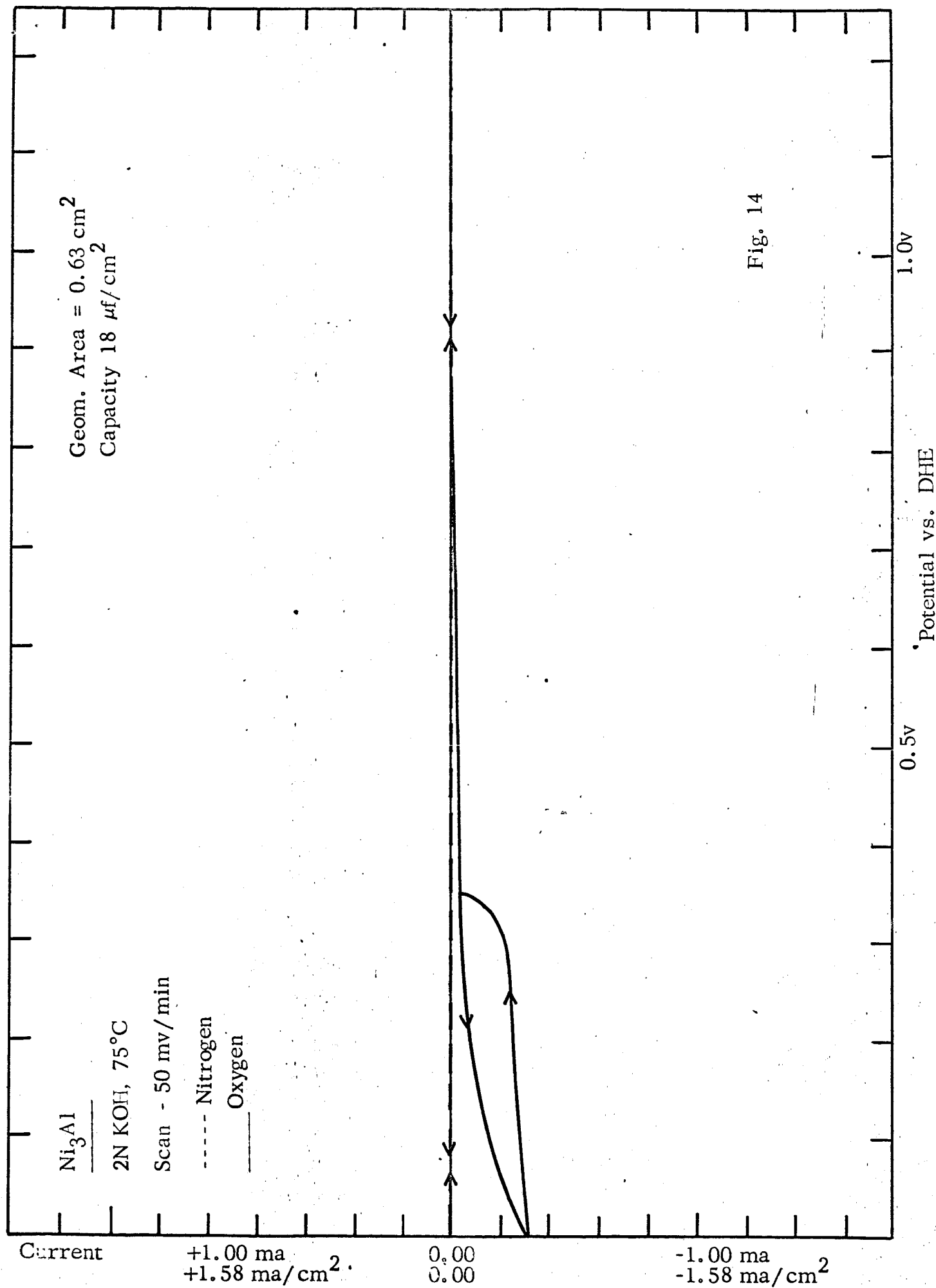


Fig. 13



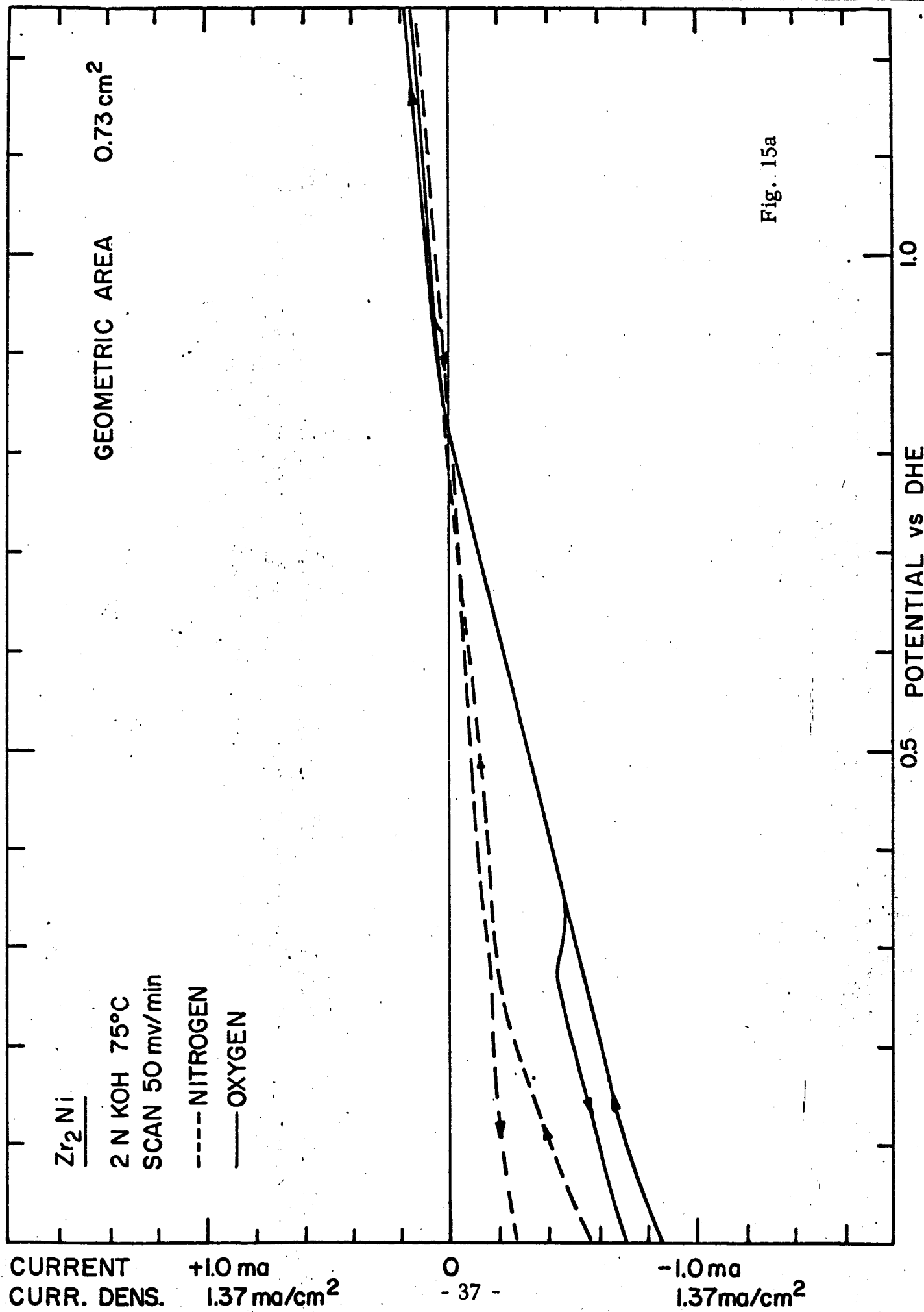
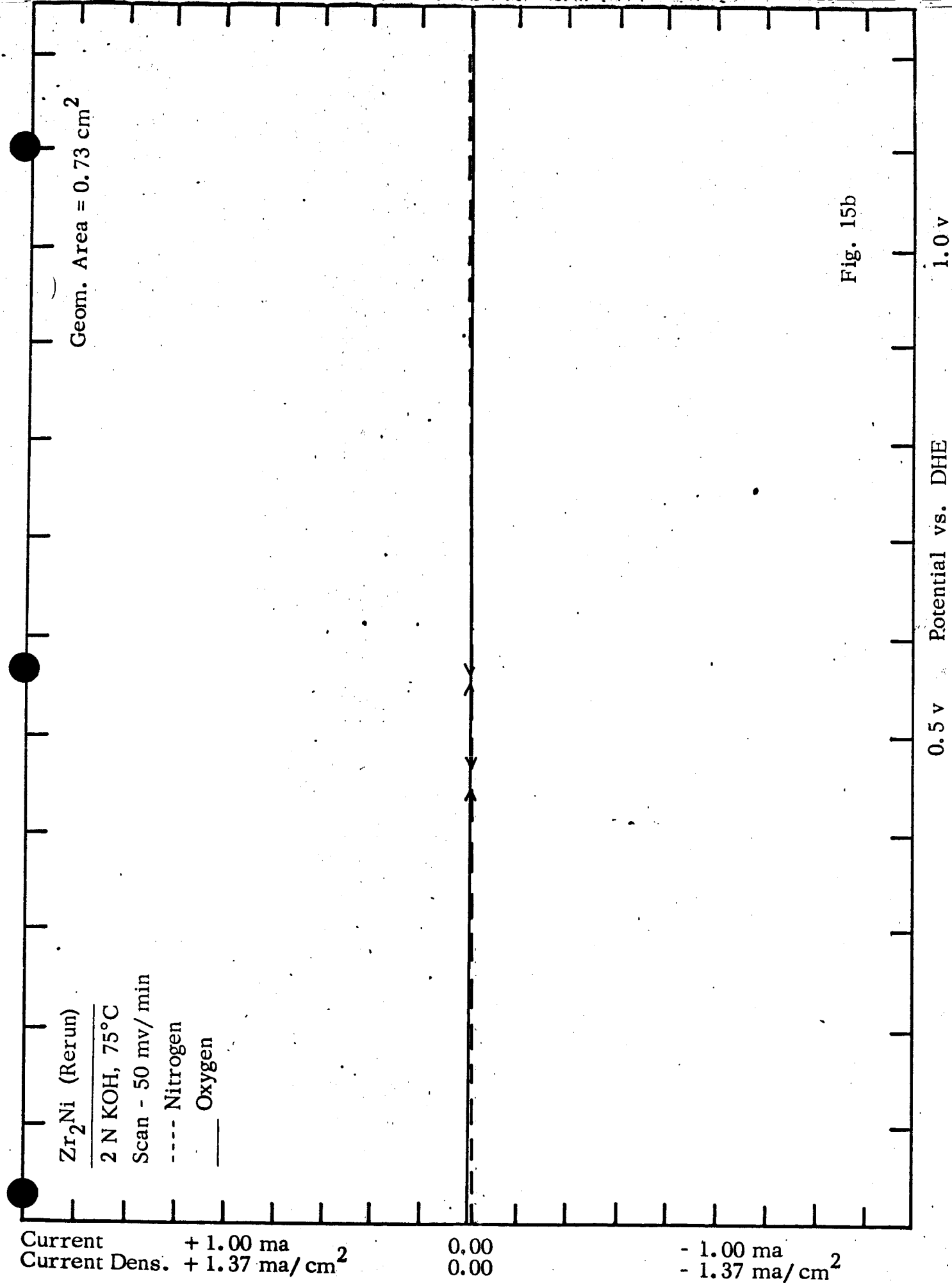


Fig. 15a



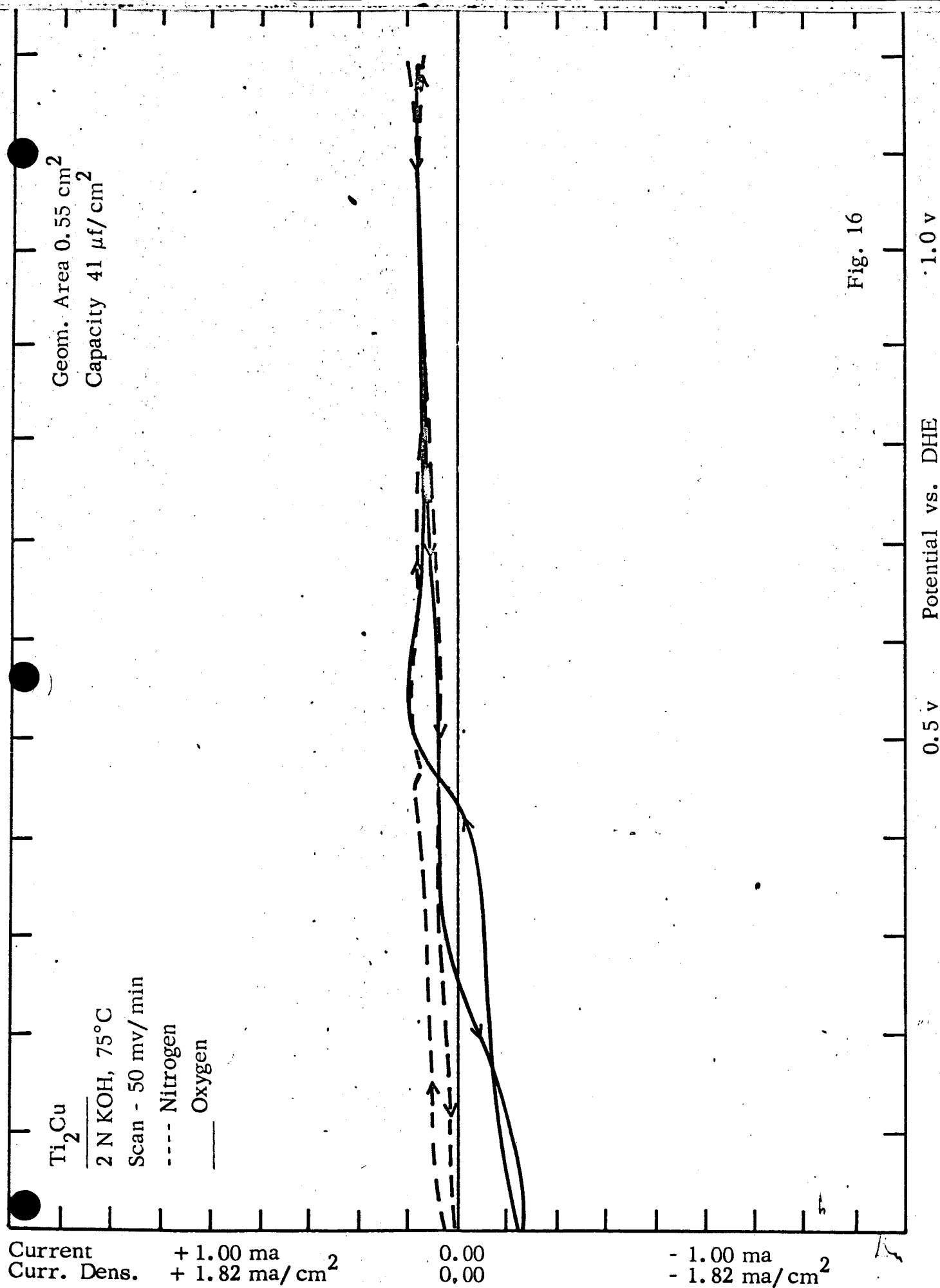


Fig. 16

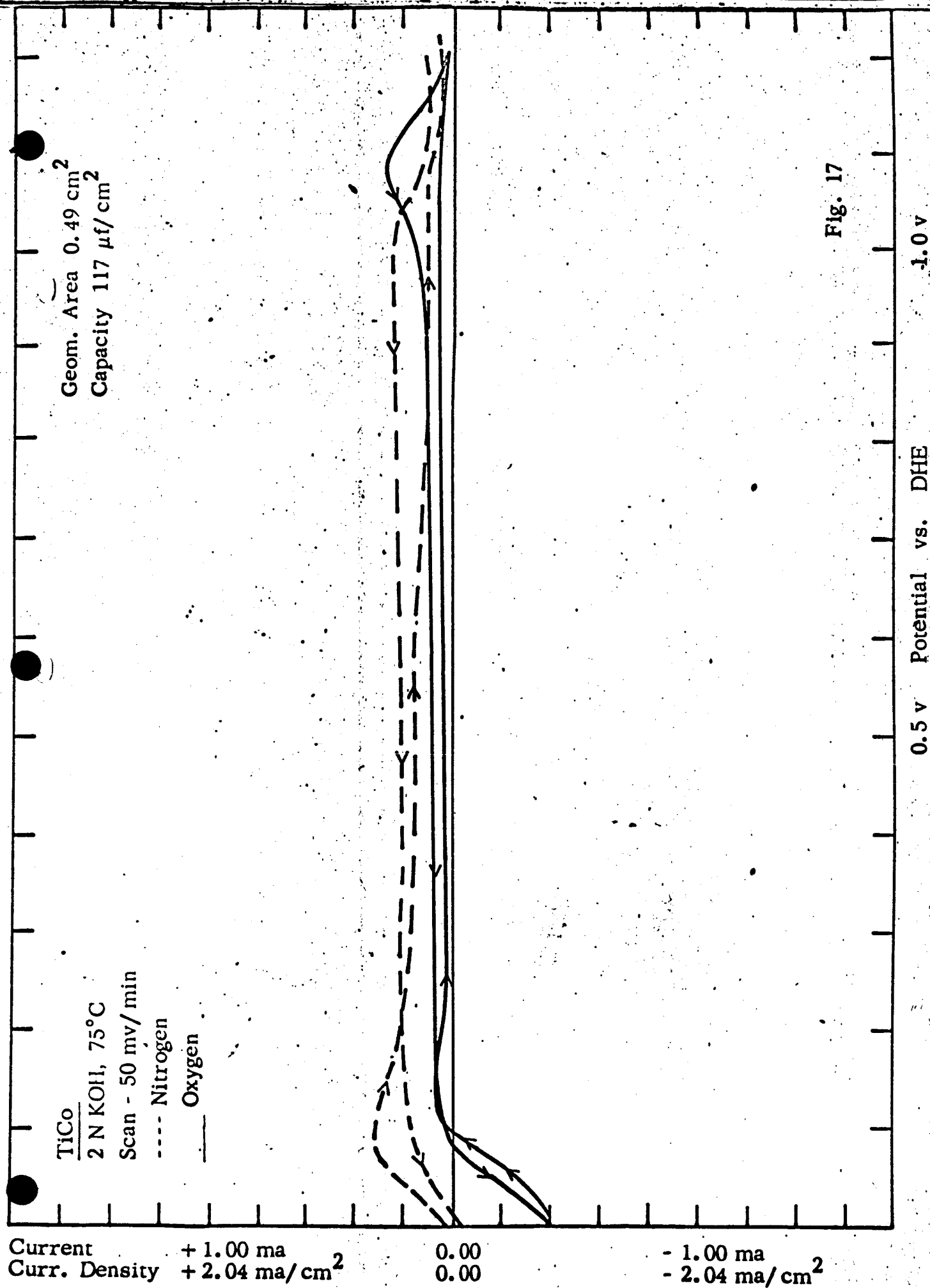


Fig. 17

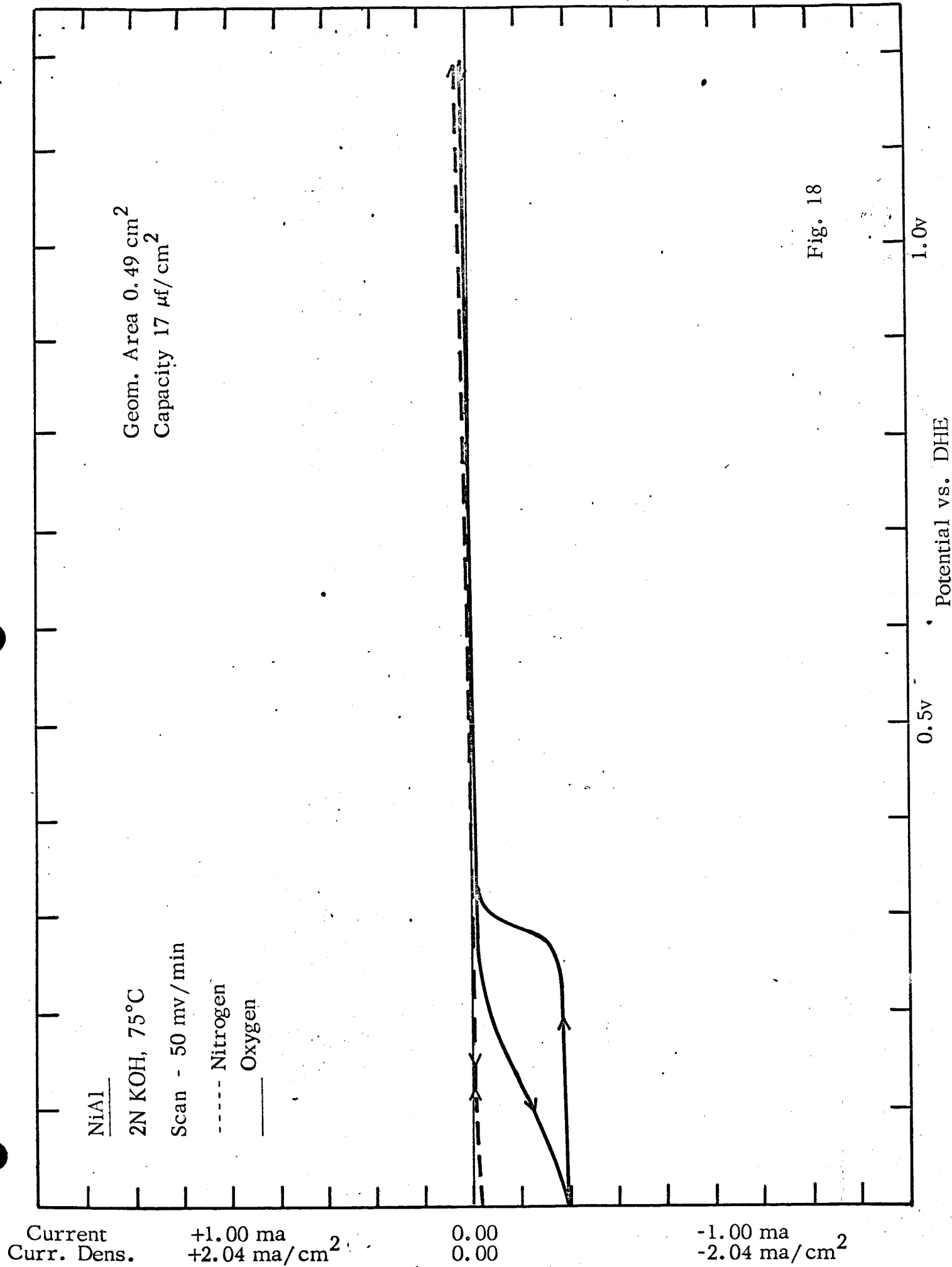
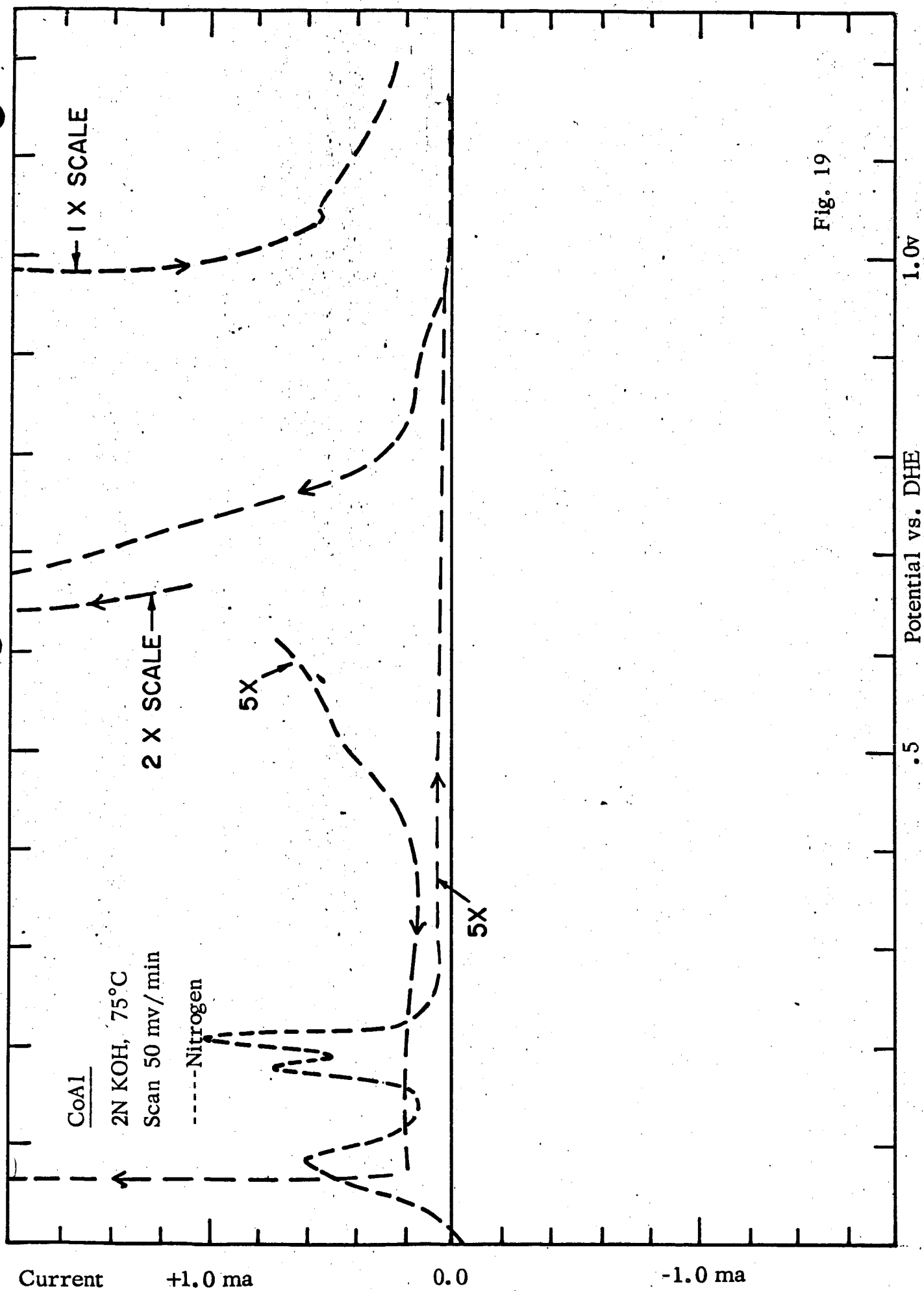


Fig. 18



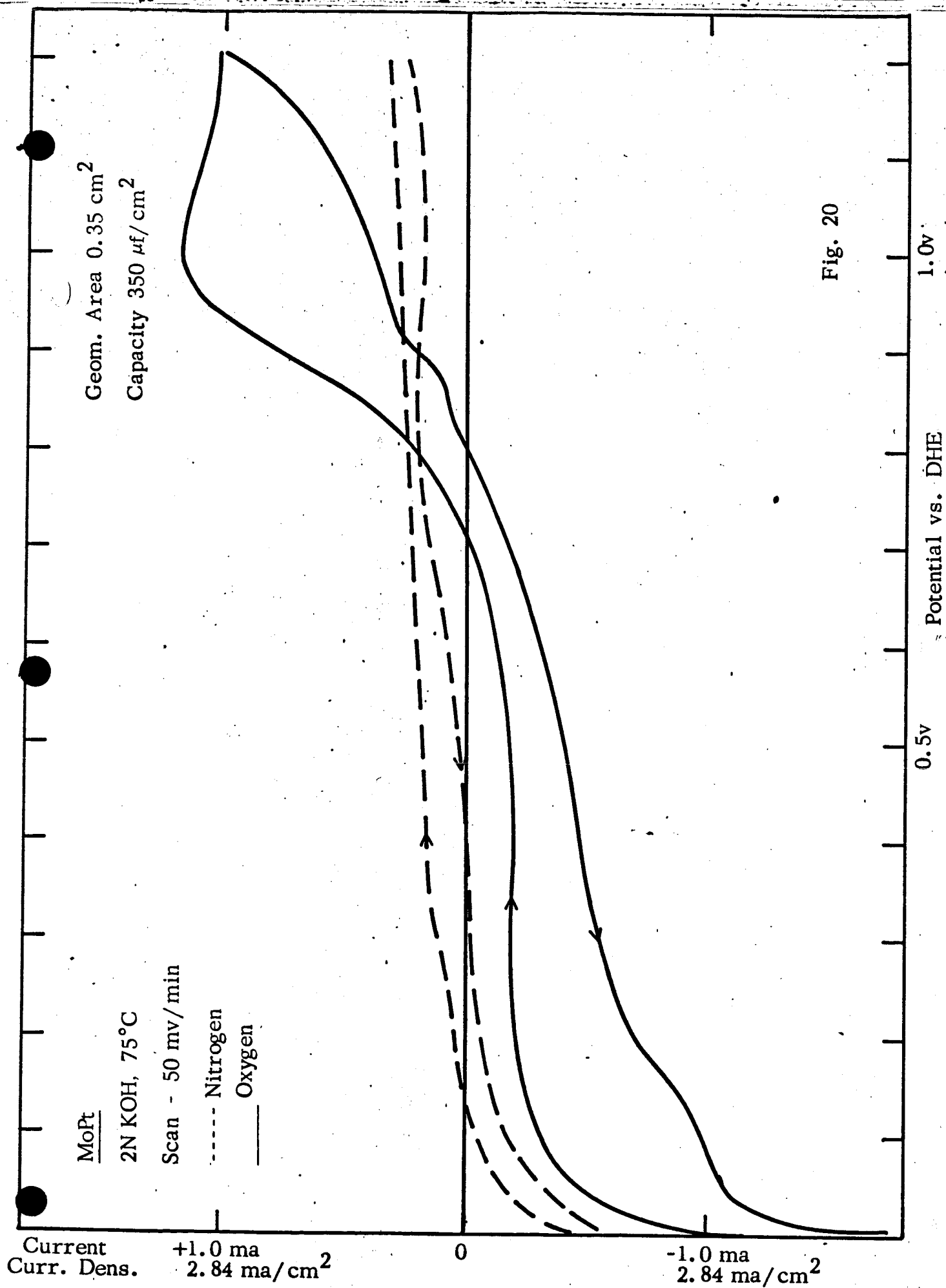


Fig. 20

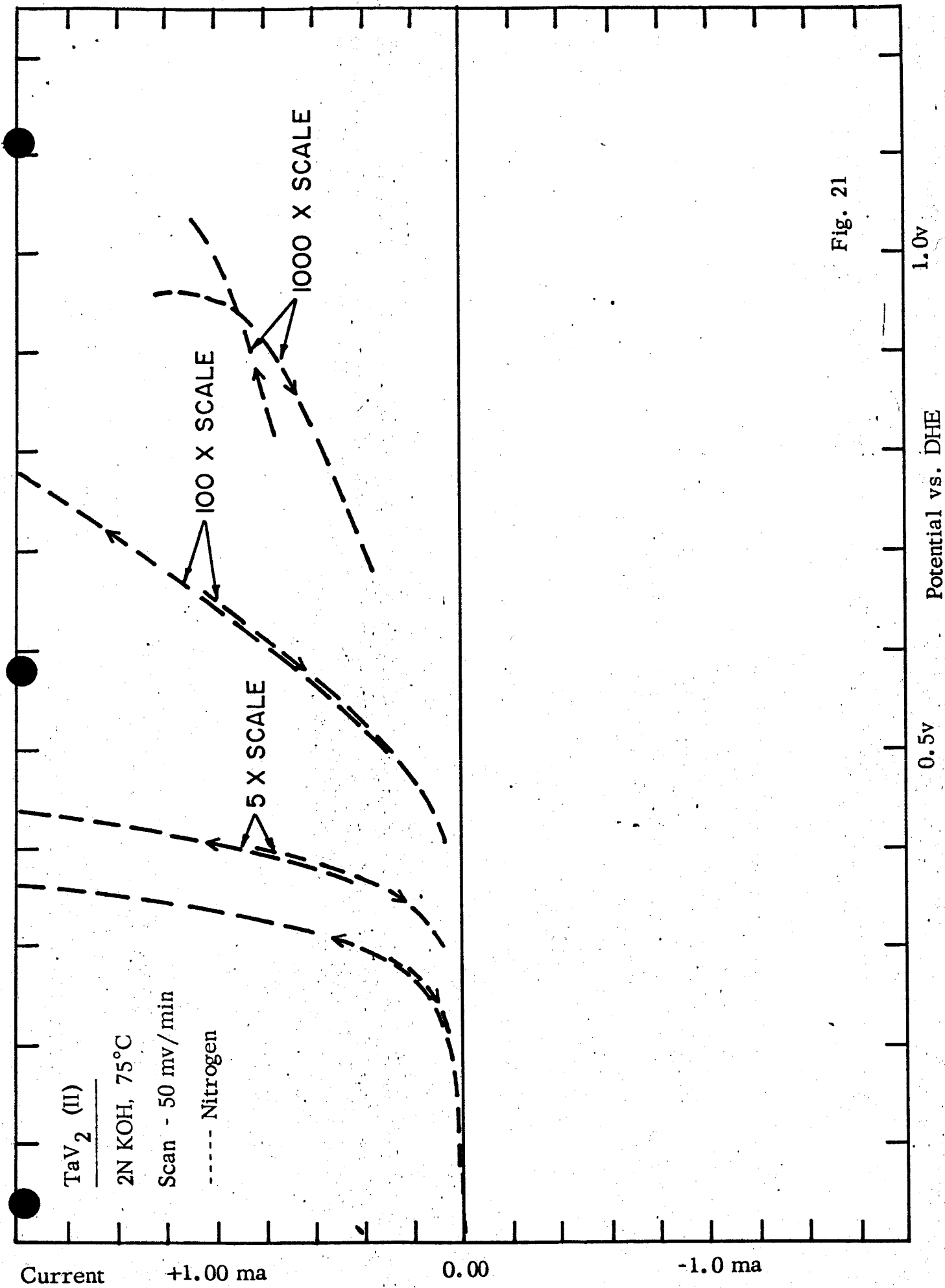


Fig. 21

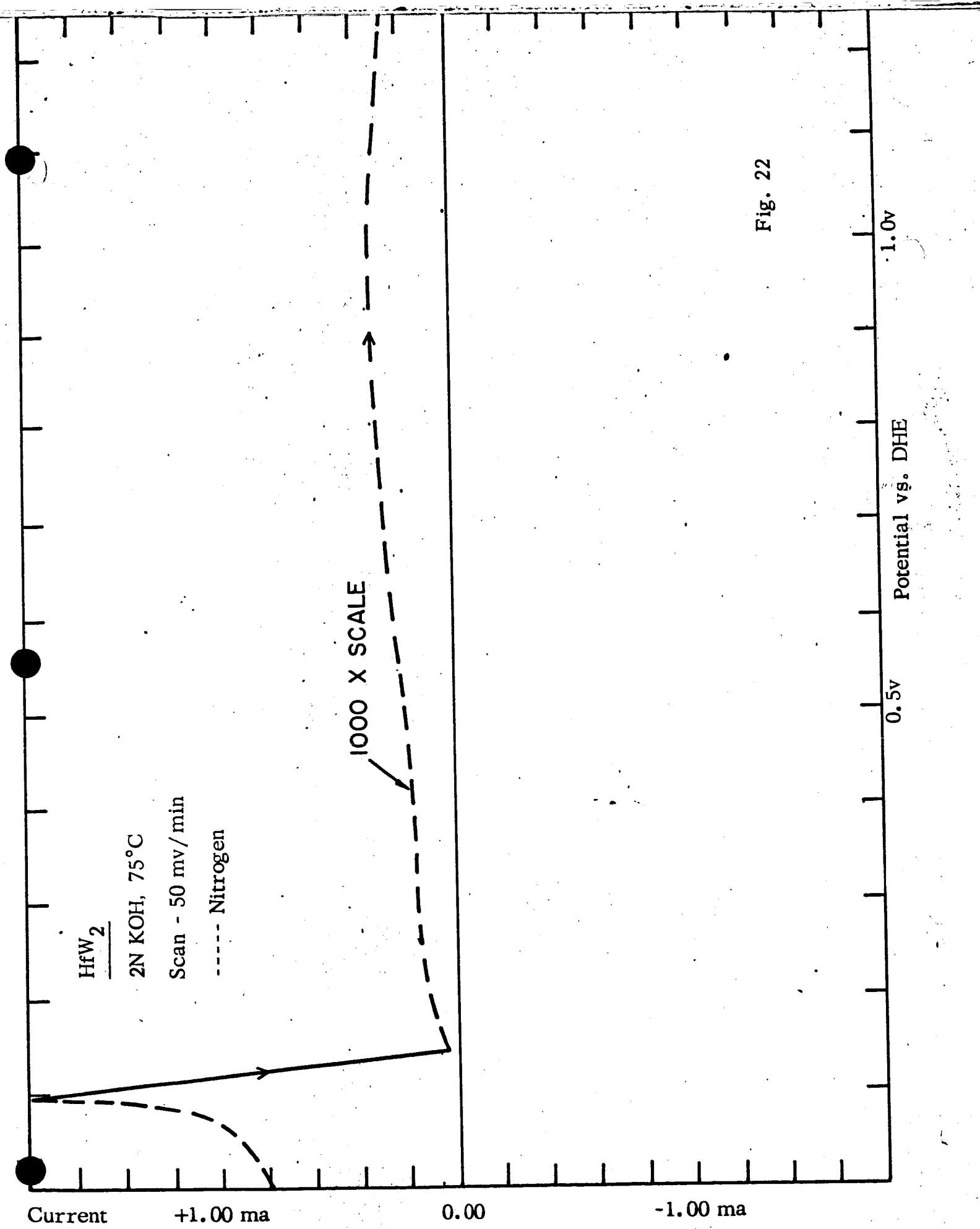


Fig. 22

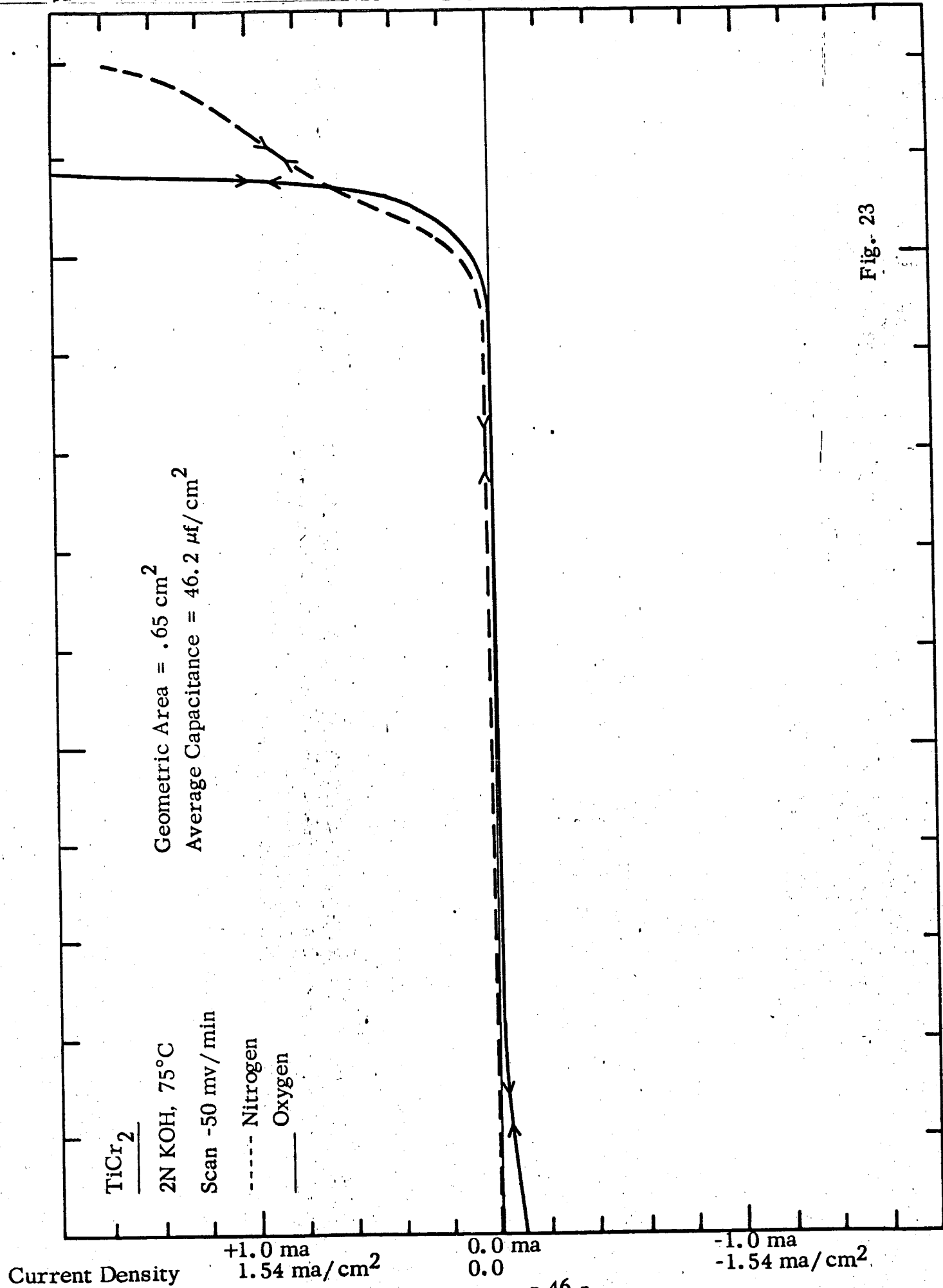
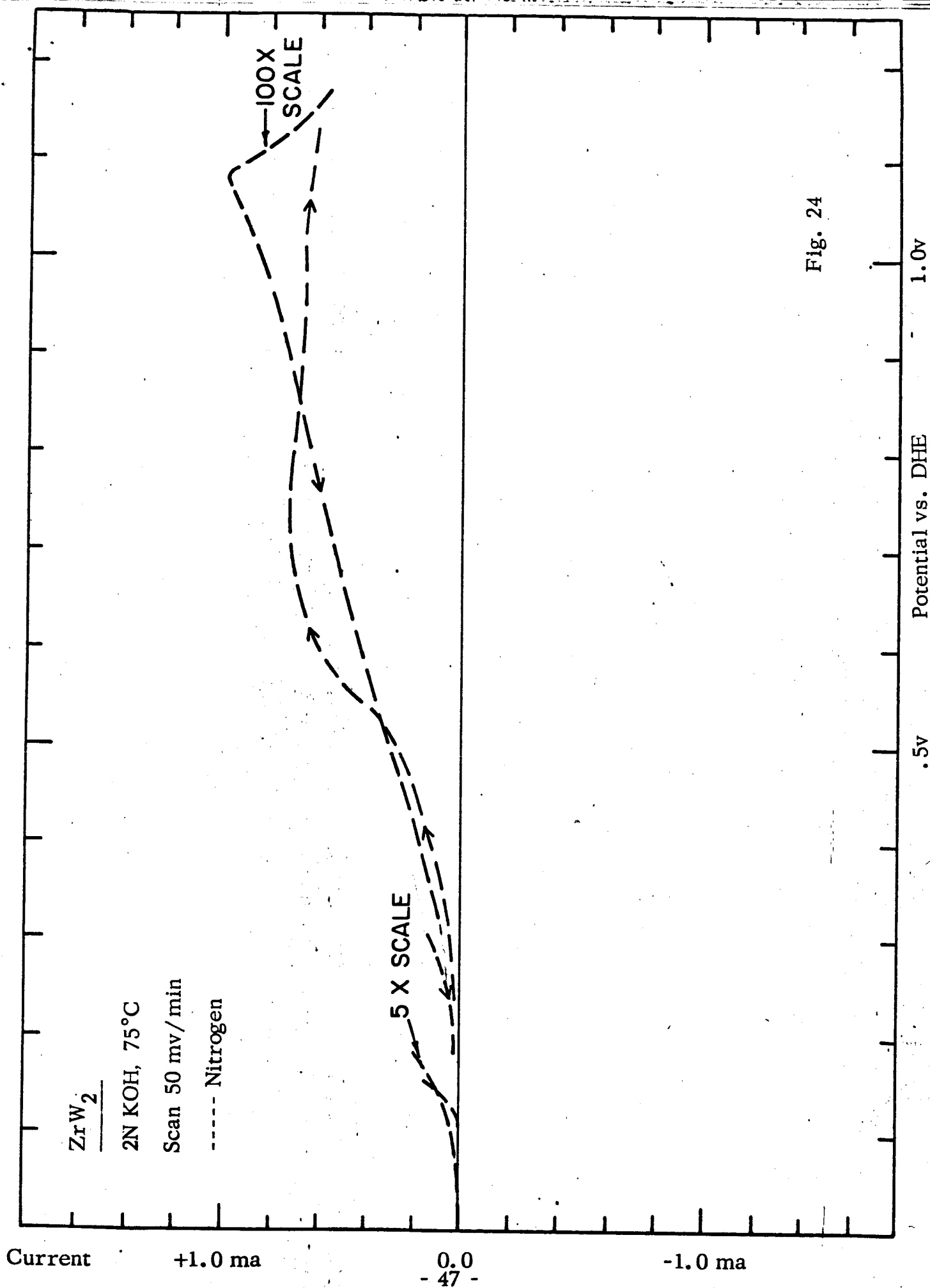


Fig. 23



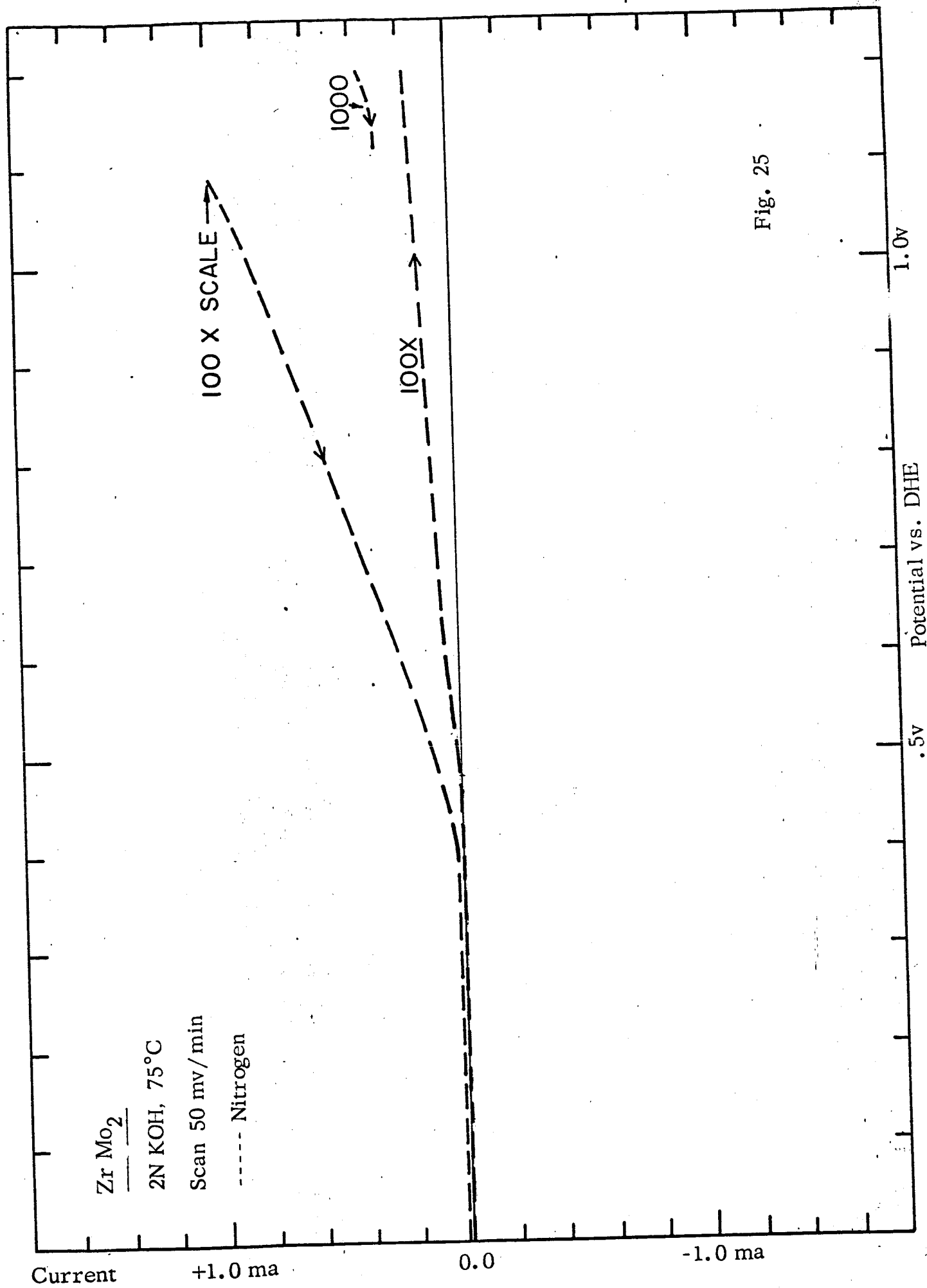


Fig. 25

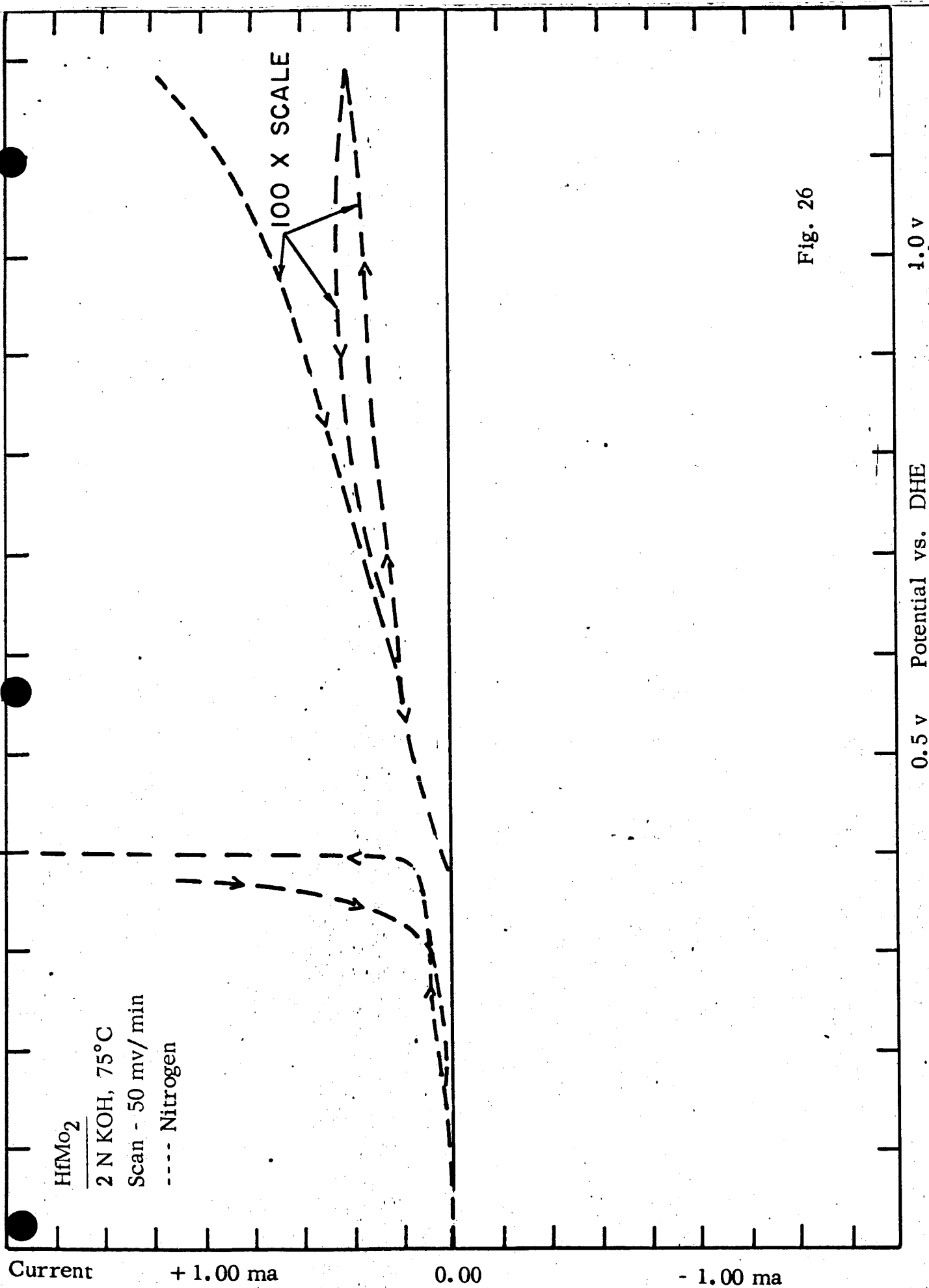


Fig. 26

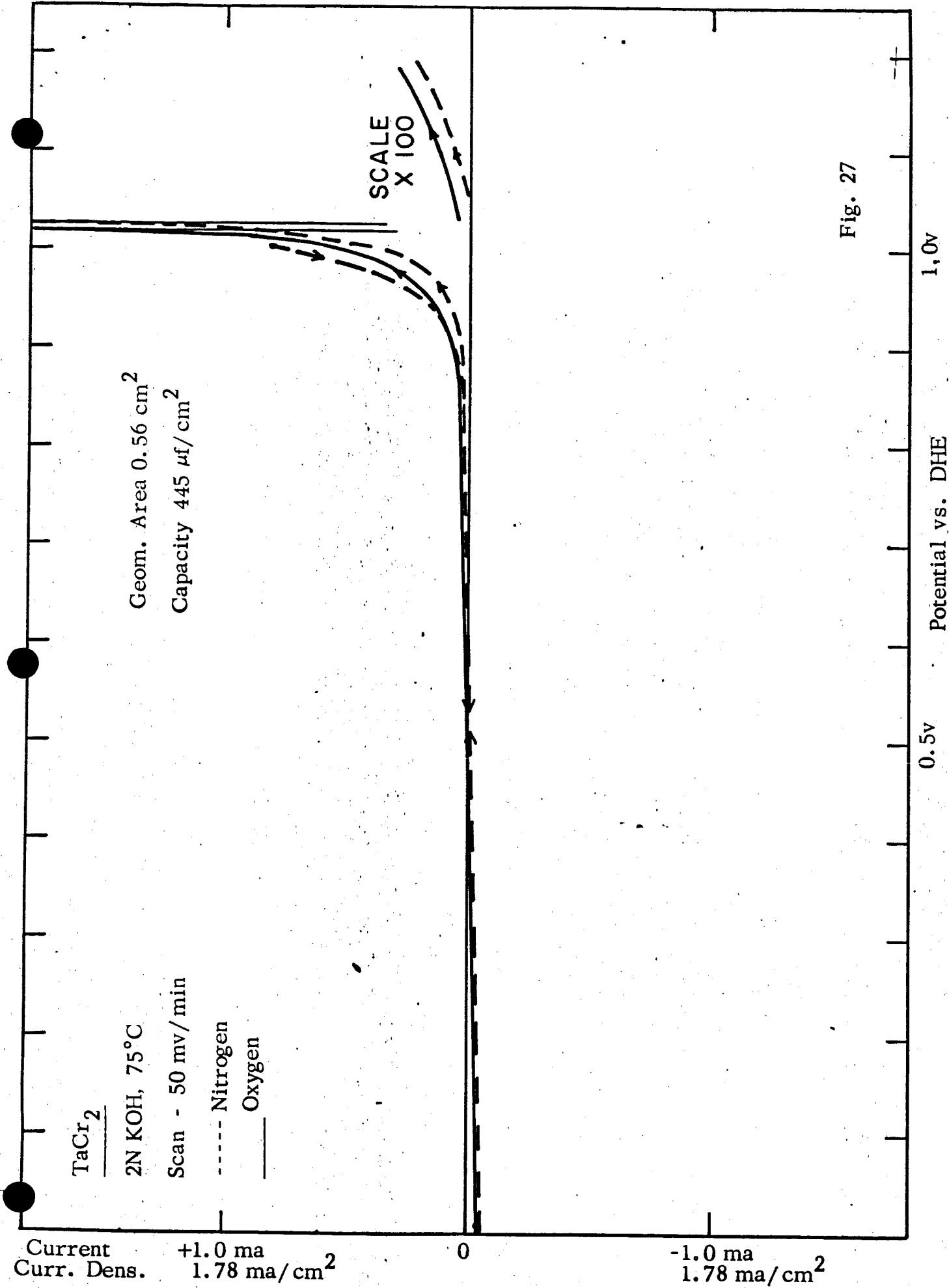


Fig. 27

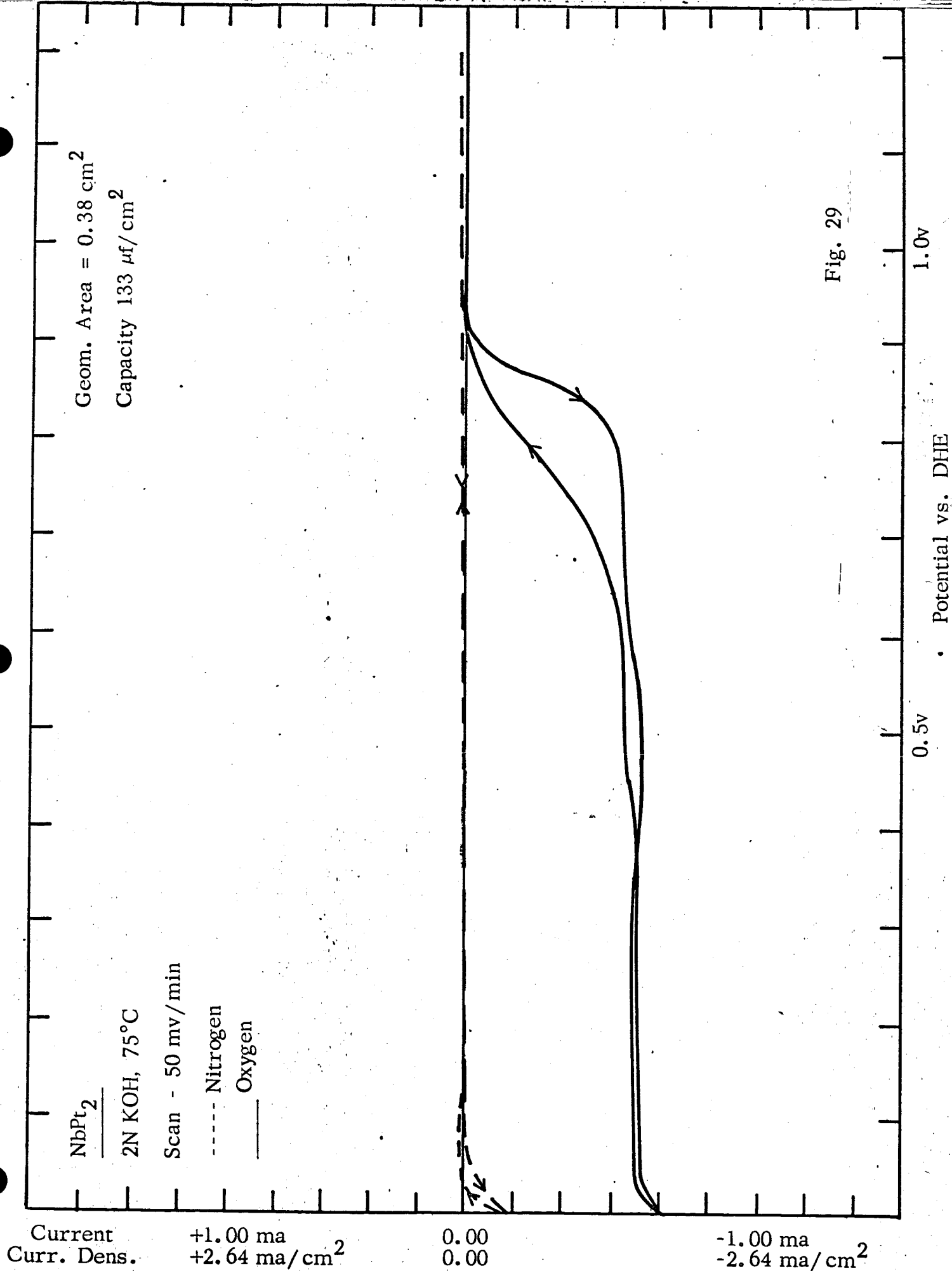
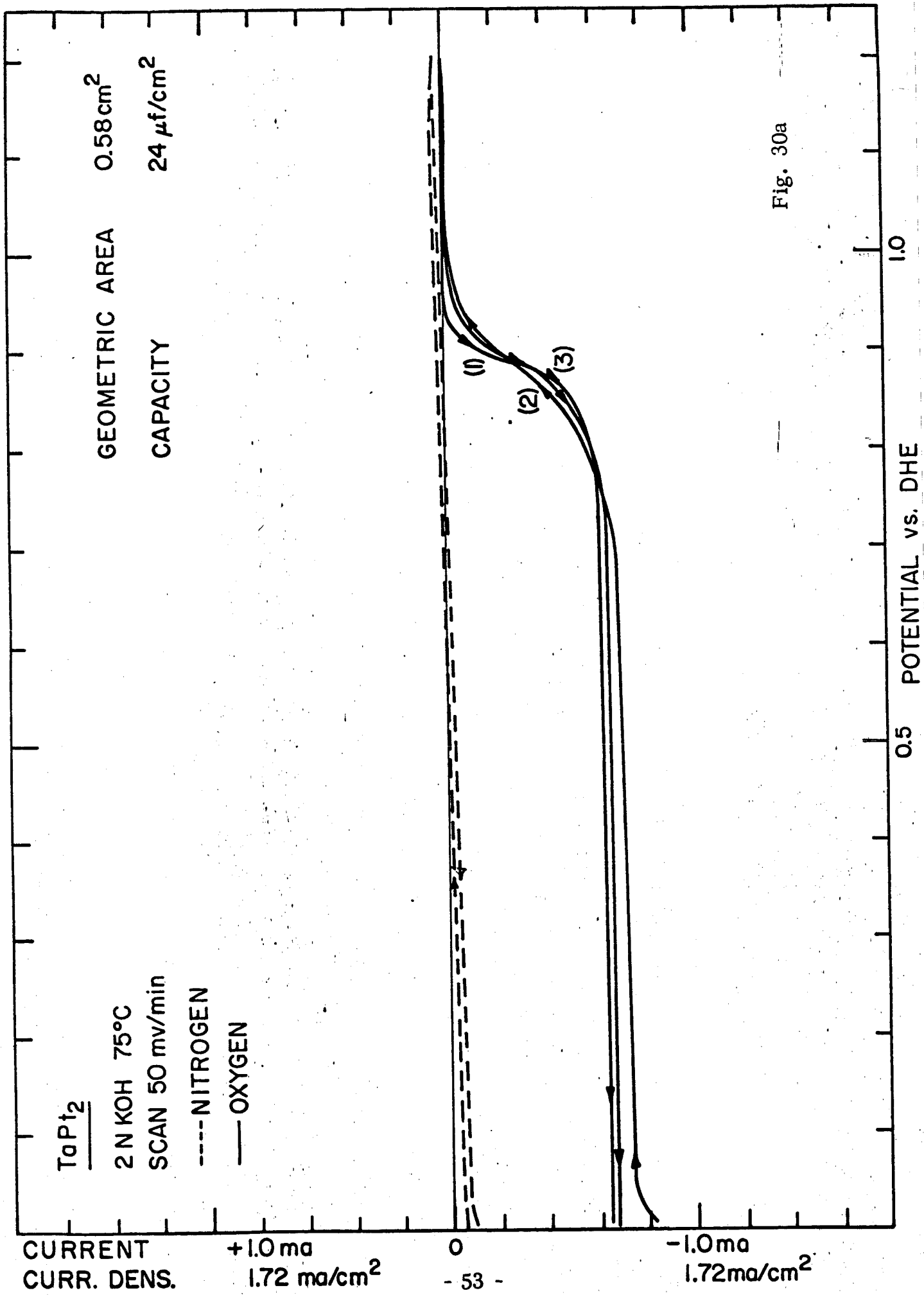


Fig. 29



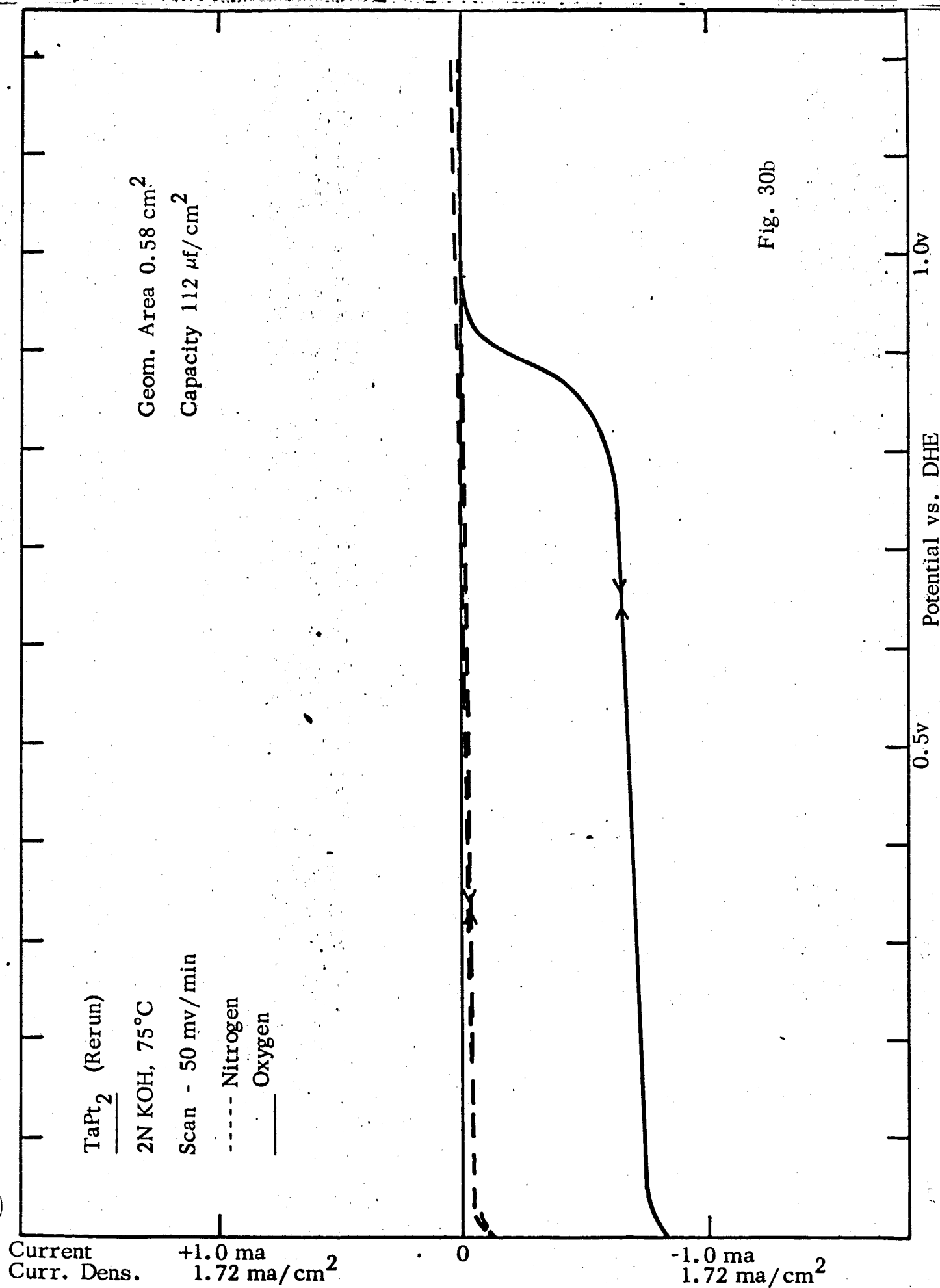
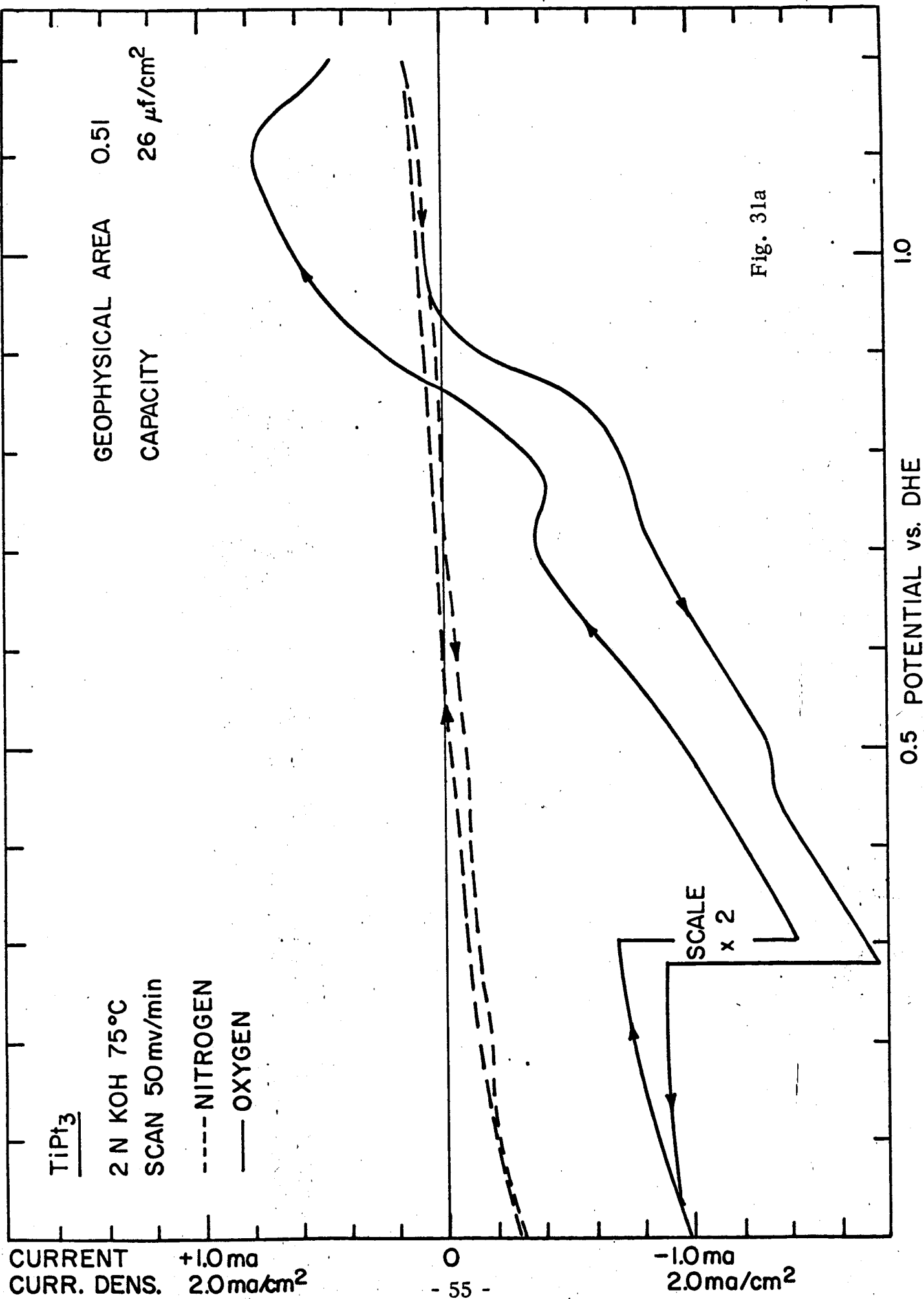


Fig. 30b



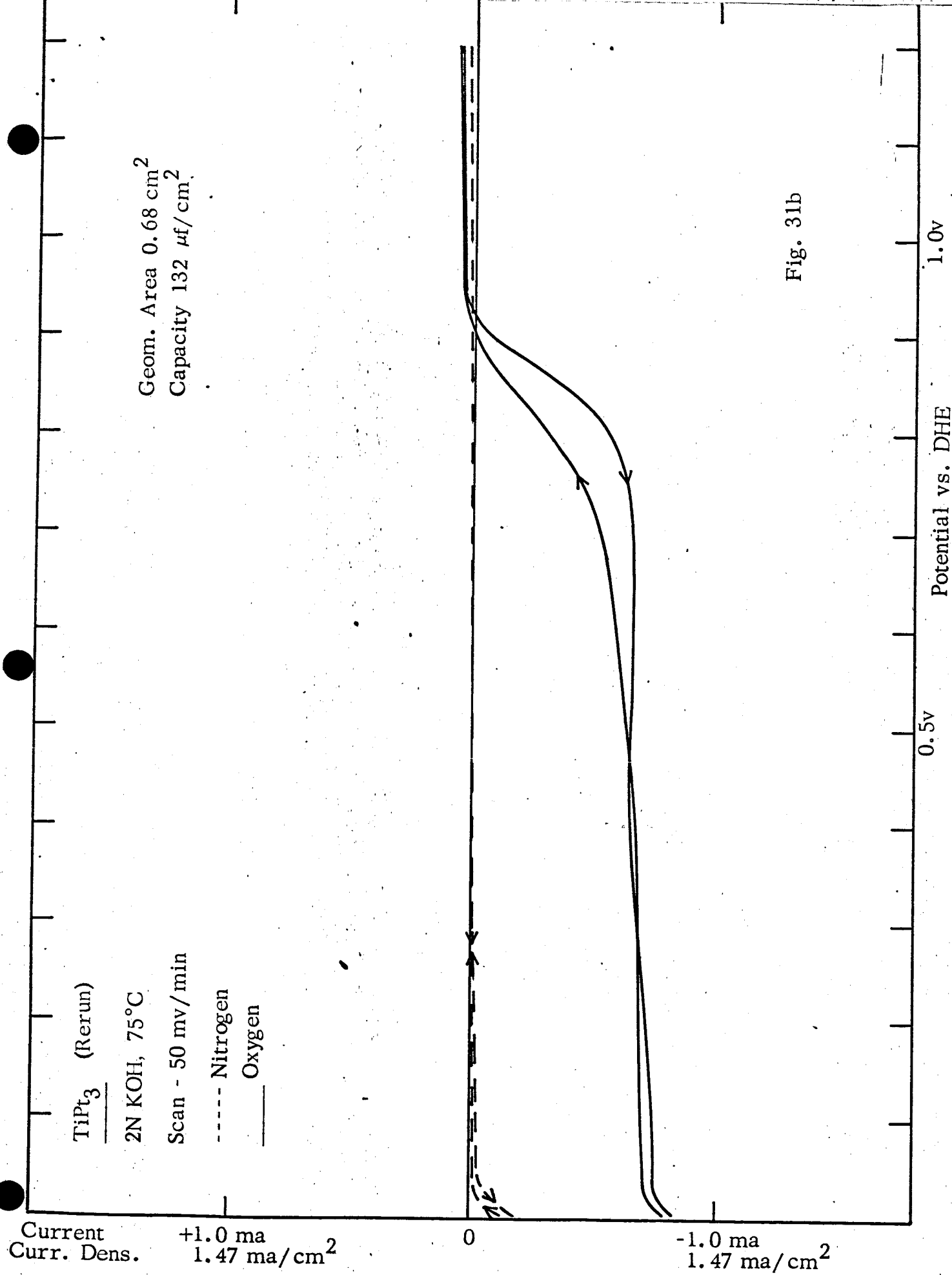
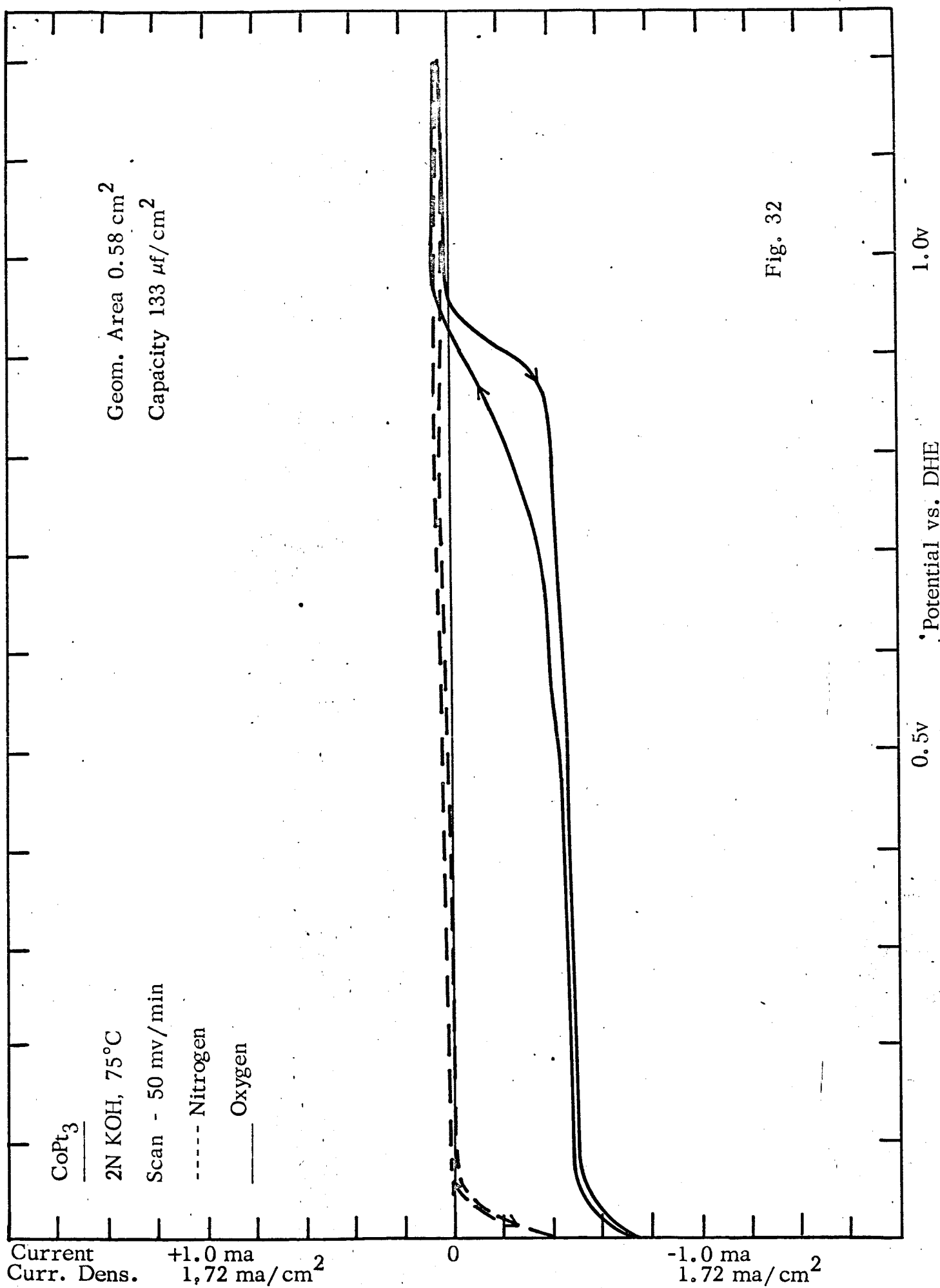


Fig. 31b



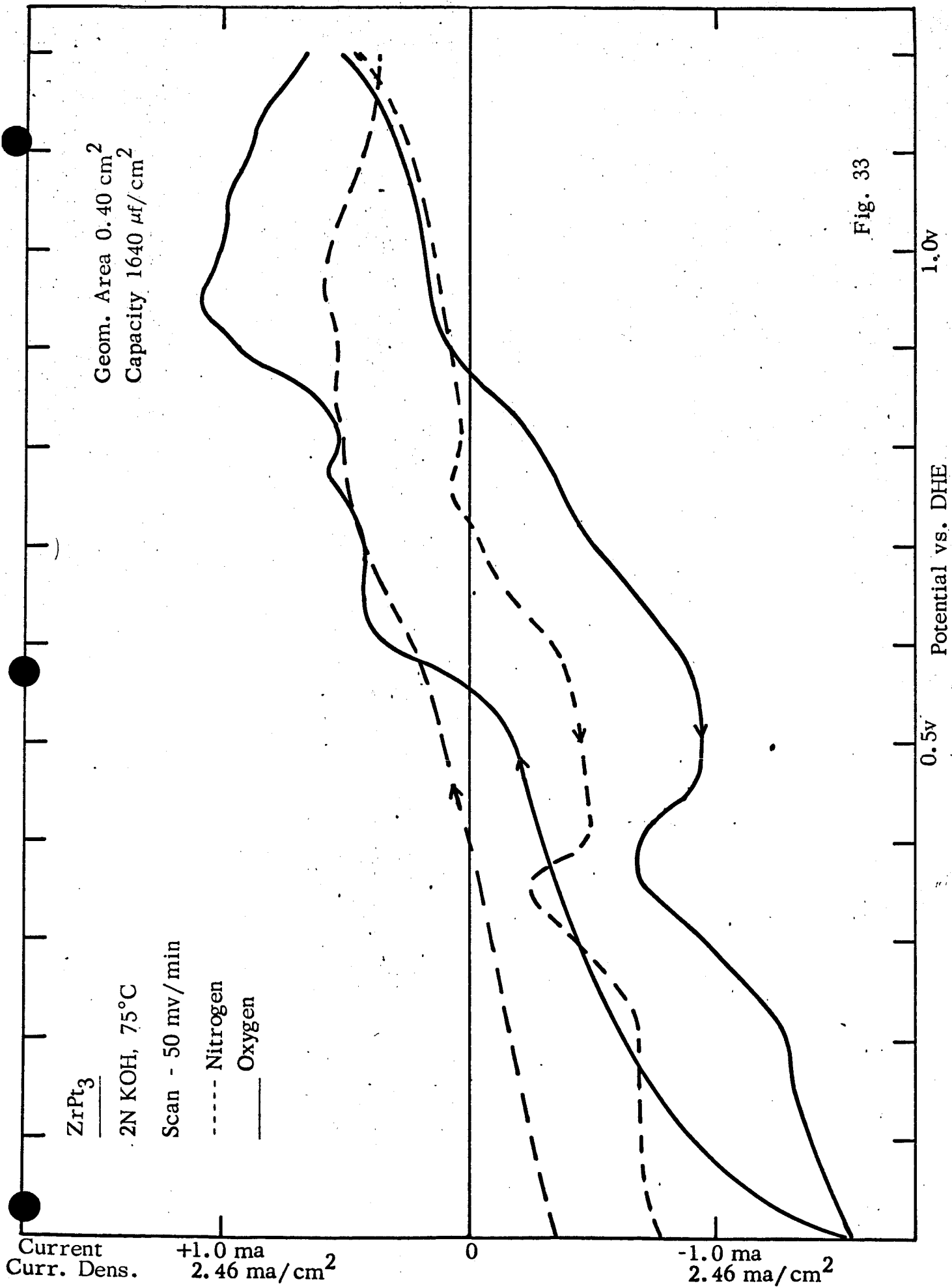
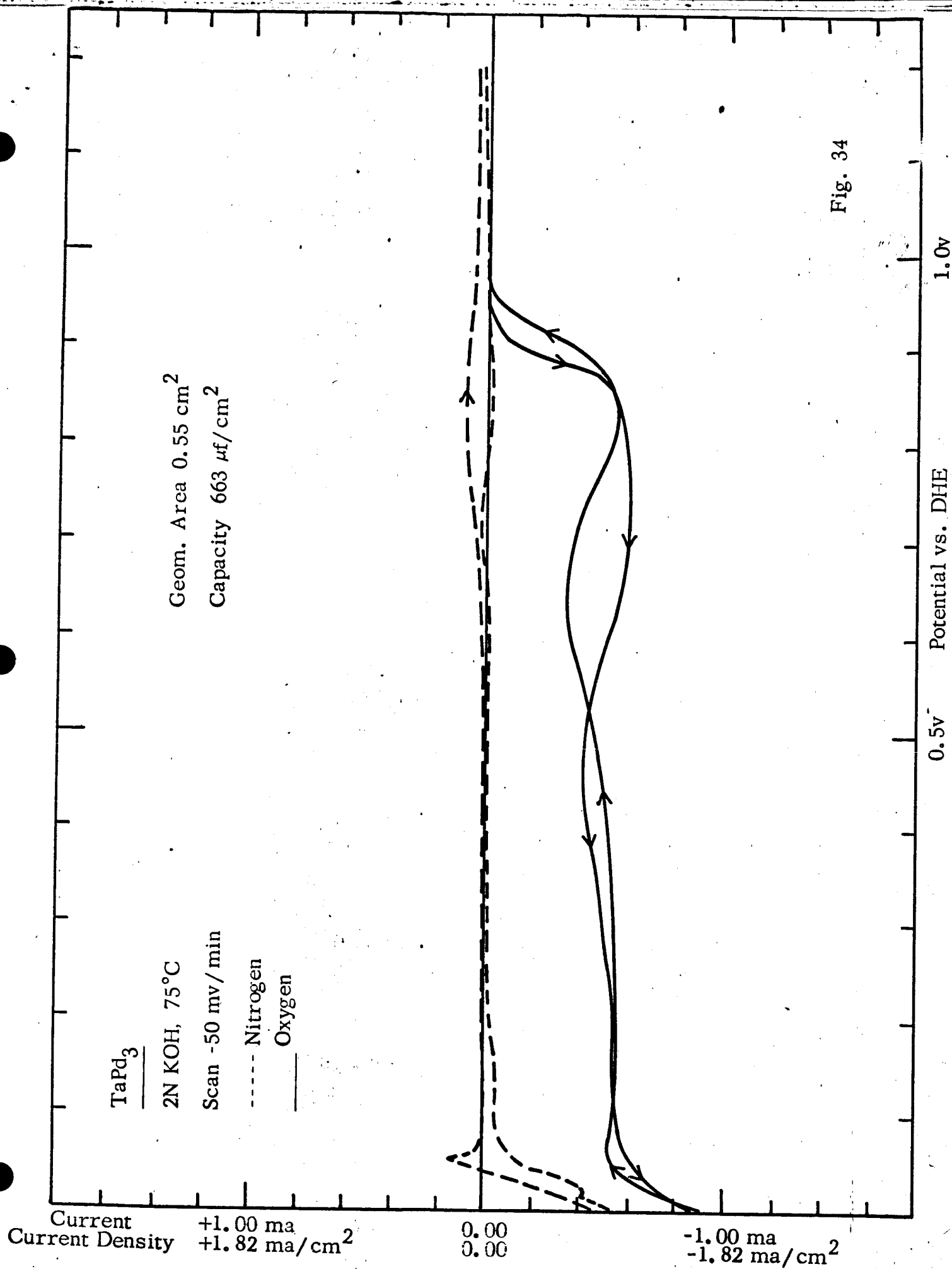
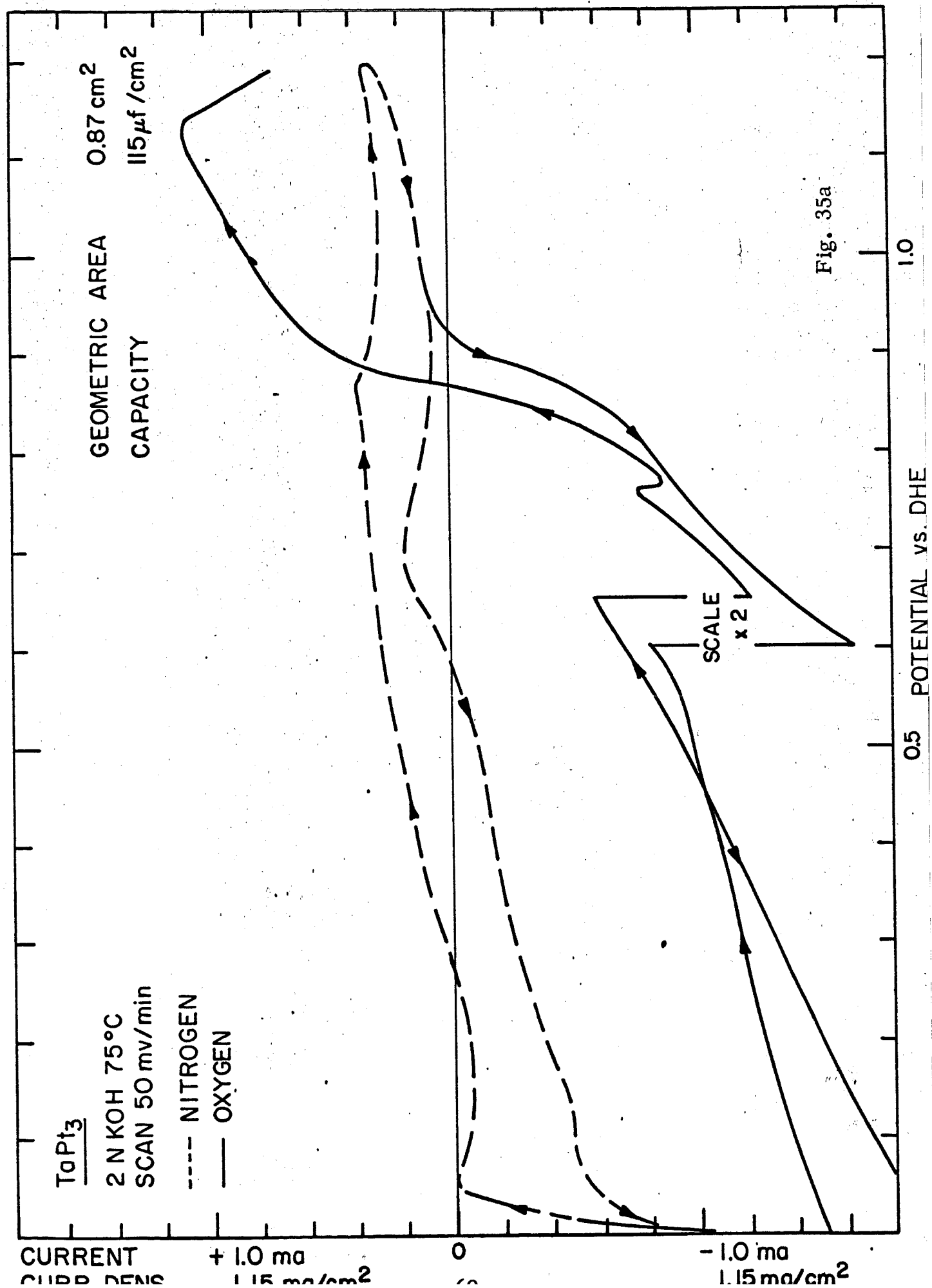


Fig. 33





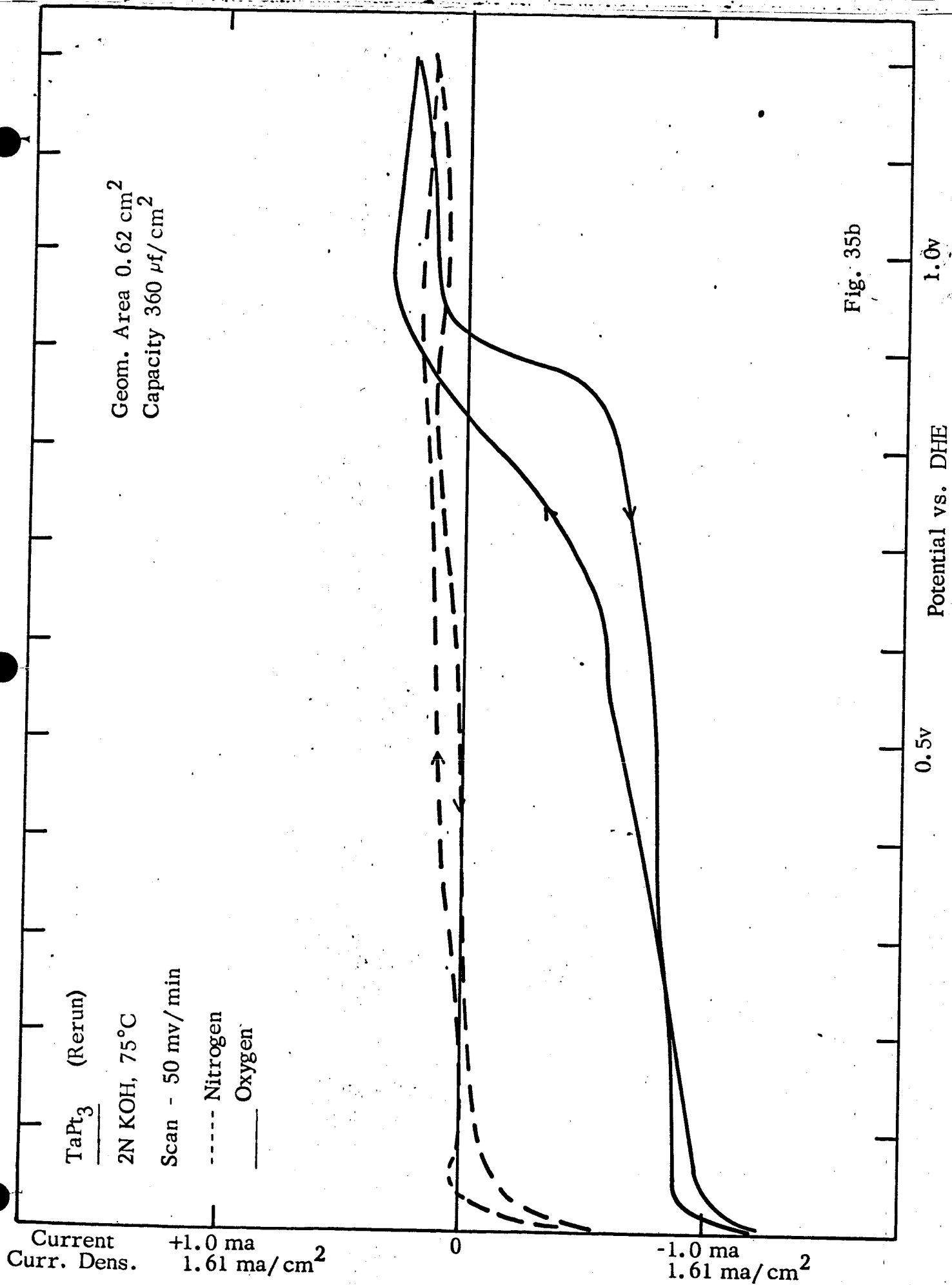


Fig. 35b

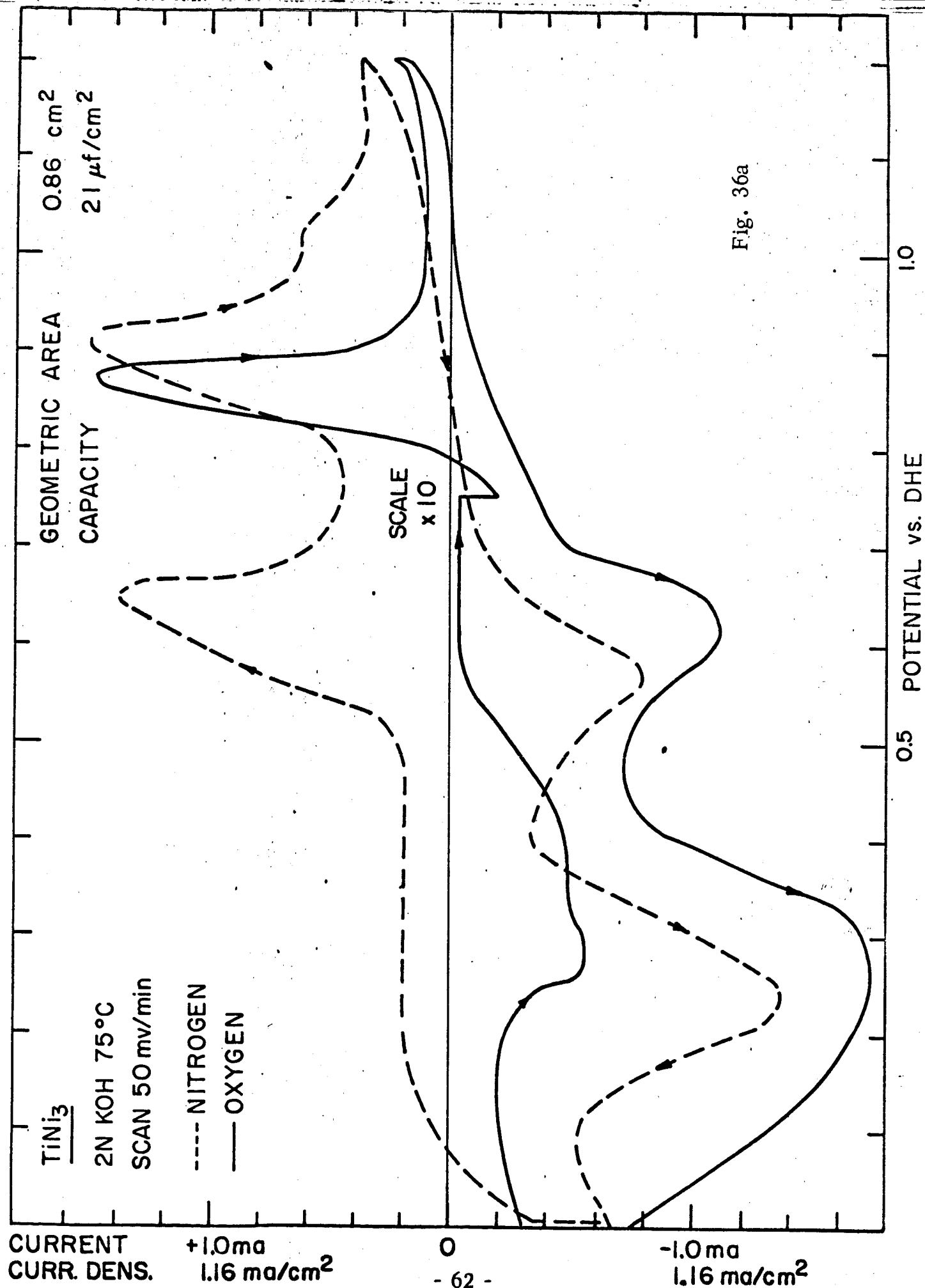
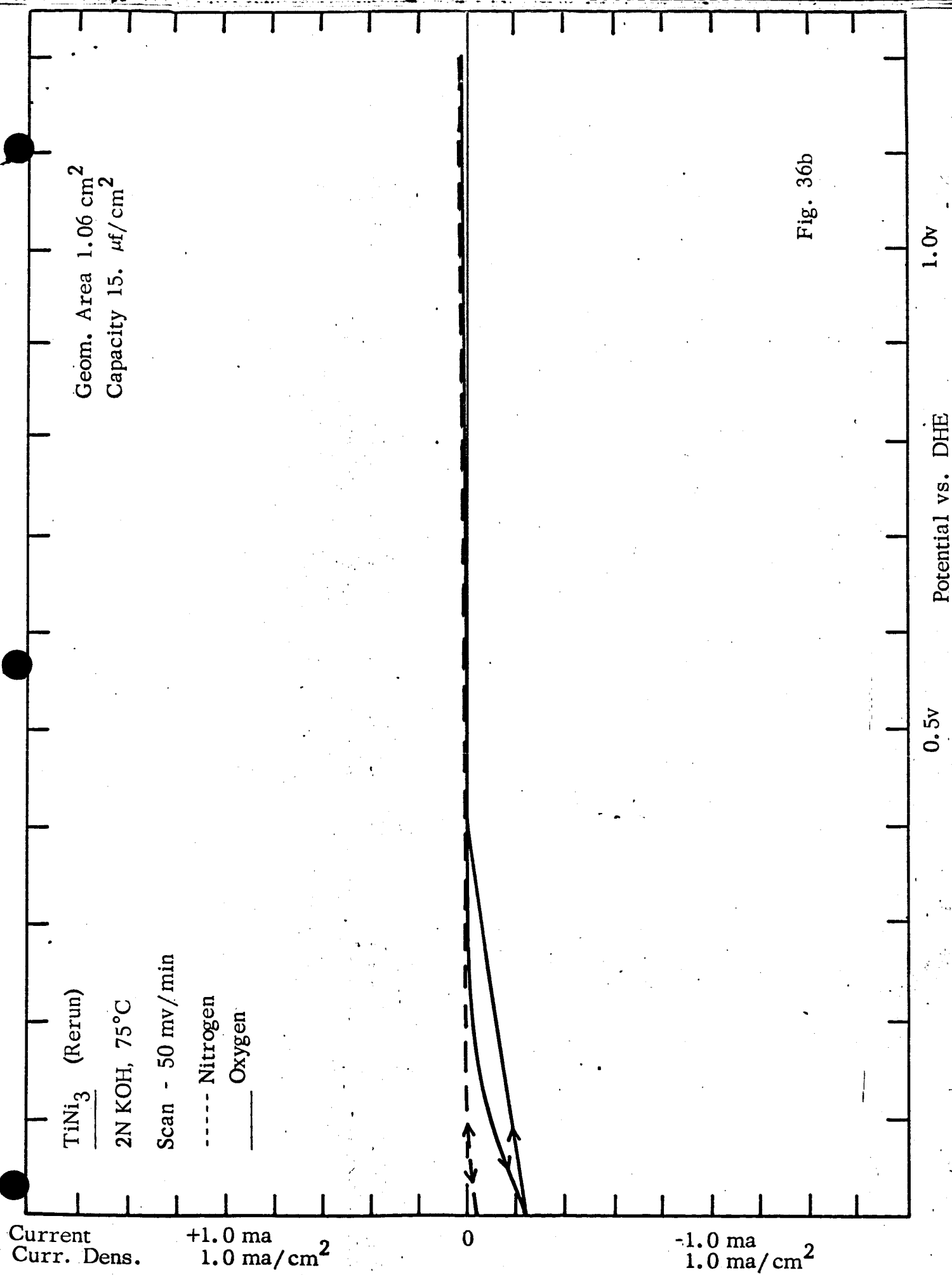


Fig. 36a



Current +1.00 ma
Current Density +2.00 ma/cm²

V Pt₃

2N KOH, 75°C
Scan -50 Mv/min

----- Nitrogen
_____ Oxygen

Average

C = 140 μf/cm²

Geom. Area 0.50 cm²

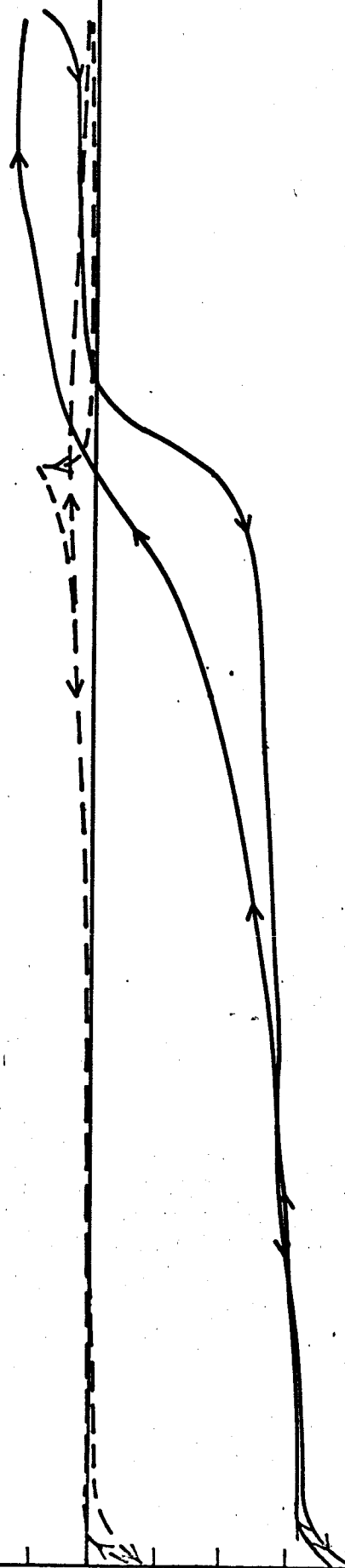


Fig. 37

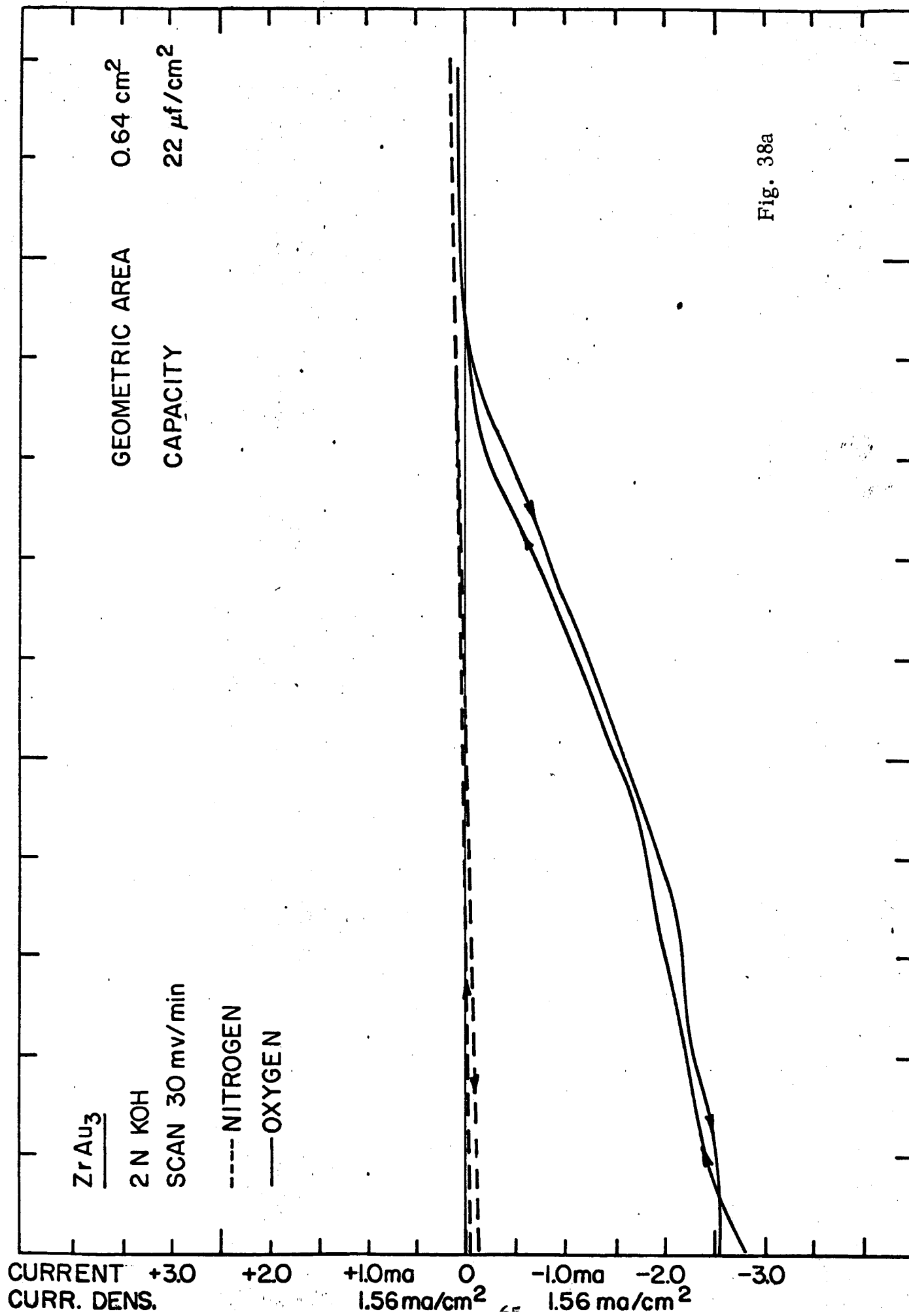
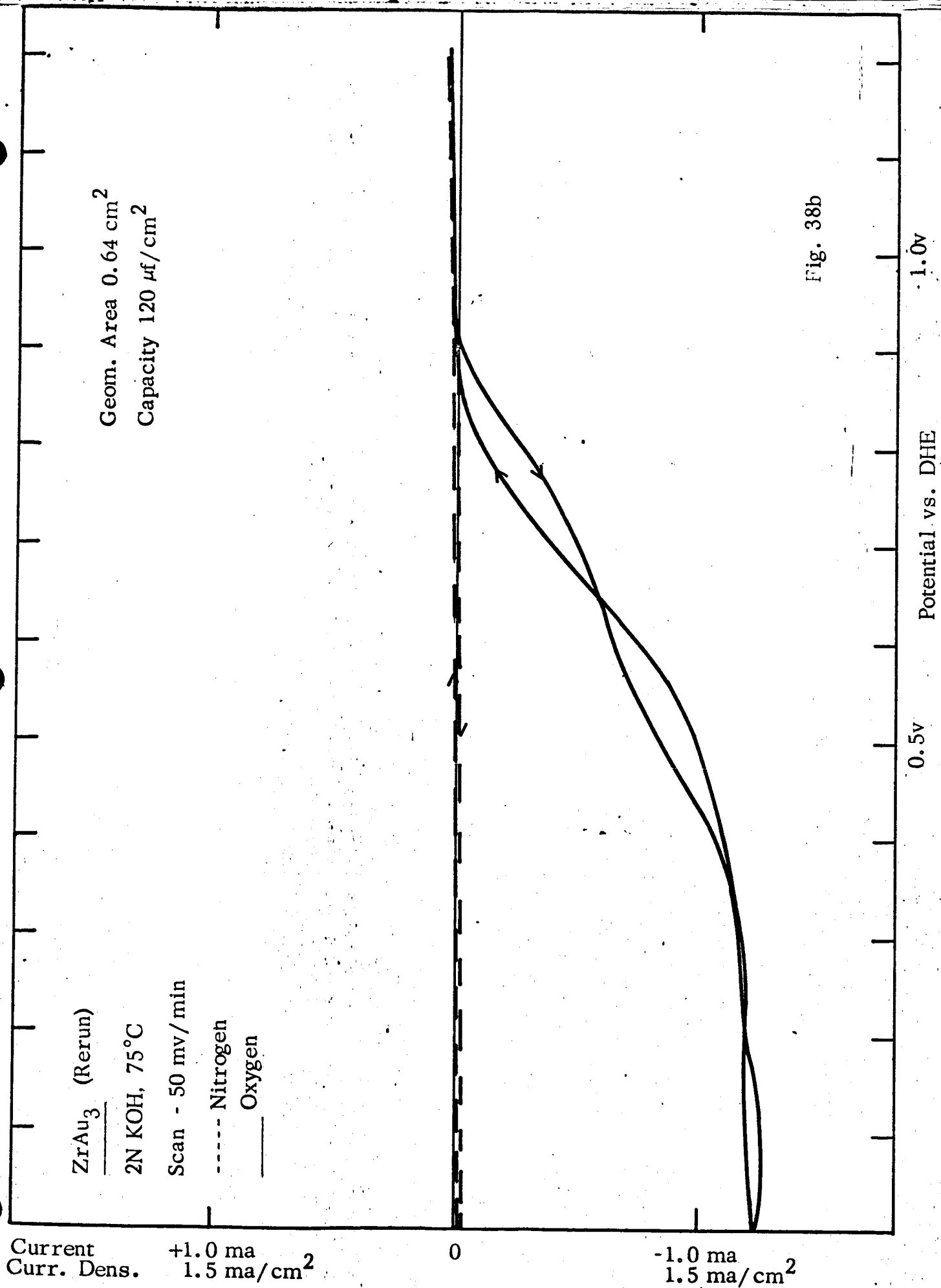
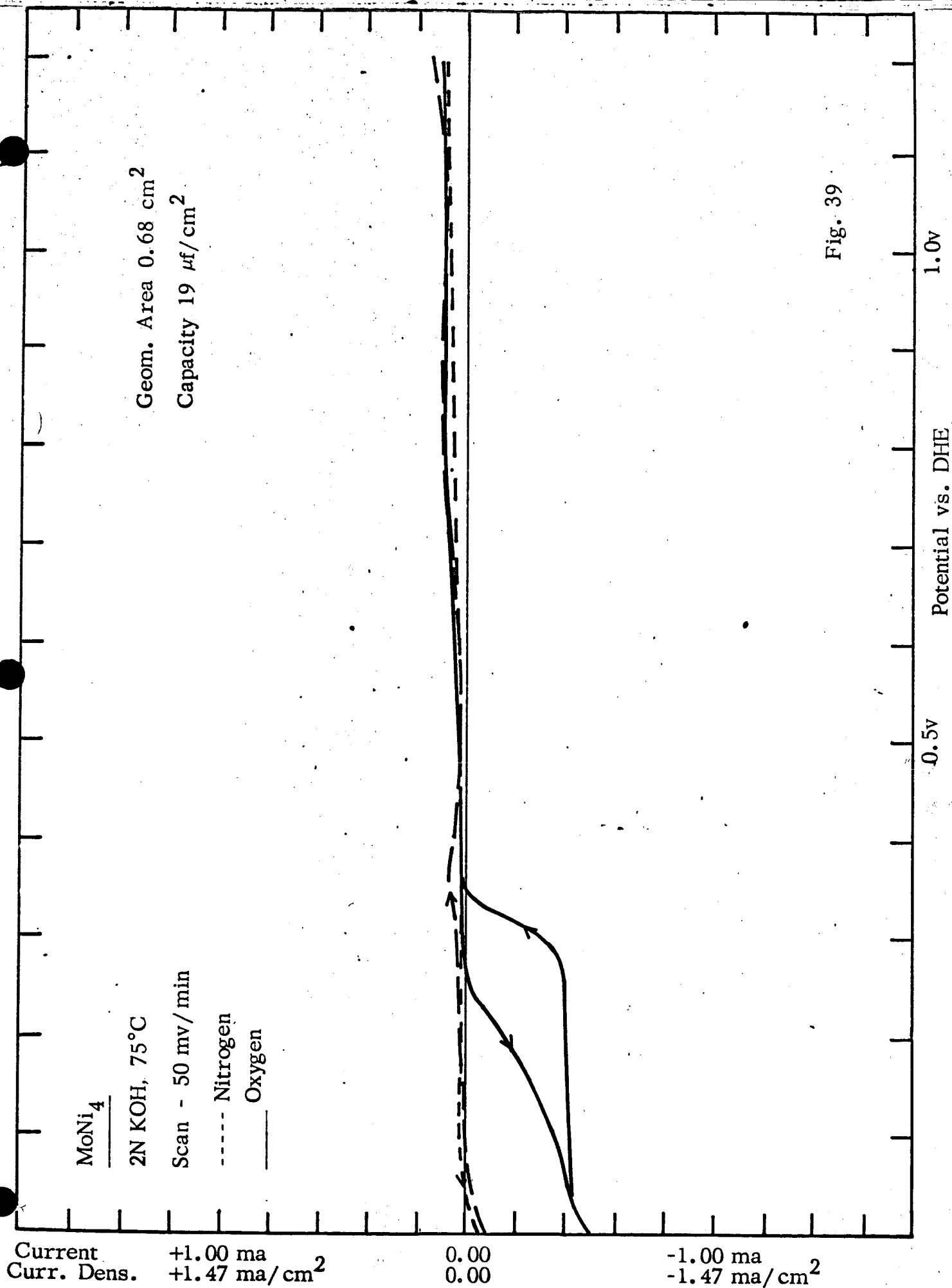
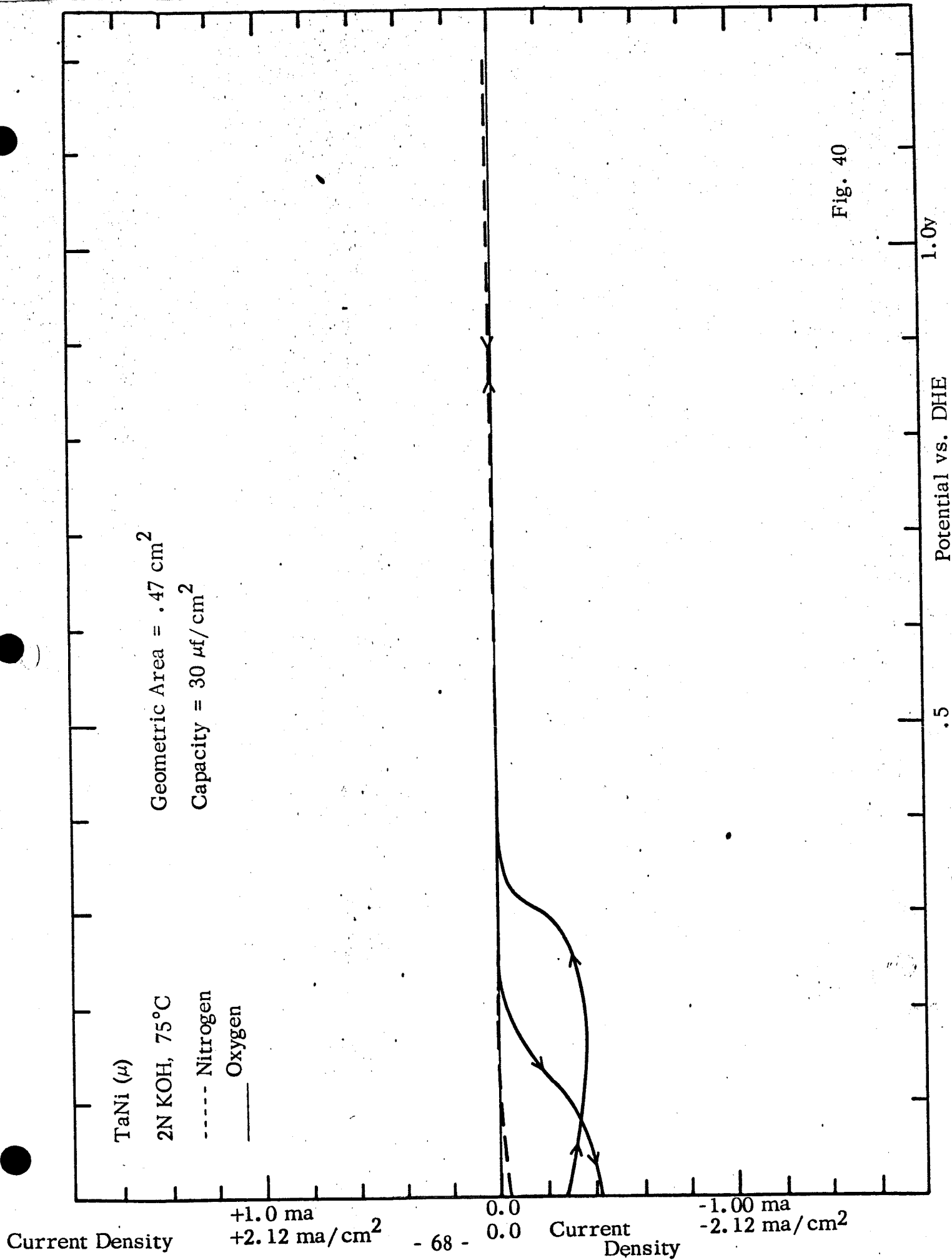


Fig. 38a







Current
Curr. Dens.

TaV₂ (I)
2N KOH, 75°C
Scan - 50 mv/min
----- Nitrogen

Geom. Area 0.72 cm²

+1.0 ma
1.39 ma/cm²

100 X SCALE

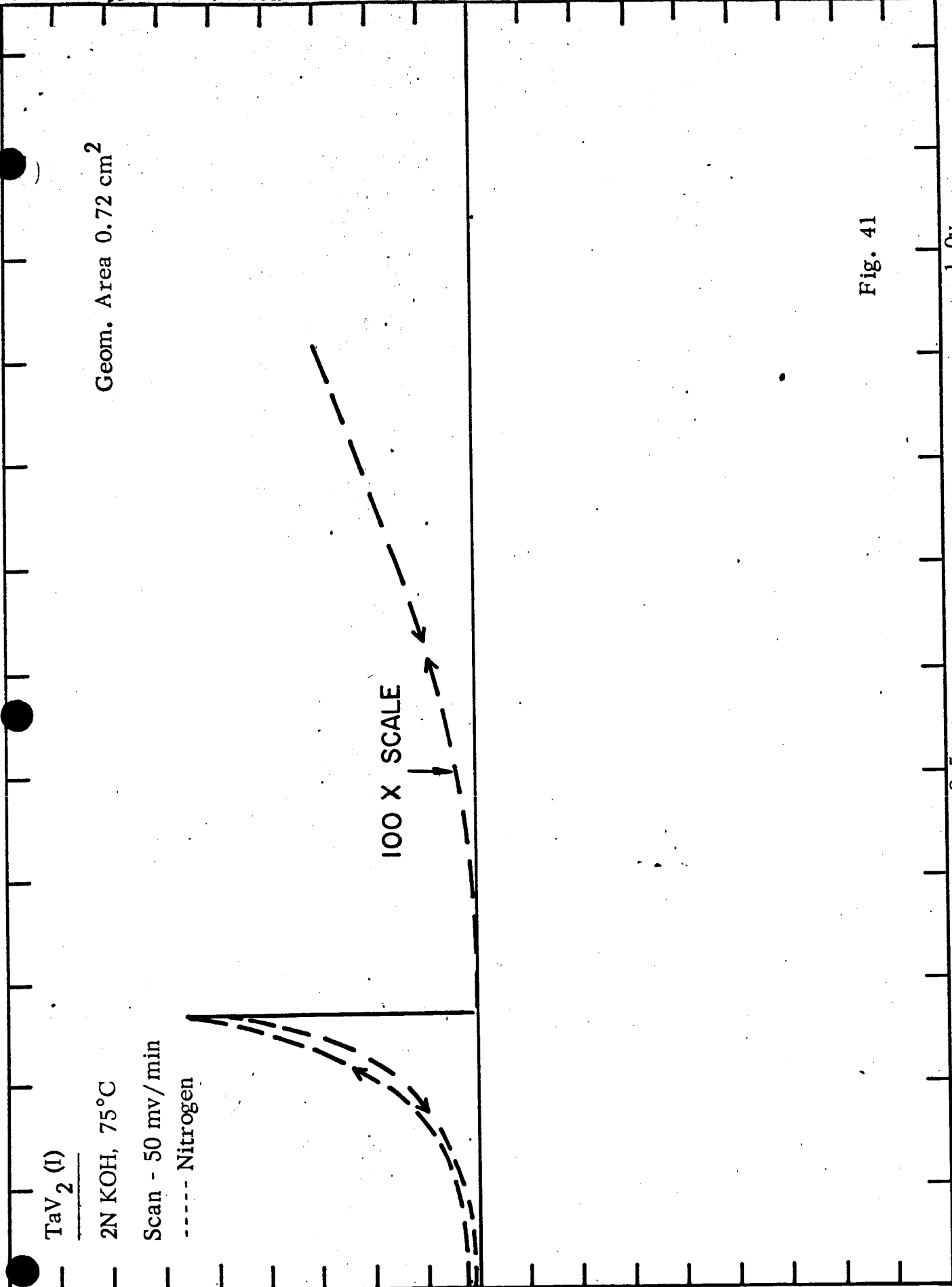
-1.0 ma
1.39 ma/cm²

Fig. 41

Potential vs. DHE

0.5v

1.0v



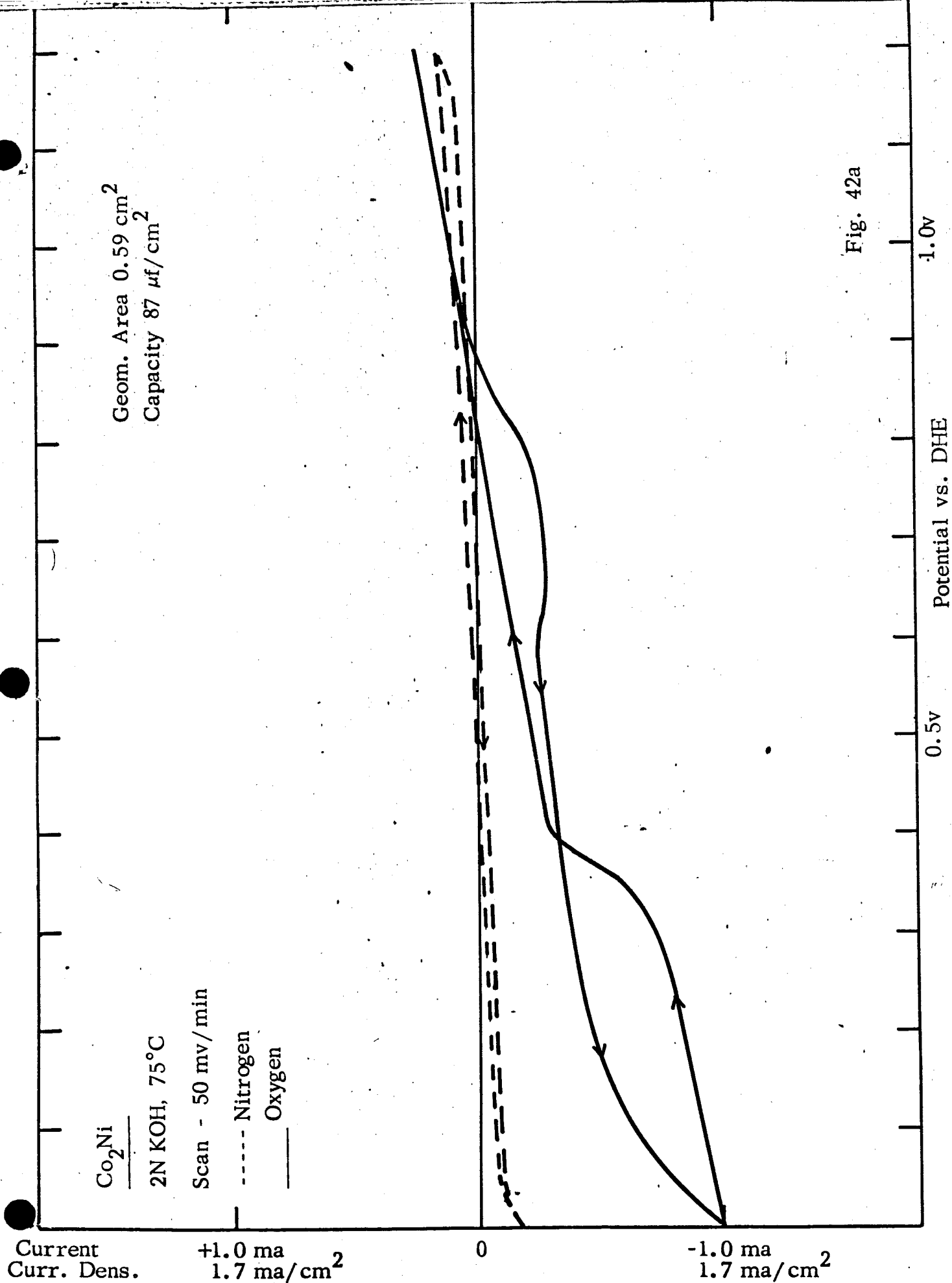


Fig. 42a

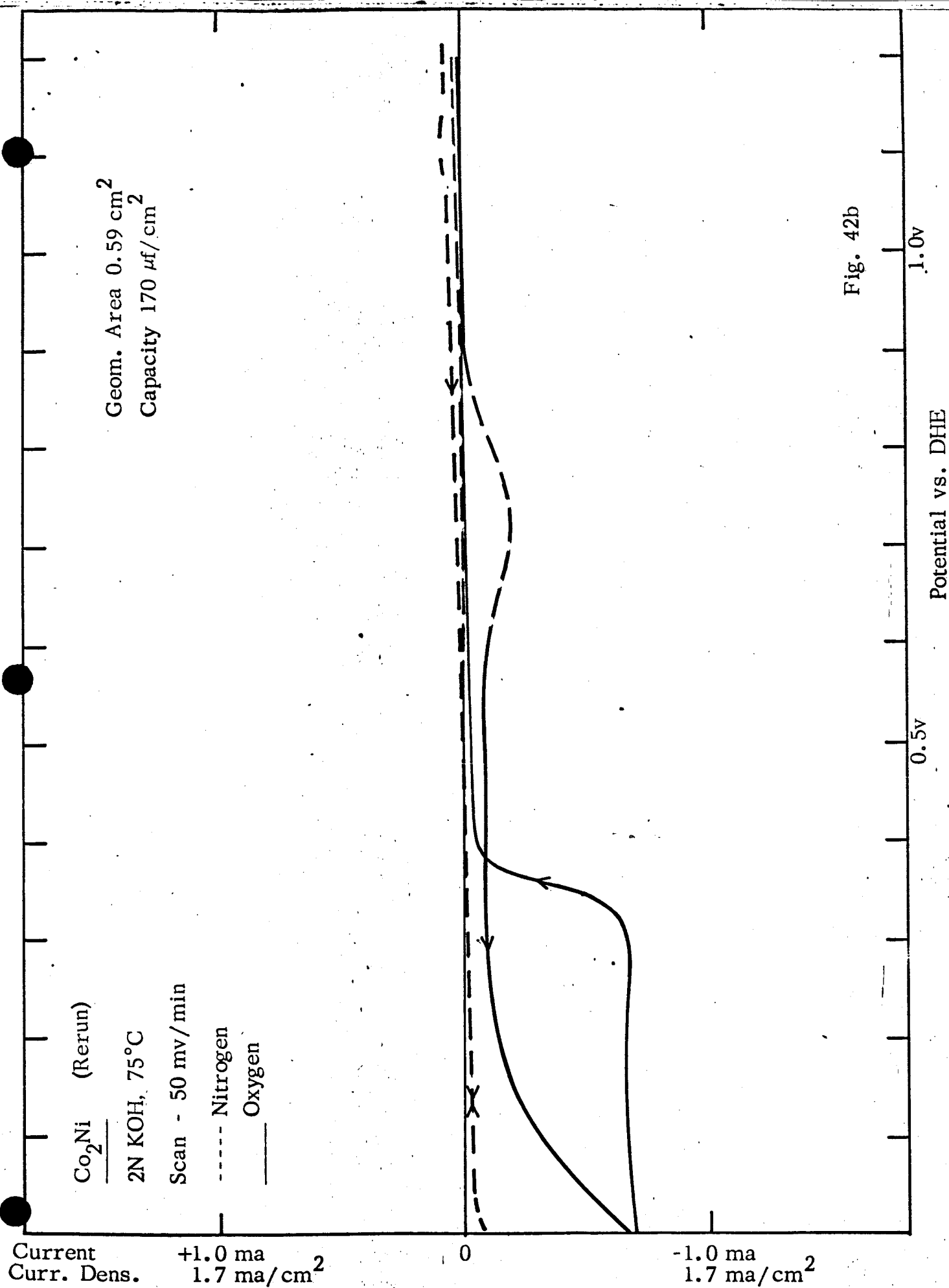


Fig. 42b

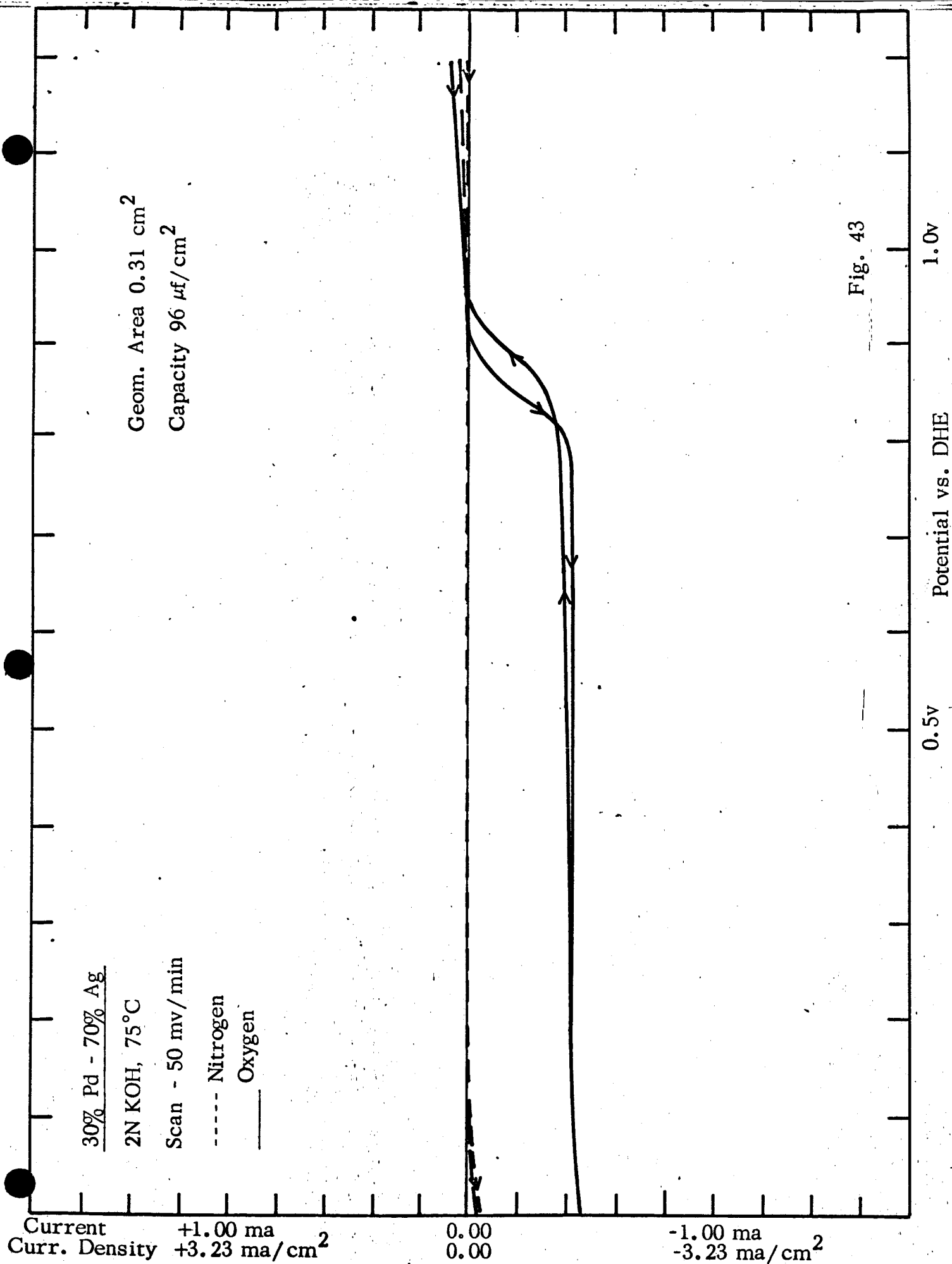


Fig. 43

Current
Curr. Dens.

+1.0 ma

1.33 ma/cm²

0

-1.0 ma

1.33 ma/cm²

50% Pd-50% Ag

2N KOH, 75°C

Scan - 50 mv/min

----- Nitrogen

— Oxygen

Geom. Area 0.75 cm²

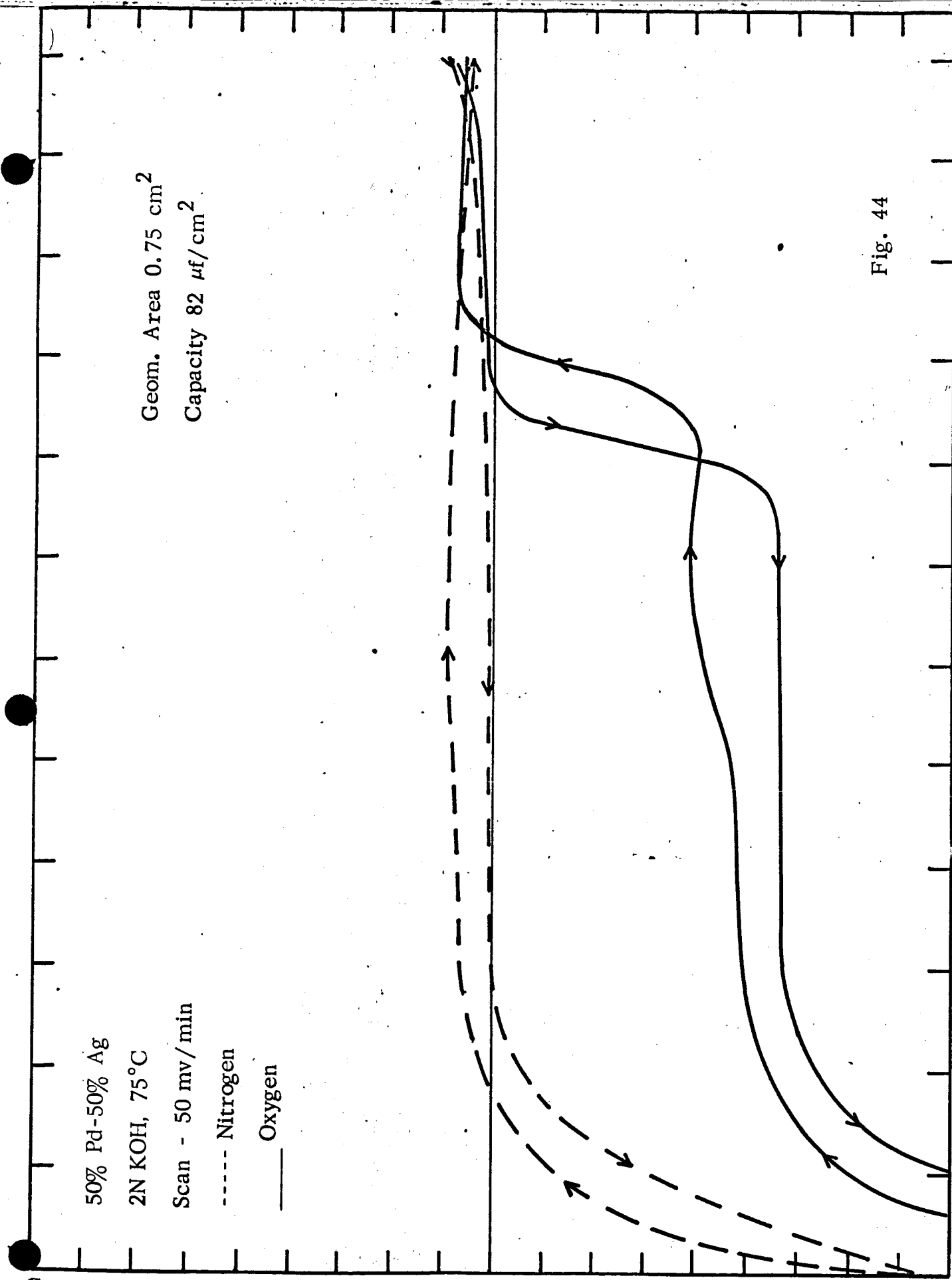
Capacity 82 μ f/cm²

Fig. 44

1.0v

Potential vs. DHE

0.5v



70% Pd - 30% Ag
 2N KOH, 75°C
 Scan 50 mv/min
 CE:Pt RE:DHE

Geometric Area .55 cm²
 Average Capacity 67 μf/cm²

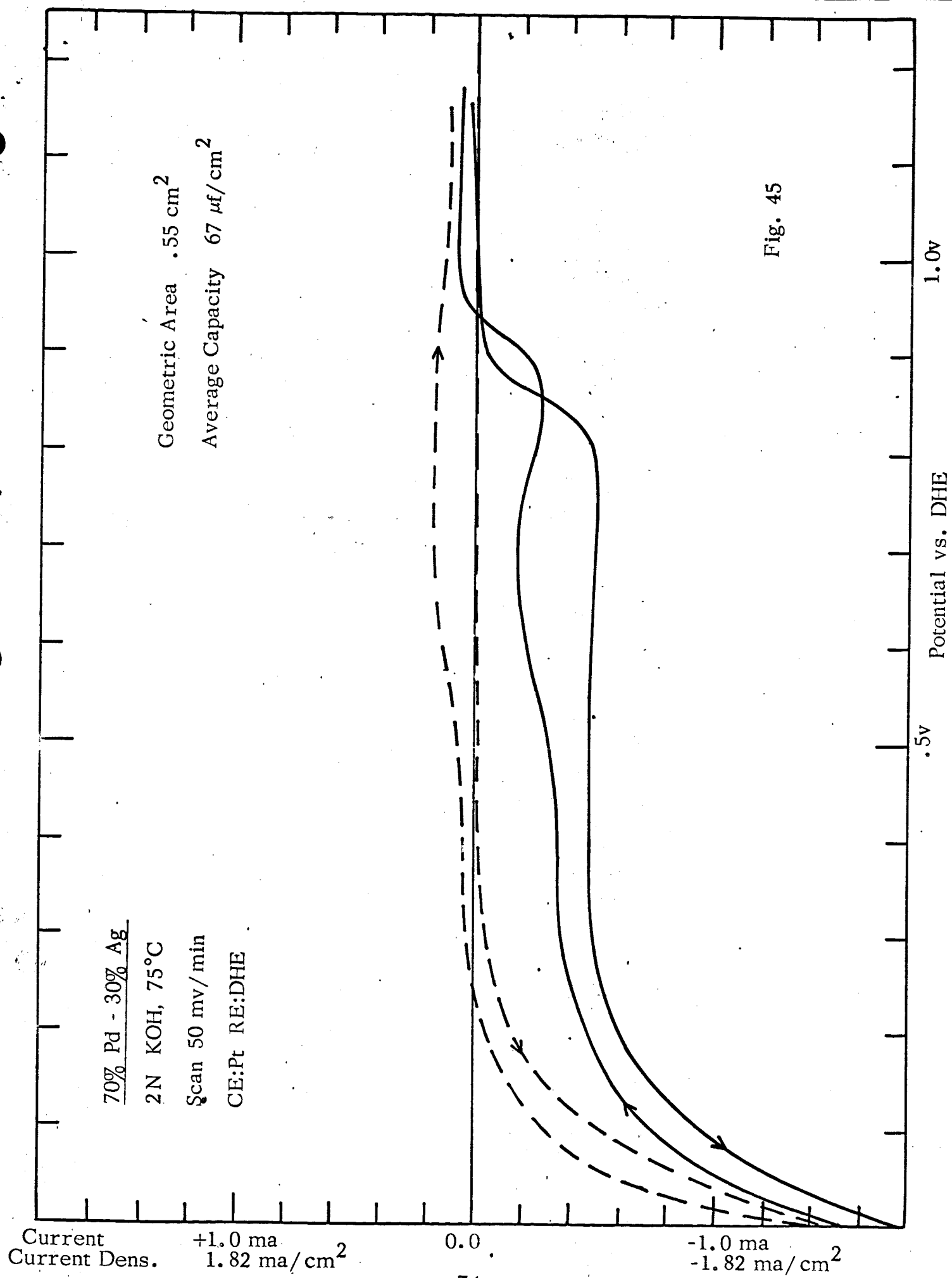


Fig. 45

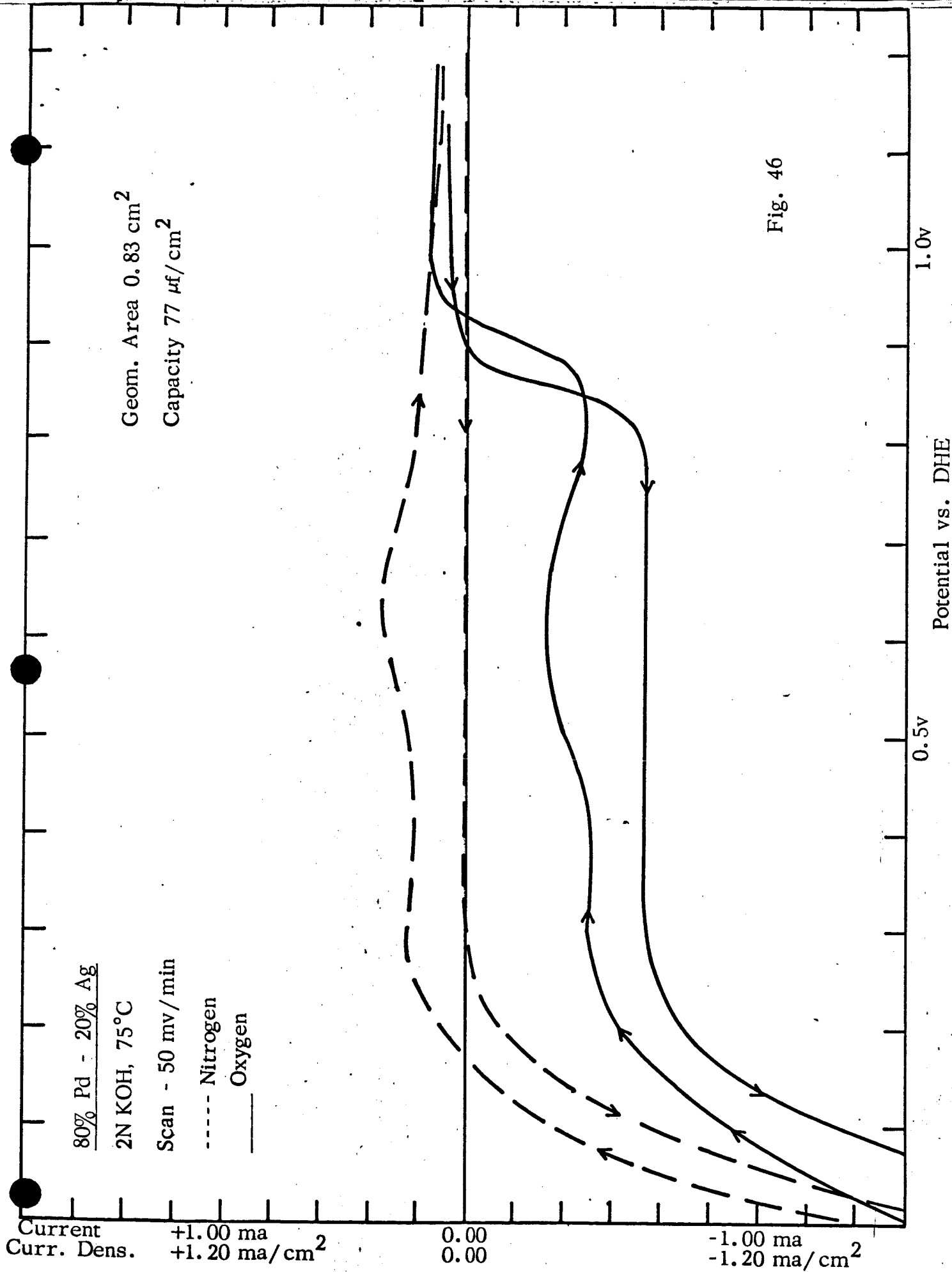
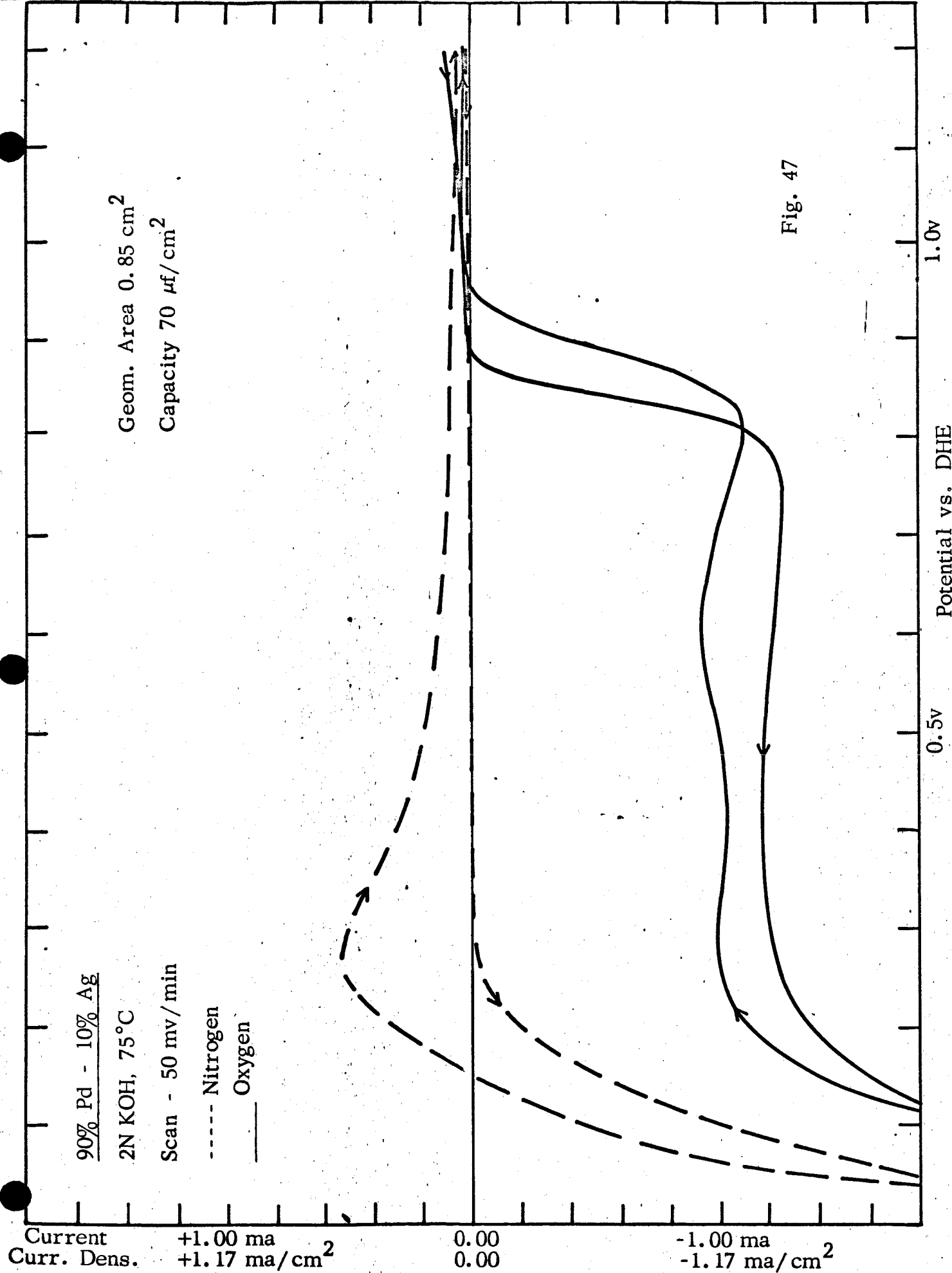


Fig. 46



Current
Curr. Dens. +1.0 ma
1.9 ma/cm²

Cr₂B

2N KOH, 75°C

Scan - 50 mv/min

----- Nitrogen

_____ Oxygen

Geom. Area 0.52 cm²
Capacity 54 μf/cm²

SCALE
X 100

0

-1.0 ma
1.92 ma/cm²

0.5v

1.0v

Potential vs. DHE

Fig. 48

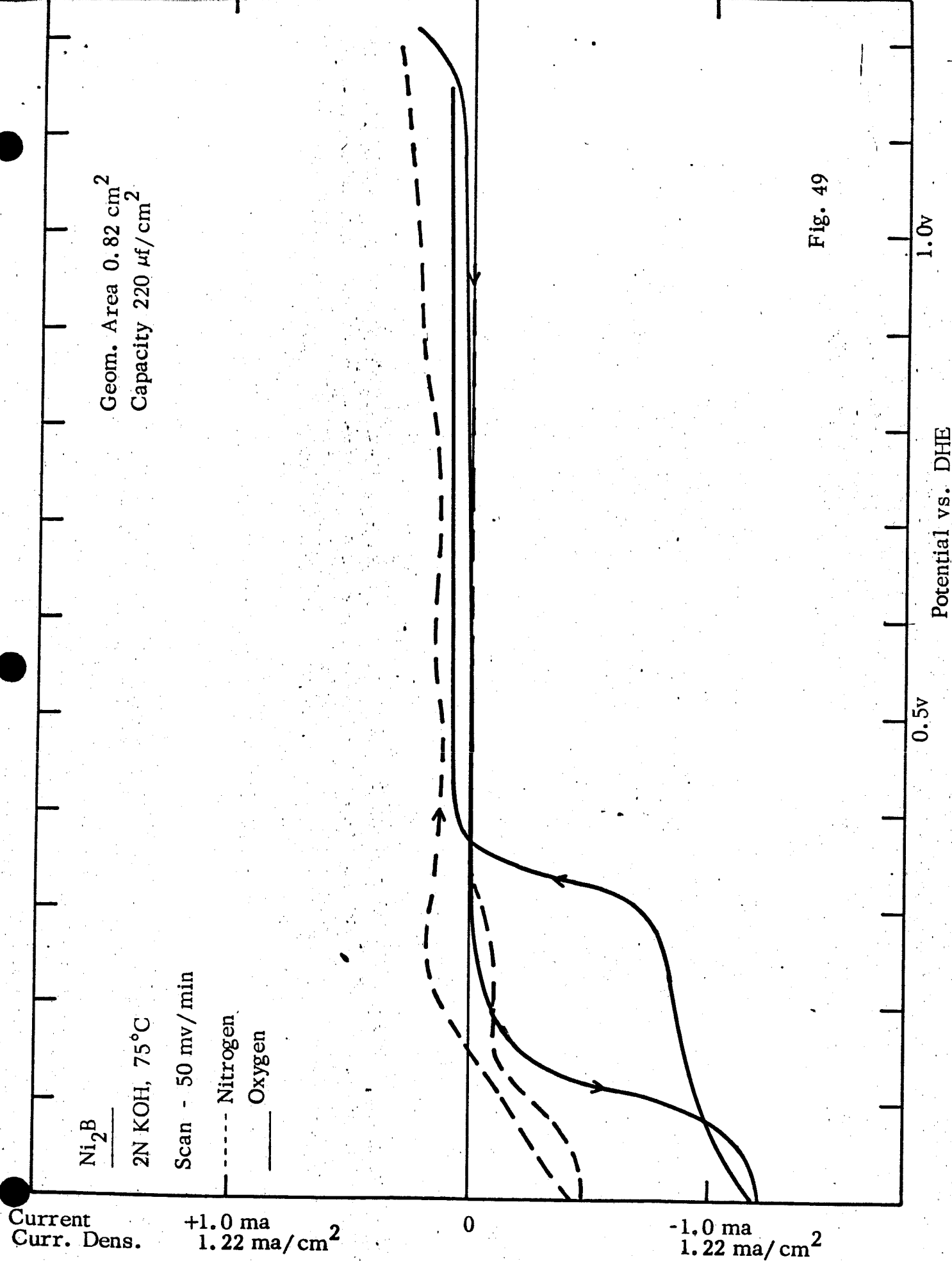


Fig. 49

Current
Current Dens. +1.0 ma
+2.84 ma/cm²

0.0

-1.0 ma
+2.84 ma/cm²

- 79 -

B₄C

2N KOH, 75°C

Scan 50 mv/min

CE:Pt RE:DHE

----- Nitrogen

_____ Oxygen

Geometric Area .35 cm²

Fig. 50

1.0v

.5v Potential vs. DHE

.5v

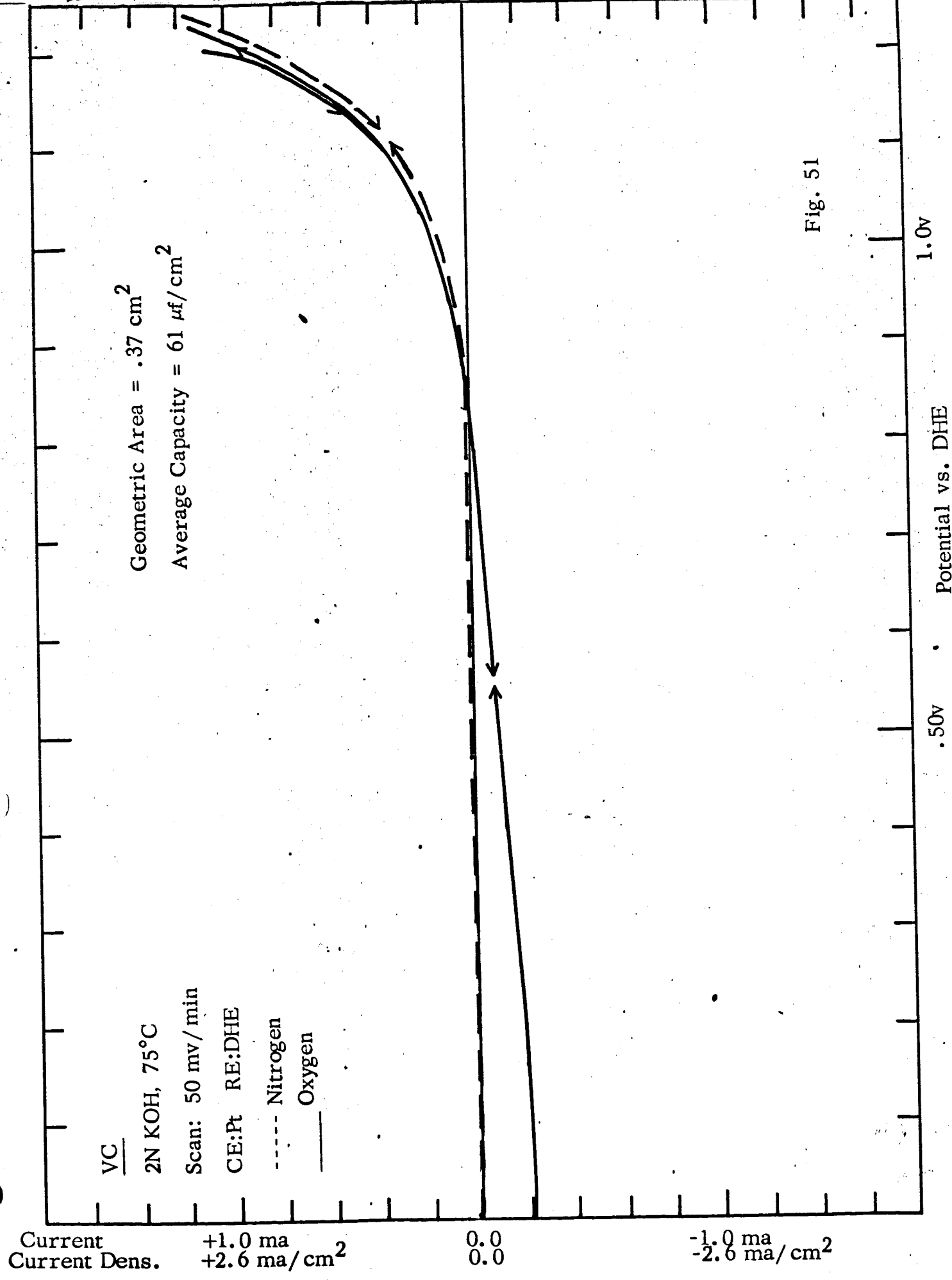


Fig. 51

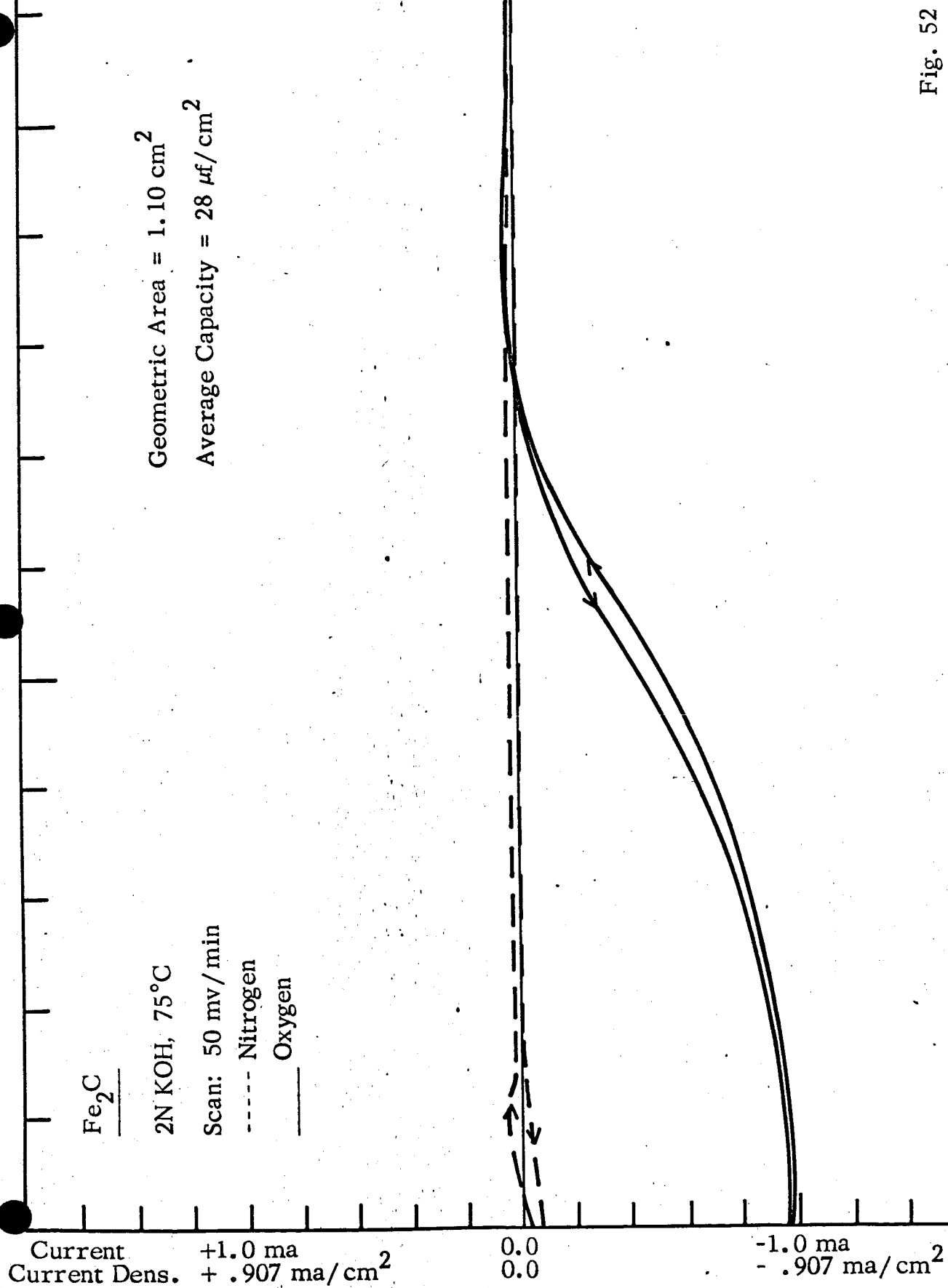
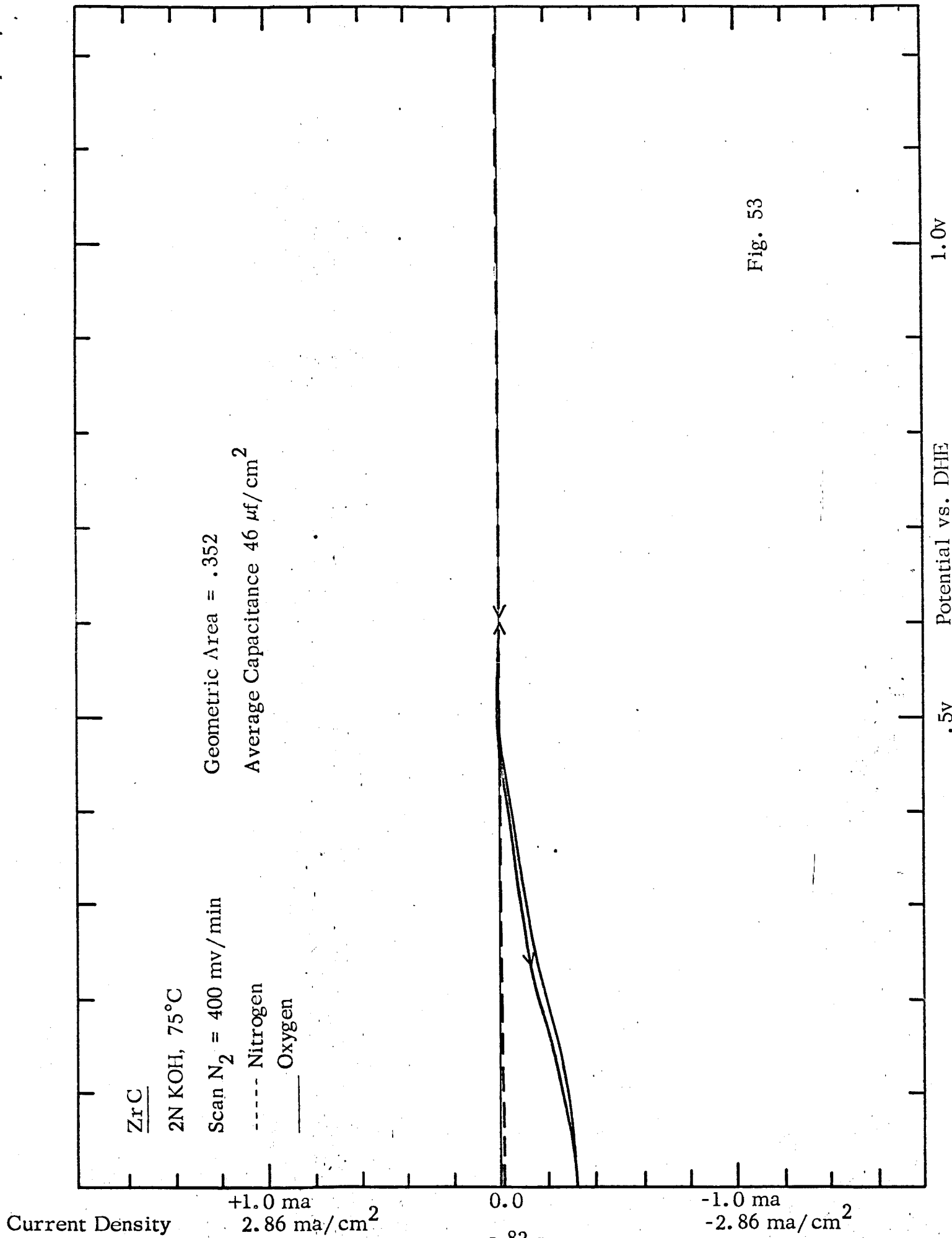


Fig. 52



Current Dens.
Current

NbC

2N KOH, 75°C

Scan: 50 mv/min

CE:Pt RE:DHE

----- Nitrogen

Average Capacitance $169 \mu\text{f}/\text{cm}^2$
Geometric Area $.35 \text{ cm}^2$

+2.84 ma/cm²
+1.0 ma

0.0
0.0

-2.84 ma/cm²
-1.0 ma

5 X
SCALE

100 X I

1 X
2 X

Fig. 54

1.0v

.5v

Potential vs. DHE

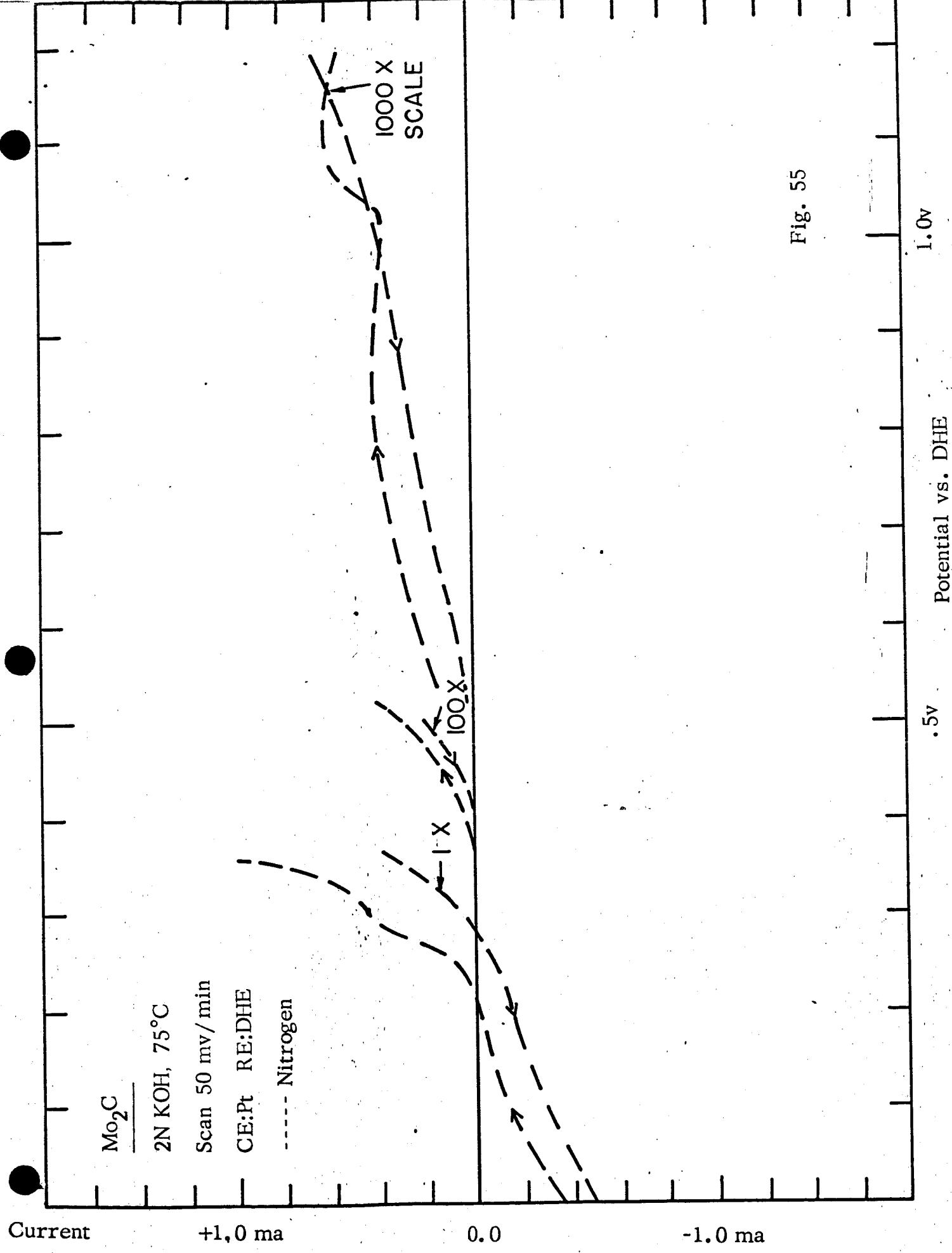


Fig. 55

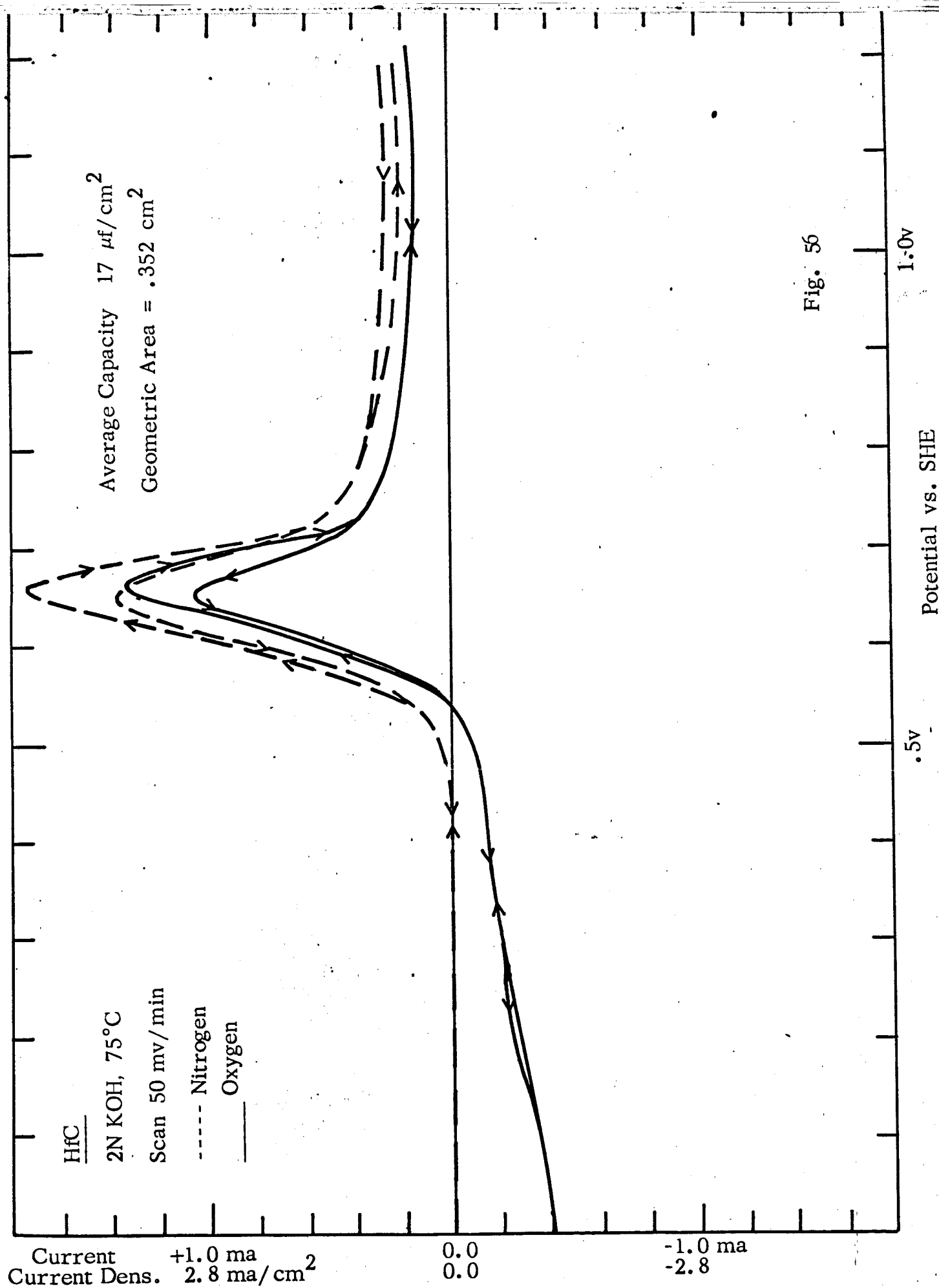


Fig. 56

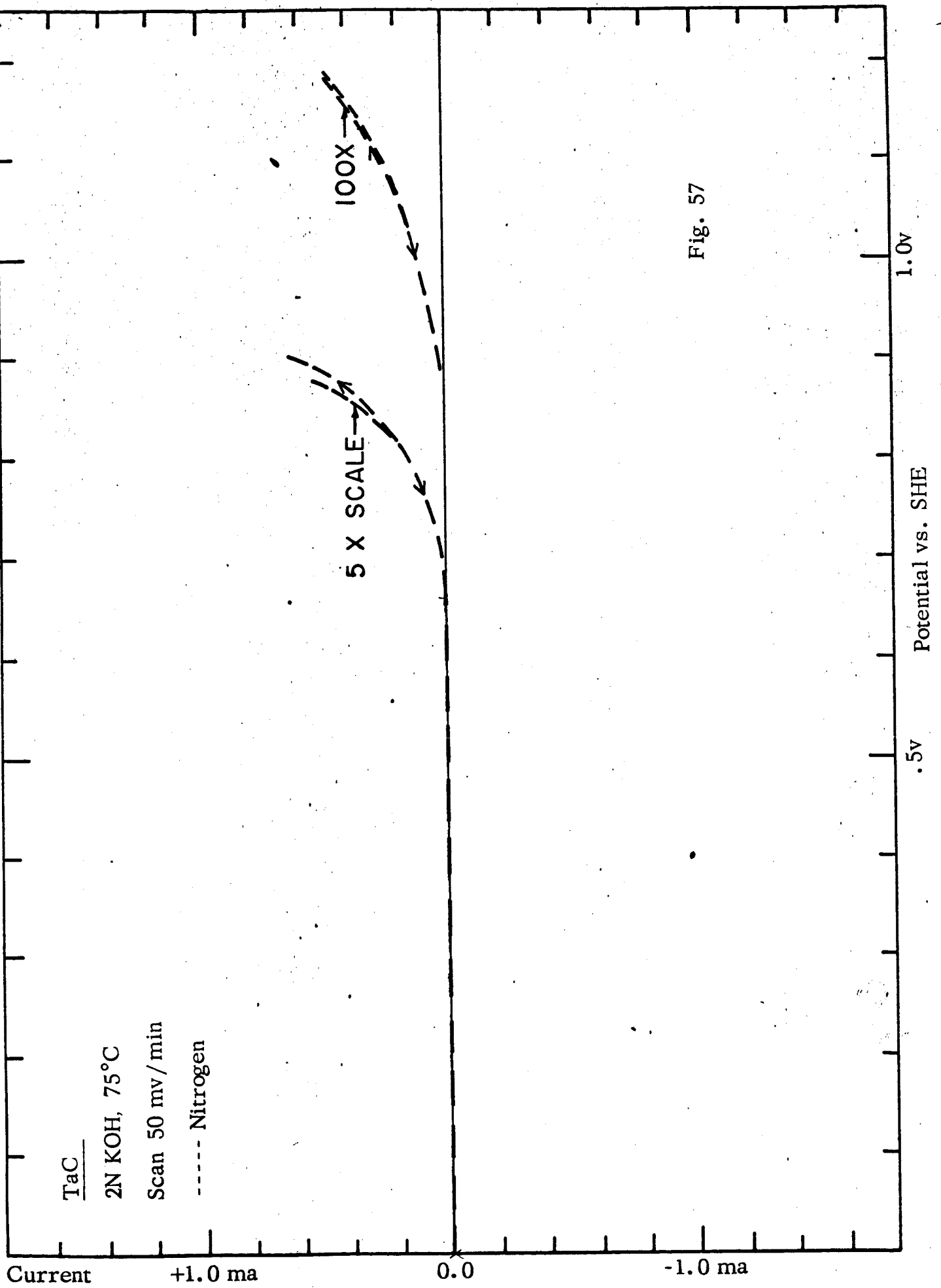
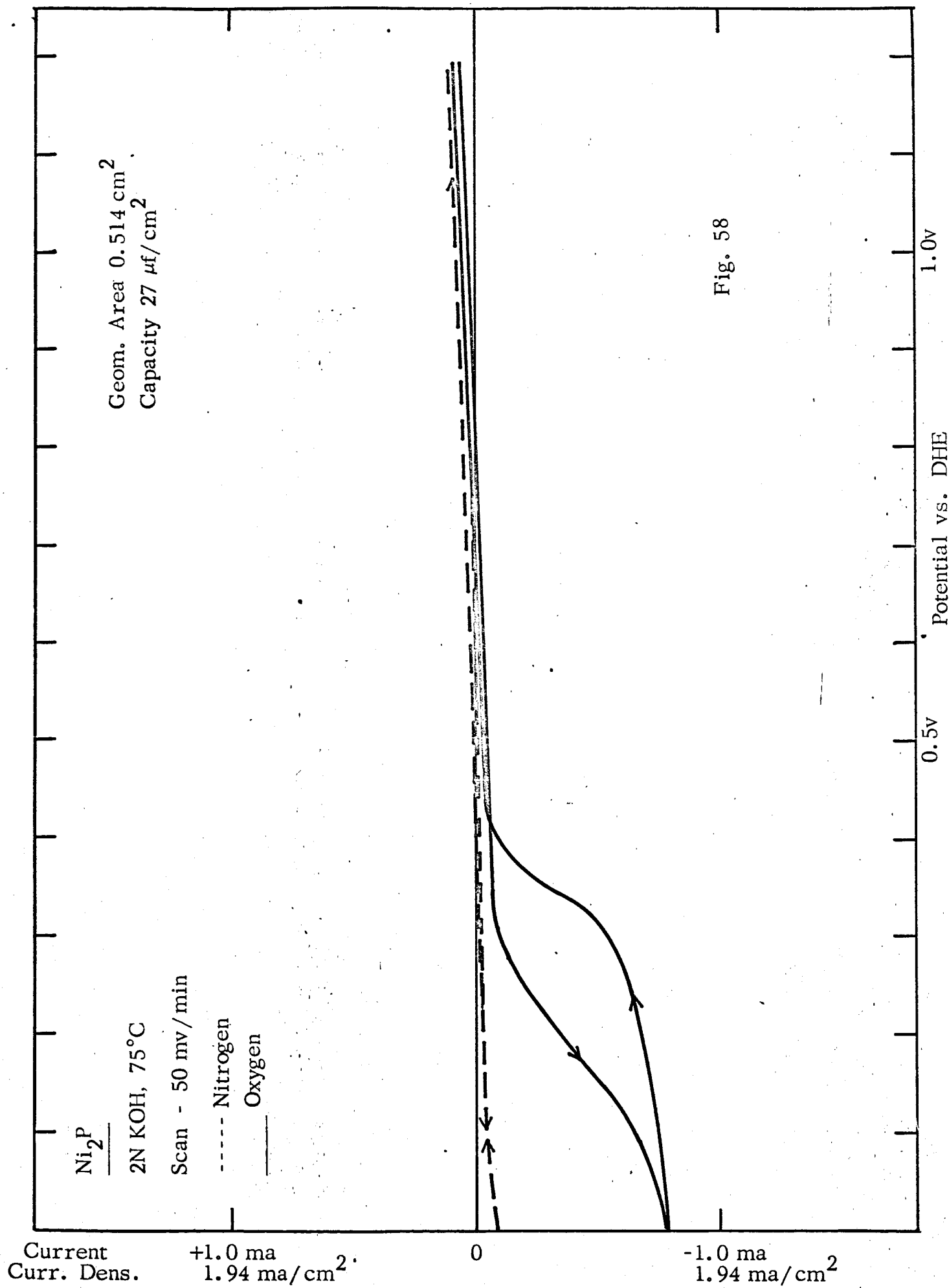
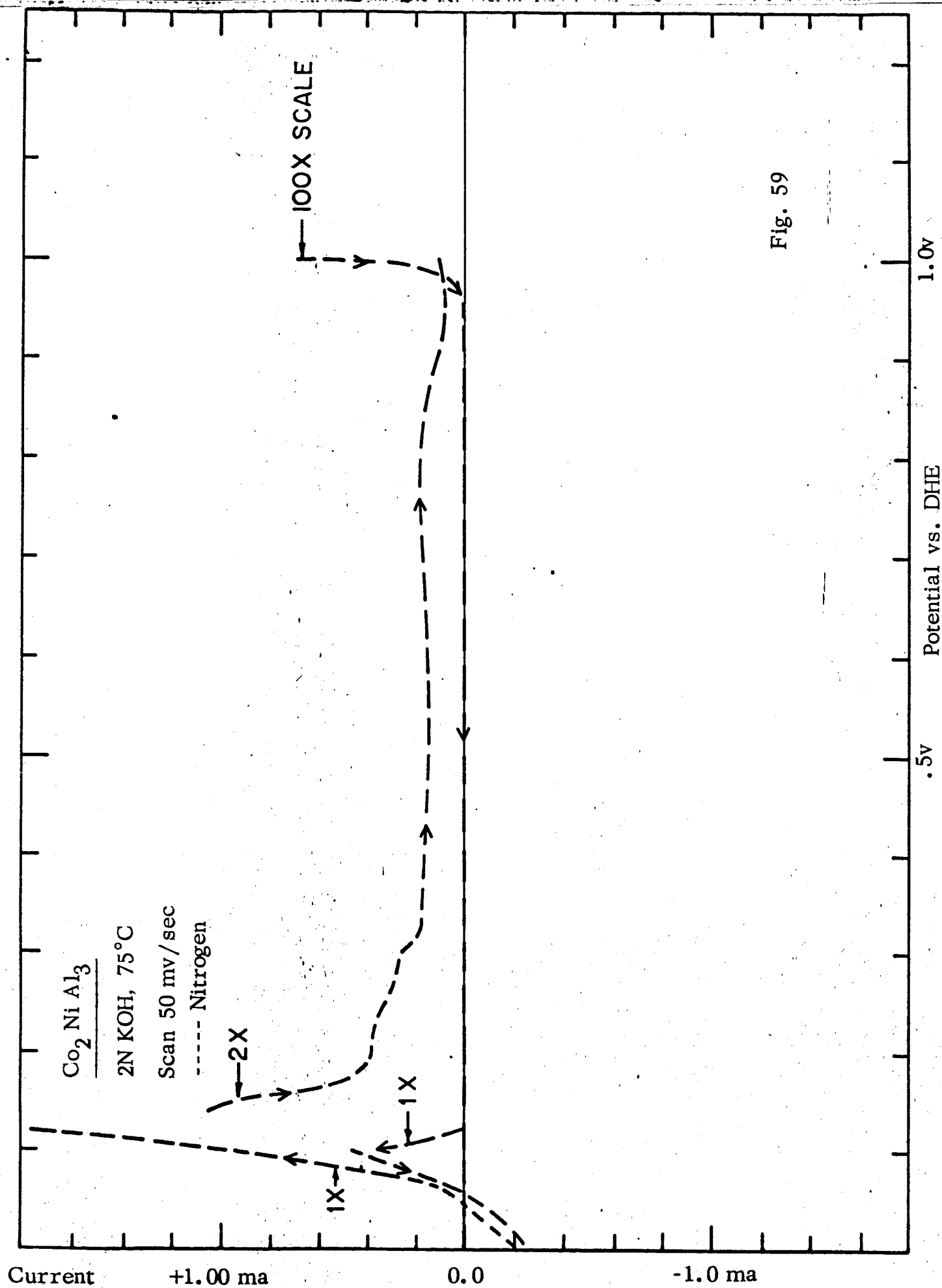


Fig. 57





F. Metallurgical Characterization of Intermetallic Compounds

The extent to which a particular electrode sample is actually made up of a given intermetallic compound can be determined by metallographic analysis. In many cases, a small amount of a second phase, either a metallic solution or an intermetallic compound, may be present in a particular sample, but the sample usually contains 90% or more of the compound to be tested.

In metallographic preparation, the sample is ground flat through a series of progressively finer SiC grit papers. It is then fine-polished on Microcloth wheels using either diamond pastes or alumina slurries, depending on the hardness of the particular compound. Next, the sample is etched to delineate the actual metallographic structure.

Due to the large number of elements involved in the synthesis of these intermetallic compounds, there is no general etchant which is applicable to all compounds. Instead, each compound must be treated separately, and a suitable etchant must be found for each case. This is generally based upon the elements in the compound, as well as the particular amount of each metal in that compound.

Representative photomicrographs of some of the intermetallic compounds studied in this program are given below. A general description of the compound, its etchant, and its heat-treatment (if any) accompanies each photomicrograph.

Of the eighteen samples shown below, only three show any significant amounts of second phase, namely Mo_3Pt , Ni_3B , and MoNi_4 . The reasons for the presence of the second phase are included with the description of the particular photomicrograph. The remainder are almost all uniformly single phase in nature. With proper melting procedure (so that there are no significant weight losses) and adequate heat treatment times and temperatures (for proper homogenization), single phase intermetallic compounds are usually attained.

AB₂ Stoichiometry (From 1st Quarterly Report)

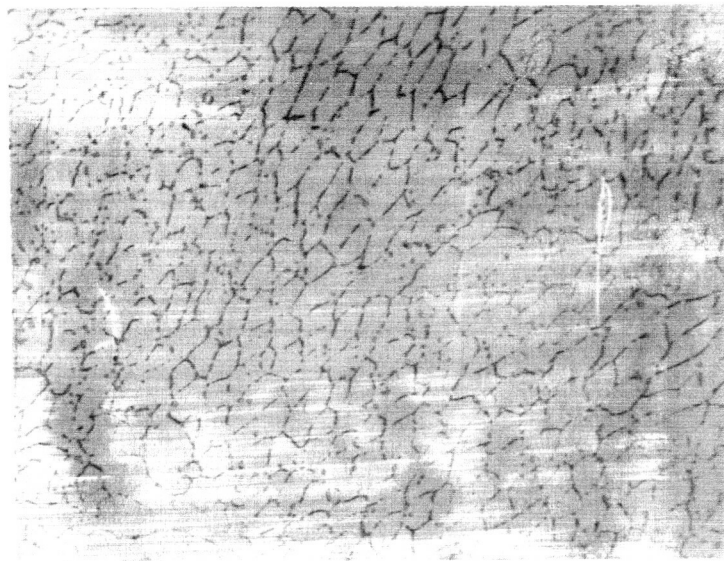


Fig. 60

Sample No. 572-25

TaPt₂ (c.p. orthorhombic phase) 150X.

Electrolytically etched in 20% HCl solution at approximately 3v (a.c. source) with Pt electrode.

The compound forms according to a congruent reaction. Due to small losses of Pt, a small amount of the compound TaPt has formed along the grain boundaries of TaPt₂.

AB₃ Stoichiometry (From 1st Quarterly Report)

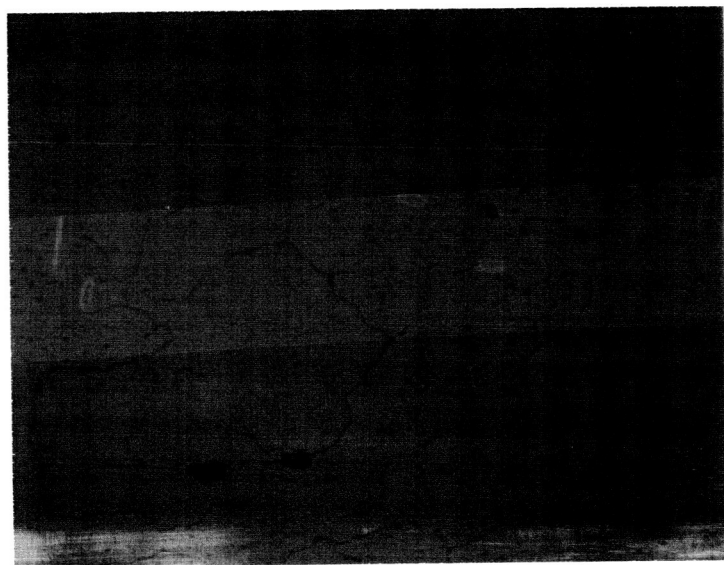


Fig. 61

Sample No. 572-31

TiPt₃ (AuCu₃ - type, L1₂ structure) 100X.

Electrolytically etched in 20% HCl solution at approximately 3v (a.c. source) with Pt electrode.

The compound forms according to a congruent reaction. Extremely small precipitate particles of TiPt are seen, possibly due to some loss of Pt during melting.

AB_3 Stoichiometry (From 1st Quarterly Report)



Fig. 62

Sample No. 572-29

$TaPt_3$ (12 lsh stacking type; DOa structure) 100X.

Electrolytically etched in a 20% HCl solution at approximately 3v (a. c. source) with Pt electrode.

This compound forms according to a congruent reaction, and is entirely $TaPt_3$.

AB_3 Stoichiometry (From 1st Quarterly Report)



Fig. 63

Sample No. 572-17

$NbNi_3$ ($TiCu_3$ - type, orthorhombic structure) 50X.

This photomicrograph was taken under polarized light, as chemical etching seemed ineffective.

This compound forms according to a congruent reaction, and is entirely $NbNi_3$.

AB₃ Stoichiometry (From 1st Quarterly Report)



Fig. 64

Sample No. 572-21

TiNi₃ (DO₂₄ structure) 75X.

Chemically etched in 15 parts HCl, 5 parts HF, 5 parts HNO₃, and 15 parts glycerol. Photomicrograph taken under polarized light.

This compound formed according to a congruent reaction. The sample is almost entirely TiNi₃, except for minute particles of TiNi, or the Ni solid solution phase.

Interstitials (From 1st Quarterly Report)

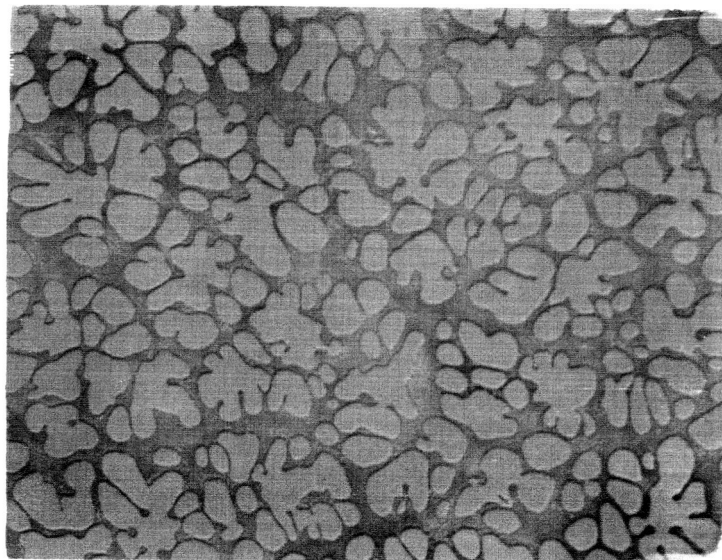


Fig. 65

Sample No. 572-30

Ni_3B (DO_{11} structure) 250X.

Chemically etched in 50 parts HCl, 5 parts HCl, and 25 parts H_2O .

During arc-melting, large losses of boron were noted. The resultant sample is therefore a two-phase alloy, consisting of primary dendrites of Ni_3B , plus a eutectic mixture of Ni_3B and Ni solid solution.

A_3B Stoichiometry

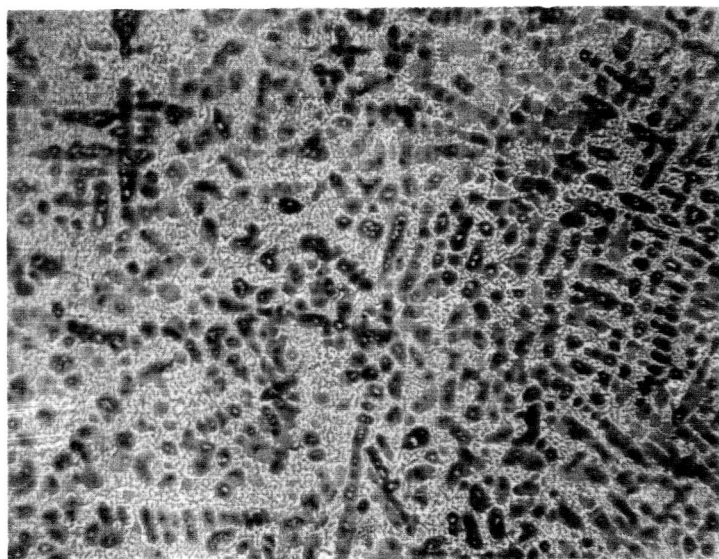


Fig. 66

Sample No. 572-55

Mo_3Pt (β - W type, A15 structure) 85X.

Chemically etched in 5 grams $CuSO_4$, 10 cc NH_4OH , 20 cc H_2O .

The β -W-type compound, based on Mo_3Pt , actually forms peritectically at $1650^\circ C$ at approximately 16 atomic % Pt. This particular sample was made at a composition of 25 atomic % Pt, and heat-treated in vacuum at $1600^\circ C$ for 40 hours. The actual sample consists of primary grains of the β -W phase (Mo-16 atomic % Pt), plus a mixture of the β -W and the epsilon ($MoPt$) phases.

A_2B Stoichiometry



Fig. 67

Sample No. 572-62

Ti₂Cu ($MoSi_2$ - type, C11 b structure) 75X.

Chemically etched in 5 parts HNO₃, 5 parts HF, 40 parts H₂O.

Ti₂Cu forms peritectically at 990°C. This sample was heat-treated in an evacuated quartz cylinder (10^{-5} mm Hg) at 800°C for 160 hours; it is virtually all Ti₂Cu.

AB Stoichiometry

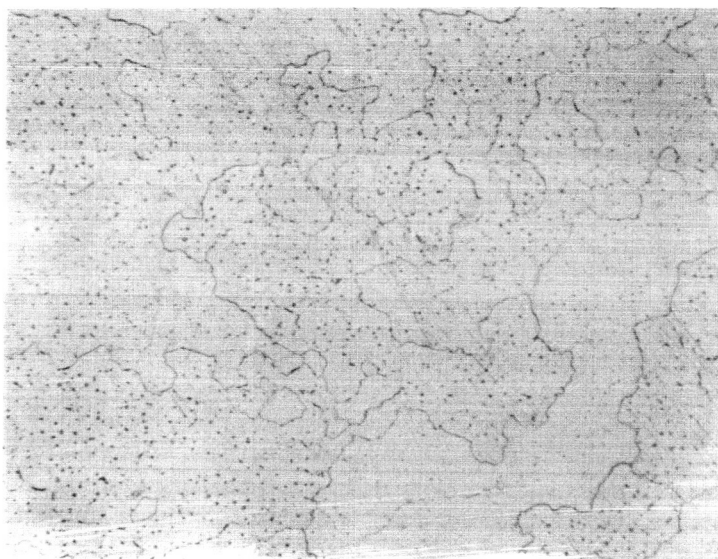


Fig. 68

Sample No. 572-61

TiCo (CsCl type; Be structure) 100X.

Chemically etched in 10 parts HNO_3 , 10 parts HF, 10 parts glycerin, and 1 part H_2O .

The reaction according to which TiCo forms is not definitely known. This sample was heat-treated at 800°C for 160 hours in an evacuated quartz cylinder (10^{-5} mm Hg). The small particles of second phase precipitate may be Ti_2Co , due to a small weight loss of CO during arc-melting.

AB Stoichiometry

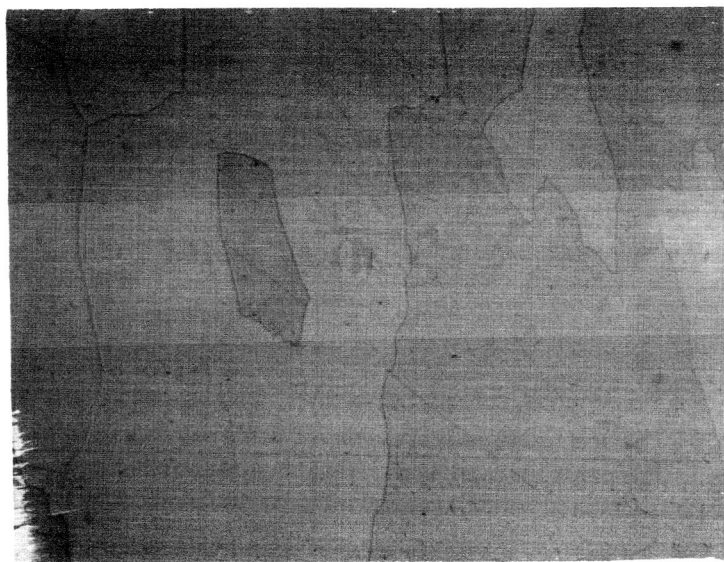


Fig. 69

Sample No. 572-59

NiAl (CsCl type, B2 structure) 50X.

Chemically etched in 25 parts HCl, 5 parts HNO₃, and 10 parts H₂O.

The compound forms according to a congruent reaction. The sample is entirely NiAl.

AB Stoichiometry

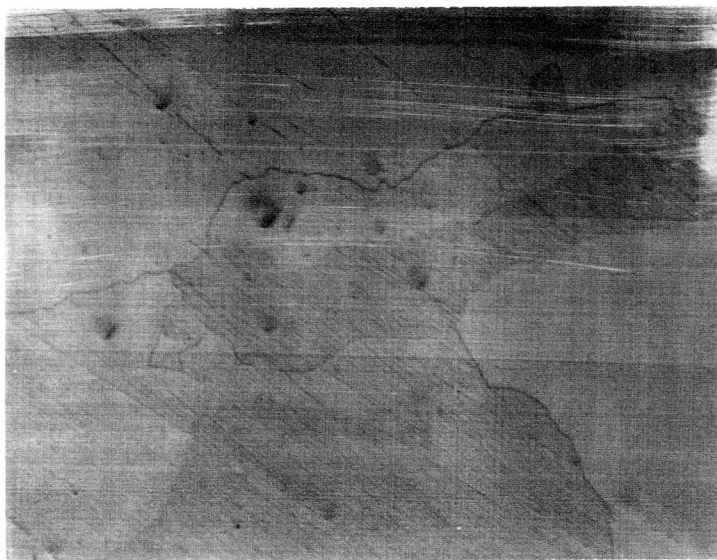


Fig. 70

Sample No. 572-73

CoAl (CoAl type, B2 structure) 75X.

Chemically etched with 25 parts HCl, 10 parts H₂O,
5 parts HNO₃, 1 part HAc.

The compound is formed according to a congruent reaction.
The sample is entirely CoAl.

AB Stoichiometry

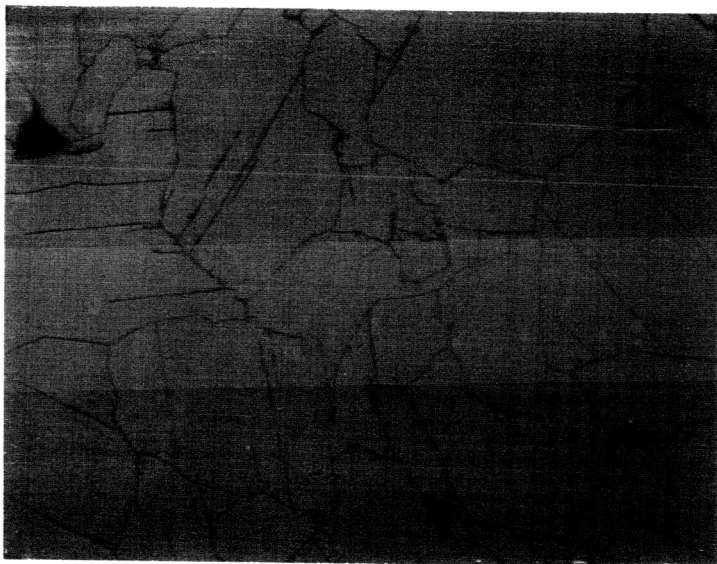


Fig. 71

Sample No. 572-38

MoPt (Hexagonal close-packed structure) 100X.

Electrolytically etched in 20% HCl solution at approximately 3v (a.c. source) with Pt electrode.

The compound forms according to a congruent reaction. The sample is entirely MoPt.

AB₃ Stoichiometry



Fig. 72

Sample No. 572-48

CoPt₃ (AuCu₃ type, L1₂ structure) 50X.

Electrolytically etched in 20% HCl solution at approximately 3v (a.c. source) with Pt electrode.

This compound forms according to an ordering reaction at 750°C from the Co-Pt solid solution of this composition. After melting, the sample was heat-treated at 700°C, 66 hours, in an evacuated quartz cylinder (10⁻⁵ mm Hg). The sample is entirely CoPt₃.

ABn, $n > 3$ Stoichiometry

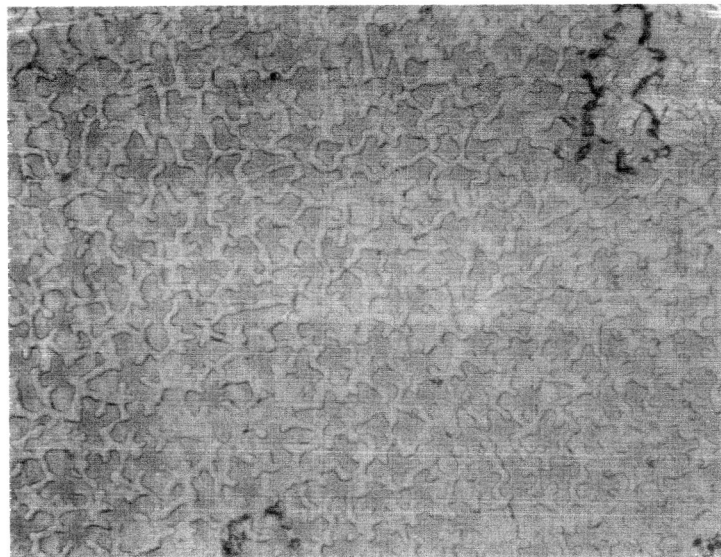


Fig. 73

Sample No. 572-49

MoNi₄ (Face-centered tetragonal superstructure) 200X.

Chemically etched.

The compound forms according to a peritectoid reaction at 840°C. The melted sample was heat-treated in an evacuated quartz cylinder (10^{-5} mm Hg) at 700°C for 66 hours. The heat-treatment was insufficient to transform the as-melted material entirely to the actual compound, and the sample is most likely a mixture of MoNi₄ and Mo solid solution.

Solid Solutions

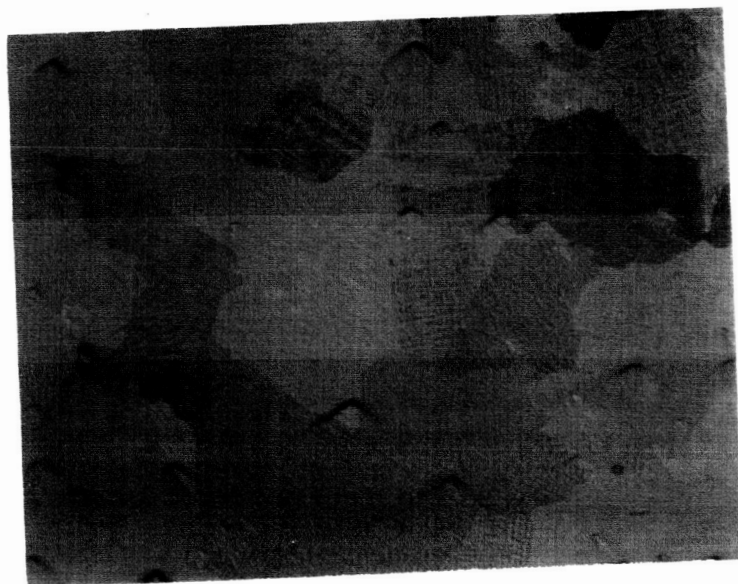


Fig. 74

Sample No. 572-44

Ta - 66.7 atomic % V (TaV_2) 50 X

Chemically etched with 10 parts HF, 10 parts HNO_3 , 20 parts glycerin.

At elevated temperatures, Ta and V form a complete series of solid solution alloys. At the composition TaV_2 , the alloy orders below 1320°C to form a compound with a Laves phase (MgCu_2 -type) structure. The above photomicrograph shows that particular composition in its solid solution state.

Solid Solution

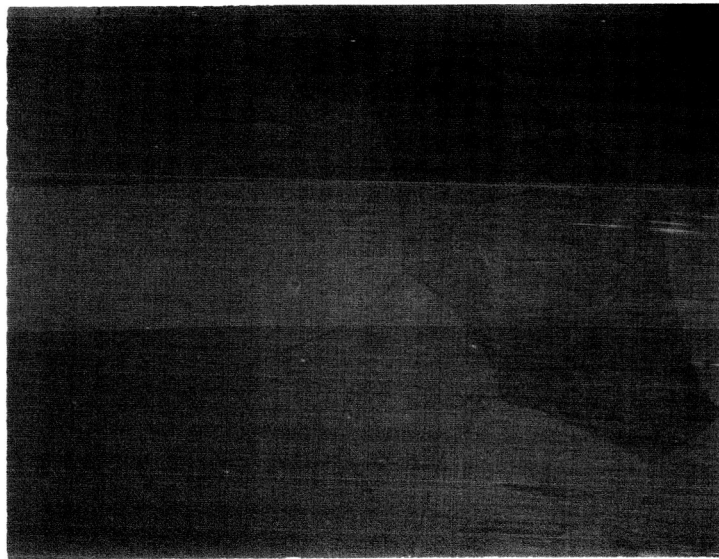


Fig. 75

Sample No. 572-33

Co - 33.3 atomic % Ni (Co_2Ni) 50X.

Chemically etched.

Co and Ni form a complete series of solid solution alloys.
This sample is an alloy corresponding to the composition
66.7 atomic % Co, 33.3 atomic % Ni.

Interstitials

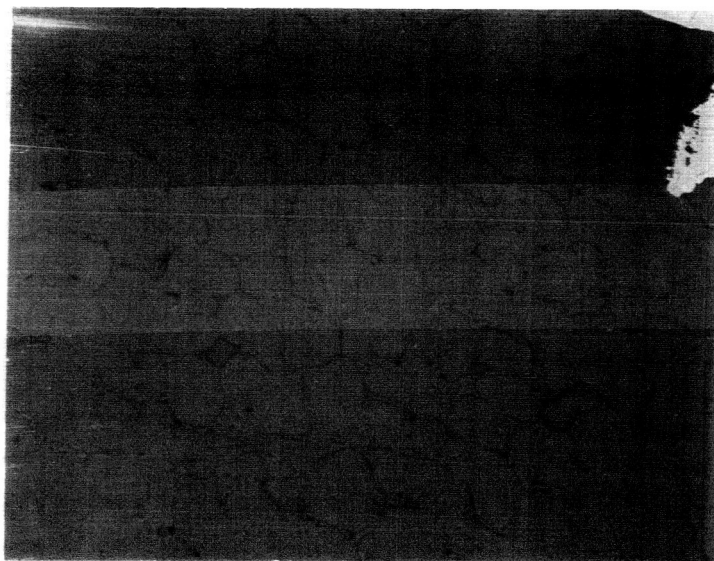


Fig. 76

Sample No. 572-39

Ni_2B (CuAl_2 type, C16 structure) 100X.

Chemically etched with 50 parts HCl , 5 parts HNO_3 ,
25 parts H_2O .

The compound is formed according to a congruent reaction.
The sample is primarily Ni_2B with some small amounts of
 Ni_3B at the grain boundaries due to boron loss during melting.

Ternary compound
AB Stoichiometry

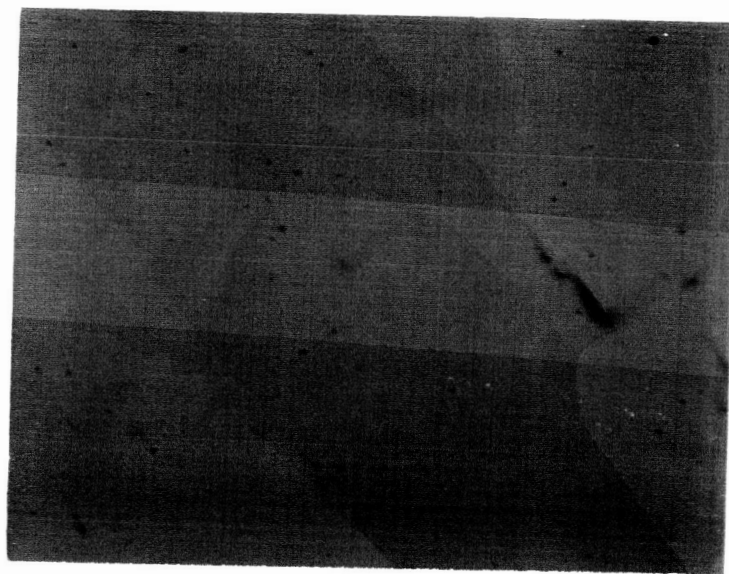


Fig. 77

Sample No. 572-72

$(\text{Co}_{.67}\text{Ni}_{.33})\text{Al}$ (CsCl type, B2 structure) 75X.

Chemically etched with 5 parts HNO_3 , 25 parts HCl , 1 parts HAc , 10 parts H_2O .

This compound is based upon CoAl and NiAl which are mutually soluble in one another, i. e., Co and Ni can readily substitute for one another. No second phase was present in the sample.

V. GENERAL DISCUSSION

A detailed discussion has accompanied each test. Of the tested elements, Pd shows very good O_2 activity, only slightly inferior to Pt (around 75 mv more polarization in the non-steady state $i(E)$ -curve). Graphite shows relatively good intrinsic activity (with O_2 current at $E = 800$ mv); and iron with O_2 -reduction at $E = 600$ mv is surprisingly more active than nickel.

The experiments with the intermetallic compounds show that under conditions of O_2 -reduction, the fundamental factor determining the activity is the atomic factor. Thus, compounds of Pt and Au show an $i(E)$ -curve for O_2 -reduction which is similar (but with "diluted" activity) to those of pure Pt and Au. In some cases such as $TaPt_2$, the activity of the intermetallic compound is very close to the activity of pure Pt.

The solid solution, " Co_2Ni " shows a very interesting behavior which confirms the catalytic activity of Co^{3+} containing oxide and the poor activity of the bivalent oxide.

Of the interstitials tested, carbides show activity, especially an iron carbide (Hag carbide Fe_2C) prepared by surface carburization (with CO) of an iron rod at several temperatures not exceeding $300^\circ C$, which shows activity for O_2 -reduction which, lower than that of Pt, Pd, Ag and Au, but considerably better than the activity of Fe.

VI. FUTURE WORK

1. Preparation and testing of carbides, nitrides, and carbonitrides of Fe, Co, Ni both as high dispersed material and as compact materials (surface layers on pure metals).
2. Testing as "floating electrodes" Pt-Teflon-electrodes (as standards) and electrodes obtained from highly dispersed catalysts (carbides, carbonitrides, etc.; Pd-Au- "blacks", etc.).
3. Testing of compact samples of borides, silicides, and nitrides obtained from Cerac.
4. Testing of compact samples of Pt-Au (ten compositions); Pd-Au (ten compositions); and Ag-Au (ten compositions).
5. Testing of compact oxides. (NiO doped with Li) $\text{NiO Co}_2\text{O}_3$, Fe_3O_4 .

DISTRIBUTION LIST FOR FUEL CELL REPORTS

August, 1964

National Aeronautics & Space Administration
Washington, D.C. 20546

Attn: Ernst M. Cohn, Code RNW
George F. Esenwein, Code MAT
A. M. Andrus, Code ST
J. R. Miles, Code SL

National Aeronautics & Space Administration
Scientific and Technical Information Facility
P. O. Box 5700
Bethesda, Maryland, 20014

(3)

National Aeronautics & Space Administration
Goddard Space Flight Center
Greenbelt, Maryland
Attn: Thomas Hennigan

National Aeronautics & Space Administration
Langley Research Center
Langley Station
Hampton, Virginia
Attn: S. T. Peterson

National Aeronautics & Space Administration
Lewis Research Center
21000 Brookpark Road
Cleveland 35, Ohio
Attn: N. D. Sanders
Robert Miller
Robert L. Cummings

National Aeronautics & Space Administration
Marshall Space Flight Center
Huntsville, Alabama
Attn: Philip Youngblood

Cell Reports (cont' t.)

National Aeronautics & Space Administration
Ames Research Center
Pioneer Project
Moffett Field, California
Attn: James R. Swain

National Aeronautics & Space Administration
Manned Spacecraft Center
Houston 1, Texas
Attn: William R. Dusenbury
Robert Cohen

National Aeronautics & Space Administration
Ames Research Center
Mountain View, California
Attn: Jon Rubenzer, Biosatellite Project

Jet Propulsion Laboratory
4800 Oak Grove Drive
Pasadena, California
Attn: Aiji Uchiyama

DEPARTMENT OF THE ARMY

U. S. Army Engineer R & D Labs.
Fort Belvoir, Virginia
Attn: Electrical Power Branch

U. S. Army Engineer R & D Labs.
Fort Monmouth, New Jersey
Attn: Arthur F. Daniel (Code SELRA/SL-PS)

U. S. Army R & D Liaison Group (9851 DV)
APO 757
New York, New York
Attn: Chief, Chemistry Branch

U. S. Army Research Office
Physical Sciences Division
3045 Columbia Pike
Arlington, Virginia.

Cell Reports (cont.)

AF Cambridge Research Lab

Attn: CRZE

L. G. Hanscom Field
Bedford, Massachusetts .

Attn: Francis X. Doherty/Edward Raskind (Wing F)

Rome Air Development Center, ESD
Griffiss AFB, New York

Attn: Frank J. Mollura (RASSM)

Space Systems Division

Attn: SSZAE-11

Air Force Unit Post Office
Los Angeles 45, California

Air Force Ballistic Missile Division

Attn: WEZYA-21

Air Force Unit Post Office
Los Angeles 45, California

ATOMIC ENERGY COMMISSION

Mr. Donald B. Hoatson

Army Reactors, DRD

U. S. Atomic Energy Commission
Washington 25, D. C.

OTHER GOVERNMENT AGENCIES

Defense Documentation Center Headquarters

Cameron Station, Bldg. 5

5010 Duke Street

Alexandria 4, Virginia

Attn: TISIA

Office, DDR & E: USW & BSS

The Pentagon

Washington 25, D. C.

Attn: G. B. Wareham .

Cell Reports (cont.)

Harry Diamond Labs.
Room 300, Building 92
Connecticut Avenue & Van Ness Street, N. W.
Washington, D. C.

Attn: Nathan Kaplan

Army Materiel Command
Research Division
AMCRD-RSCM T-7
Washington 25, D. C.

Attn: John W. Crellin

Natick Labs.
Clothing & Organic Materials Div.
Natick, Massachusetts

Attn: Leo A. Spano/Robert N. Walsh

U. S. Army TRECOM
Physical Sciences Group
Fort Eustis, Virginia

Attn: (SMOFE)

U. S. Army Research Office
Box CM, Duke Station
Durham, North Carolina

Attn: Paul Greer/Dr. Wilhelm Jorgensen

U. S. Army Mobility Command
Research Division
Center Line, Michigan

Attn: O. Renius (AMSMO-RR)

Hq., U. S. Army Materiel Command
Development Division
Washington 25, D. C.

Attn: Marshall D. Aiken (AMCRD-DE-MO-P)

Cell Reports (cont.)

DEPARTMENT OF THE NAVY

Office of Naval Research
Department of the Navy
Washington 25, D.C.

Attn: Dr. Ralph Roberts/H. W. Fox

Bureau of Naval Weapons
Department of the Navy
Washington 25, D.C.

Attn: (Code RAAE)

U. S. Naval Research Laboratory
Washington, D. C. 20390

Attn: (Code 6160)

Bureau of Ships
Department of the Navy
Washington 25, D.C.

Attn: Bernard B. Rosenbaum/C. F. Viglotti

Naval Ordnance Laboratory
Department of the Navy
Corona, California

Attn: Mr. William C. Spindler (Code 441)

Naval Ordnance Laboratory
Department of the Navy
Silver Spring, Maryland

Attn: Philip B. Cole (Code WB)

DEPARTMENT OF THE AIR FORCE

Wright-Patterson AFB
Aeronautical Systems Division
Dayton, Ohio

Attn: George W. Sherman, APIP

Cell Reports (cont.)

Mr. Kenneth B. Higbie
Staff Metallurgist
Office, Director of Metallurgy Research
Bureau of Mines
Interior Building
Washington, D. C. 20240

Institute for Defense Analyses
Research and Engineering Support Division
1666 Connecticut Avenue, N. W.
Washington 9, D. C.

Attn: Dr. George C. Szego/R. Hamilton

Power Information Center
University of Pennsylvania
Moore School Building
200 South 33rd Street
Philadelphia 4, Pennsylvania

Office of Technical Services
Department of Commerce
Washington, D. C. 20009

PRIVATE INDUSTRY

Alfred University
Alfred, New York
Attn: Professor T. J. Gray

Allis-Chalmers Mfg. Co.
1100 S. 70th Street
Milwaukee 1, Wisconsin
Attn: Dr. W. Mitchell, Jr.

Allison Division of General Motors
Indianapolis 6, Indiana
Attn: Dr. Robert E. Henderson

American Cyanamid Company
1937 W. Main Street
Stamford, Connecticut
Attn: Dr. R. G. Haldeman

Cell Reports (cont.)

American Machine & Foundry
689 Hope Street
Springdale, Connecticut
Attn: Dr. L. H. Shaffer
Research & Development Division

Astropower, Inc.
2968 Randolph Avenue
Costa Mesa, California
Attn: Dr. Carl Berger

Battelle Memorial Institute
Columbus 1, Ohio
Attn: Dr. C. L. Faust

Bell Telephone Laboratories, Inc.
Murray Hill, New Jersey
Attn: Mr. U. B. Thomas

Clevite Corporation
Mechanical Research Division
540 East 105th Street
Cleveland, Ohio
Attn: A. D. Schwope

Electrochimica Corp.
1140 O'Brien Drive
Menlo Park, California
Attn: Dr. Morris Eisenberg

Electro-Optical Systems, Inc.
300 North Halstead Street
Pasadena, California
Attn: E. Findl

Engelhard Industries, Inc.
497 DeLancy Street
Newark 5, New Jersey
Attn: Dr. J. G. Cohn

Cell Reports (cont.)

Esso Research and Engineering Company
Products Research Division
P. O. Box 215
Linden, New Jersey
Attn: Dr. Carl Heath

The Franklin Institute
Philadelphia, Pennsylvania
Attn: Mr. Robert Goodman

General Electric Company
Direct Energy Conversion Operations
Lynn, Massachusetts
Attn: Dr. E. Glazier

Garrett Corp.
1625 Eye Street, N. W.
Washington 6, D. C.
Attn: George R. Shepherd

General Electric Company
Research Laboratory
Schenectady, New York
Attn: Dr. H. Liebhafsky

General Electric Company
Missile and Space Vehicle Department
P. O. Box 8555
Philadelphia 1, Pennsylvania
Attn: A. D. Taylor

General Motors Corp.
Box T
Santa Barbara, California
Attn: Dr. C. R. Russell

Globe-Union, Inc.
Milwaukee 1, Wisconsin
Attn: Dr. C. K. Morehouse

Cell Reports (cont.)

Hoffman Electronics Co.
Research Laboratory
Santa Barbara, California
Attn: Dr. Joseph Smatko

Johns Hopkins University
Applied Physics Laboratory
8621 Georgia Avenue
Silver Spring, Maryland
Attn: W. A. Tynan

Leesona Moos Laboratories
Lake Success Park
Community Drive
Great Neck, New York
Attn: Dr. A. Moos

McDonnell Aircraft Corporation
Attn: Project Gemini Office
P. O. Box 516
St. Louis 66, Missouri

Monsanto Research Corporation
Everett 49, Massachusetts
Attn: Dr. J. O. Smith

North American Aviation Co.
S & ID Division
Downey, California
Attn: Dr. James Nash

Pratt and Whitney Aircraft Division
United Aircraft Corporation
East Hartford 8, Connecticut
Attn: Librarian

Radio Corporation of America
Astro Division
Heightstown, New Jersey
Attn: Dr. Seymour Winkler

Cell Reports (cont.)

Radio Corporation of America
Somerville, New Jersey

Attn: Dr. G. Lozier

Speer Carbon Company
Research and Development Laboratories
Packard Road at 47th Street
Niagara Falls, New York

Attn: Dr. L. M. Liggett

Stanford Research Institute
820 Mission Street
So. Pasadena, California

Attn: Dr. Fritz Kalhammer

Thiokol Chemical Corporation
Reaction Motors Division
Denville, New Jersey

Attn: Dr. D. J. Mann

Thompson Ramo Wooldridge
2355 Euclid Avenue
Cleveland 17, Ohio

Attn: Mr. Victor Kovacik

Unified Science Associates, Inc.
826 S. Arroyo Parkway
Pasadena, California

Attn: Dr. Sam Naiditch

Union Carbide Corporation
12900 Snow Road
Parma, Ohio

Attn: Dr. George E. Evans

University of California
Space Science Laboratory
Berkeley 4, California

Attn: Prof. Charles W. Tobias

Cell Reports (cont.)

University of Pennsylvania
Electrochemistry Laboratory
Philadelphia 4, Pennsylvania
Attn: Prof. John O' M. Bockris

University of Pennsylvania
Philadelphia 4, Pennsylvania
Attn: Dr. Manfred Altman

Western Reserve University
Cleveland, Ohio
Attn: Prof. Ernest Yeager

Yardney Electric Corp.
New York, New York
Attn: Dr. Paul Howard

Mr. Peter D. Richman, President
ChemCell Inc.
3 Central Avenue
East Newark, N. J. 07029